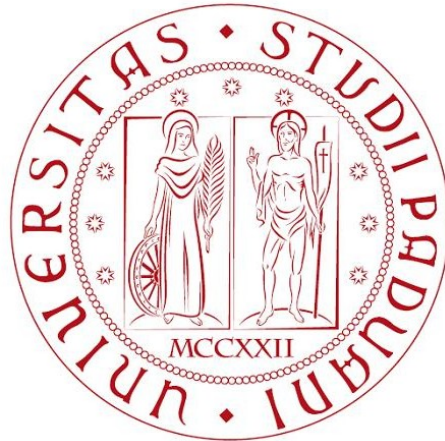# Università degli Studi di Padova

Dipartimento di Fisica ed Astronomia "Galileo Galilei"

Corso di Laurea Magistrale in Fisica

IR thermography analysis of the powerful hydrogen beam at ELISE

Laureanda:
Isabella Mario

Relatore: Dr. Gianluigi Serianni
Correlatore: Prof. Dr.-Ing. Ursel Fantz

Ai miei genitori Patrizia e Maurizio,
Ai miei nonni Angelo e Mirella,
Ad Andrea e Riccardo.

ABSTRACT

La test facility ELISE per ioni negativi dell'idrogeno è dotata di un calorimetro strumentale per caratterizzare la potenza e l'uniformità del fascio. Oltre a fornire una calorimetria mediante la misura della temperatura dell'acqua di raffreddamento e una misura di temperatura dalle termocoppie, i 30×30 blocchi di rame che formano la superficie del calorimetro sono monitorati da una telecamera infrarossa. Attualmente le procedure per l'analisi infrarossa si sono dimostrate ben funzionanti ma sono basate su un utilizzo passo passo di routines separate per cui solo impulsi selezionati su richiesta sono caratterizzati. Nel caso di operazioni quotidiane è fortemente desiderabile automatizzare le routines di analisi. Tale automatizzazione permette di aggiungere l'analisi infrarossa al database standard di ELISE e sarà il primo passo di questa tesi magistrale. Successivamente il metodo di analisi sarà applicato al database di ELISE per caratterizzare le proprietà del fascio in differenti condizioni operative, quindi identificare l'influenza dei parametri della sorgente e del sistema di accelerazione sulle proprietà del fascio.

ABSTRACT

The negative hydrogen ion test facility ELISE is equipped with a diagnostic calorimeter facilitating to characterize the beam power and the beam uniformity. Besides providing water calorimetry and thermocouples, the 30×30 copper blocks of the calorimeter are monitored by an infrared camera system. The present analysis routine applied to the IR data proved to work well but is based on a step-by- step usage of several routines such that only selected beam pulses are characterized on demand. For routine operation it is highly desirable to automatize the analysis routines. This automatization allows adding the IR results to the standard ELISE database and will be the first step in the master thesis. Subsequently, the analysis method will be applied to the ELISE database in order to characterize the beam features in different operating conditions, thus identifying the influence of source and accelerator parameters on the beam properties.

Riassunto

La fusione termonucleare fornirà al mondo con una fonte di energia sicura ed ecologicamente pulita.

Una mistura di deuterio trizio, che costituisce il carburante dei reattori, è nello stato di plasma ed è magneticamente confinato in una camera da vuoto di forma toroidale. Gli iniettori di fasci neutri (NBI) forniranno un sistema di riscaldamento ausiliario per tali impianti termonucleari. ITER, il reattore termonucleare sperimentale internazionale che è in fase di realizzazione a Cadarache (FR), avrà due NBI di 16.5 MW ciascuno.

L'iniettore di fasci neutri progettato per ITER, descritto nella sezione 1.3, è basato su una sorgente di ioni negativi, in particolare una sorgente RF, il cui progetto è stato sviluppato negli ultimi decenni al Max-Planck-Insitut für Plasmaphysik (IPP). L'uso di ioni negativi è obbligatorio per raggiungere un alta efficienza di neutralizzazione per un fascio dell'energia di 1 MeV (richiesti da ITER). Nella sorgente il plasma è creato da antenne RF, poi il fascio è formato e accelerato da un sistema di griglie. La fase di estrazione e accelerazione consistono in stadi di accelerazione elettrostatica grazie al potenziale di griglie disposte perpendicolarmente alla linea di fascio (sviluppato dal National Insitutes for Quantum and Radiological Science and Technology QST Naka in Giappone).

Presso IPP sono presenti prototipi di sorgenti di ioni in scala 1/8 rispetto al progetto di ITER e l'esperimento ELISE che mira a studiare la fisica delle sorgenti di ioni con una sorgente che è metà della sorgente di ITER con una superficie di estrazione di circa $1000 \, \text{cm}^2$. ELISE, il cui progetto e diagnostiche di fascio sono descritte nel capitolo 2, è un importante passo tra i prototipi in piccola scala e una sorgente in scala $1:1$ di ITER.

Questa tesi mira a caratterizzare le proprietà' del fascio di ELISE, in particolare la larghezza e la deflessione del fascio, in differenti condizioni operative attraverso l'analisi infrarossa del profilo di temperatura conseguente alla deposizione di energia da parte del fascio su un calorimetro diagnostico. L'analisi descritta in 3.2 è automatizzata e i parametri del fascio misurati dall'impronta del fascio sul calorimetro sono automaticamente raccolti in un database generale. La calibrazione dell'emissività è svolta utilizzando la temperatura misurata da termocoppie installate nel calorimetro.

Nella sezione 3.3 è stato fatto un iniziale controllo incrociato con altre diagnostiche di fascio per testare l'affidabilità e la robustezza dell'analisi. Successivamente i parametri di fascio ricavati dall'analisi sono studiati in funzione di parametri operativi che hanno un impatto sul plasma e sul fascio. Nel capitolo 4 vengono discussi i risultati.

L'effetto dell'ottica di fascio, dell'accelerazione e della pressione sono studiati nelle sezioni 4.1, 4.2 e 4.3. Il plasma nella sorgente è modificato attraverso campi elettrici e magnetici e da magneti esterni installati dentro la sorgente. I risultati dall'analisi infrarossa in funzione dei parametri operativi che corrispondono ai campi elettrici e magnetici sono discussi nelle sezioni 4.5, 4.6, 4.4.

La beam emission spectroscopy (BES) è una diagnostica che fornisce la divergenza del fascio attraverso l'analisi del picco Doppler, che restituisce la distribuzione di velocità delle particelle nel fascio, per la linea spetrale H_α. La larghezza del fascio ricavata dell'impronta dello stesso sul calorimetro e' confrontata con la divergenza misurata dalla BES. Gli spettri della BES indicano la presenza di una larga componente addizionale nella divergenza del fascio, tale componente e' investigata utilizzando le porzioni esterne del calorimetro. L'analisi e il confronto sono descritti nella sezione 4.7.

Nell'ultimo capitolo sono riassunti i risultati e sono suggeriti futuri sviluppi.

Summary

Thermonuclear fusion will supply the world with a safe, environmentally friendly energy source.

Neutral beam injectors (NBI) provide an auxiliary heating system and a current drive system for thermonuclear plants. The deuterium-tritium mixture constituting the fuel in such thermonuclear reactors is in a plasma state and it is magnetically confined in a toroidally shaped vessel. In ITER, the international thermonuclear experimental reactor that is under realisation in Cadarache (FR), two NBI of 16.5 MW each will be installed .

The ITER-like neutral beam injector described in section 1.3 is based on a negative hydrogen ion source, based on a RF source, whose design was developed at the Max-Planck-Institut für Plasmaphysik (IPP) in the last decades. The use of negative ions is mandatory to reach high neutralisation efficiencies in case of beams of $1\,\mathrm{MeV}$ energy (ITER requirements). In the source volume a plasma is ignited by means of RF coils, then the beam is formed and accelerated by a grid system. The extraction and acceleration stages consist in potential steps applied to grids disposed perpendicularly to the beam-line (developed by the National Insitutes for Quantum and Radiological Science and Technology QST Naka in Japan)).

At the IPP small scale ion source prototypes that correspond to an 1/8 of the ITER size as well as the test facility ELISE that aims to investigate the physics behind the ion sources with a source half the ITER size whose extraction area is about $1000\mathrm{cm}^2$ are present. ELISE, whose design and beam diagnostics are described in chapter 2, is an important step between small scale prototypes and the full size ITER source.

This thesis aims to characterize the beam properties of ELISE, in particular the beam width and the beam deflection, in different operational conditions by means of the IR analysis of the beam profile on a diagnostic calorimeter. The analysis described in 3.2 is automatized and the beam parameters deduced from the beam imprint on the calorimeter are automatically collected in a general database. The emissivity calibration was performed using the temperature measured by thermocouples embedded on the calorimeter.

In section 3.3 a preliminary cross-check with other beam diagnostics is performed in order to test the reliability and the robustness of the analysis. Then the beam parameters retrieved from the IR analysis are investigated as a function of operational parameters that have an impact on the plasma and the beam. In chapter 4 the results are discussed.

The effects of beam optics, acceleration potential and pressure on the beam are studied in sections 4.1, 4.2 and 4.3. The plasma in the source is modified by means of applied electric and magnetic fields and by external magnets installed inside the source volume. The IR evaluation results as a function of operational parameters corresponding to the electric and magnetic field are discussed in sections 4.5, 4.6 and 4.4.

The beam emission spectroscopy (BES) is a beam diagnostic system that provides the beam divergence by means of the analysis of the H_{alpha} Doppler peak, that describes the velocity distribution of the particles in the beam. The beam width obtained by the beam imprint on the calorimeter and the beam divergence measured by the BES are compared. The spectra of BES indicate the presence of an additional broad component in the beam divergence that is investigated by means of the external portions of the diagnostic calorimeter. The cross-checks and analyses are described in section 4.7.

Last but not least in the conclusions the results are summarized and future developments are suggested.

Contents

Chapter 1

Introduction

In the last few decades the world has seen an unprecedented increase in the consumption of energy, mainly from fossil fuel, which have limited reserves. At the same time it has witnessed a growth in number and intensity of phenomena correlated to the temperature increase, whose main cause is the increase of CO_2 concentration in the atmosphere due to fossil fuel consumption.

These aspects prompt the search for a new energy source having the advantages of being relatively clean and nearly inexhaustible. A possible candidate that fulfils these requirements is controlled thermo-nuclear fusion.

1.1   Nuclear Fusion and basic concepts of plasma physics

Fusion happens when two nuclei are close enough to interact with each other through the strong interaction field which is attractive: the high kinetic energy increases the probability to overcome the repulsive Coulomb barrier thanks to the tunnel effect. For this purpose the nuclei should have high kinetic energy, at least enough to overcome the Coulomb repulsion: a feasible way consists in using matter in a plasma state.

The binding energy (MeV) per nucleon is shown in figure 1.1 and it indicates that the fusion between two nuclei into a heavier one results in a release of energy only if the product is lighter than iron (Fe).
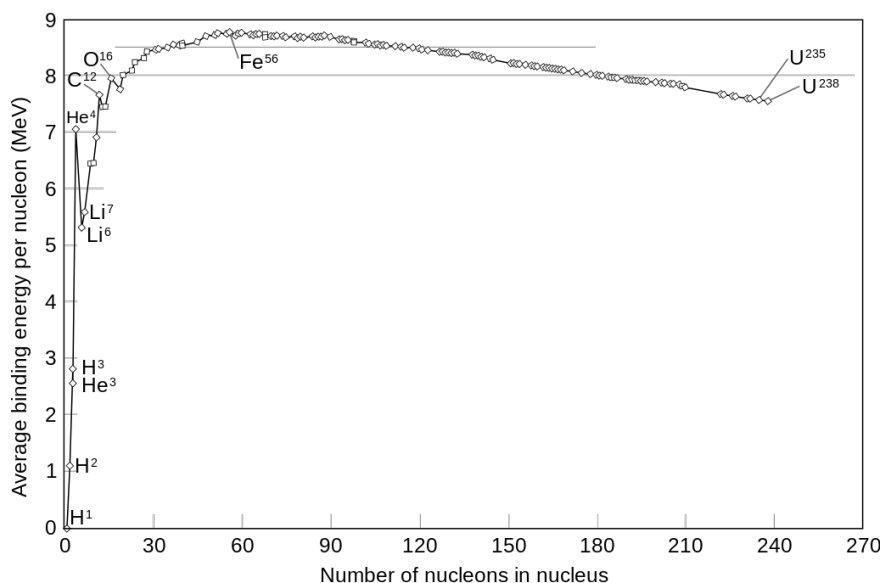

Figure 1.1: Binding energy per nucleon for different elements.

1

The most convenient fusion reaction between two nuclei, among all the possibilities (tab.1.1), is the one that involves deuterium and tritium (eq.1.1 and figure 1.2(b)), which has the largest cross section and thus the highest reaction probability (see figure 1.2(a)).The reactions between two deuterium nuclei are possible as well as the $D - T$ reaction.

The obtained energy is then divided between the two products according to the inverse of their mass ratio: 3.5 MeV for the α-particle (^4He) and 14.1 MeV for the neutron.

$$D + T \rightarrow\ ^4He + n + 17.6 \text{MeV} \tag{1.1}$$

$$
\begin{aligned}
D + T &\rightarrow\ ^4\text{He (3.5 Mev)} + \text{n (14.1 MeV)} \\
D + D &\rightarrow\ \text{T (1.01 MeV)} + \text{p (3.02 MeV) (50\%)} \\
D + D &\rightarrow\ ^3\text{He (0.82 MeV)} + \text{n (2.45 MeV) (50\%)} \\
D + {}^3\text{He} &\rightarrow\ ^4\text{He (3.6 MeV)} + \text{p (14.7 MeV)} \\
T + T &\rightarrow\ ^4\text{He} + \text{2 n} + \text{11.3 MeV} \\
{}^3\text{He} + {}^3\text{He} &\rightarrow\ ^4\text{He} + \text{2 p} \\
{}^3\text{He} + T &\rightarrow\ ^4\text{He} + \text{p} + \text{n} + \text{12.1 MeV (51\%)} \\
{}^3\text{He} + T &\rightarrow\ ^4\text{He (4.8 MeV)} + \text{D (9.5 MeV) (43\%)} \\
{}^3\text{He} + T &\rightarrow\ ^4\text{He (0.5 MeV)} + \text{n (1.9 MeV)} + \text{p (11.9 MeV) (6\%)} \\
D + {}^6\text{Li} &\rightarrow\ \text{2 }^4\text{He} + \text{22.4 MeV} \\
\text{p} + {}^6\text{Li} &\rightarrow\ ^4\text{He (1.7 MeV)} + {}^3\text{He (2.3 MeV)} \\
{}^3\text{He} + {}^6\text{Li} &\rightarrow\ \text{2 }^4\text{He} + \text{p} + \text{16.9 MeV} \\
\text{p} + {}^{11}\text{B} &\rightarrow\ \text{3 }^4\text{He} + \text{8.7 MeV}
\end{aligned}
$$

Table 1.1: list of the most favourable fusion reactions [1].

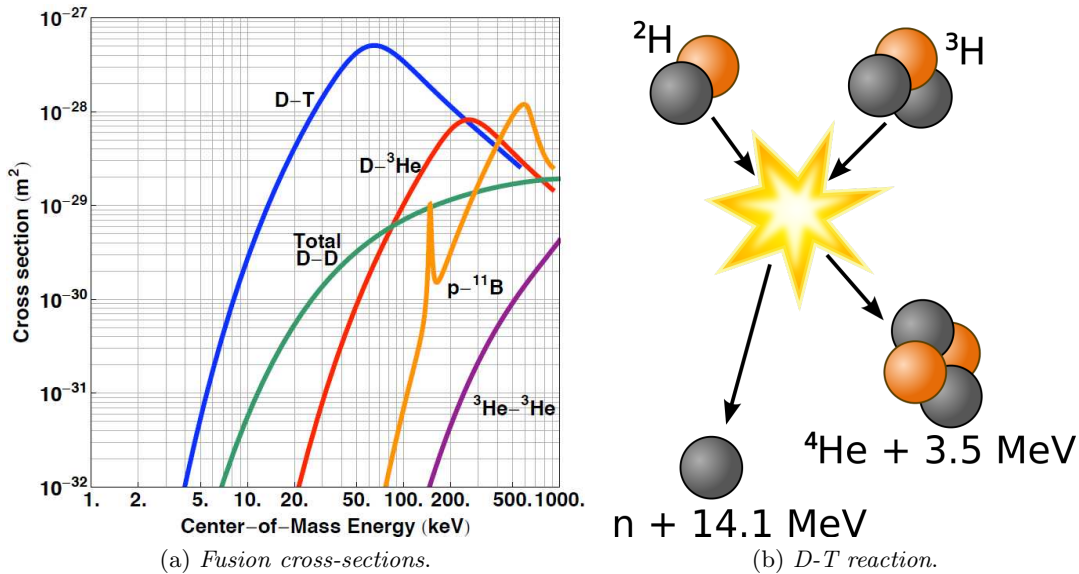(a) *Fusion cross-sections.*　　　　(b) *D-T reaction.*

Figure 1.2: left: Cross-sections of some fusion reactions as functions of kinetic energy of an incident D or p on a stationary target [1]; right: reaction between deuterium and tritium

The reagents, Deuterium and Tritium, can easily be found in nature and produced artificially respectively: the first can be extracted from seawater (30 mg/cm^3) and the second from the following reaction (eq.1.2) inside a nuclear reactor.

$$n + {}^6Li \rightarrow\ ^4He + T + 4.8 \text{MeV} \tag{1.2}$$

Therefore the primary fuels are deuterium and lithium, the latter available from the Earth crust.

The main advantages of nuclear fusion with respect to fission consist in the safety conditions and reduced nuclear waste: in order to achieve fusion the physics requirements are so strict that in case of accidents the fusion process will stop by itself very quickly. In addition, the main waste materials in a fusion reactor, primary the walls, are activated by neutrons produced during the fusion reaction: the material activation due to neutron radiation will be depleted in about $1 - 2$ centuries.

In order to reach a considerable amount of fusion reactions it is mandatory to have a mixture of deuterium and tritium with a temperature around 10^8 K and density in the order of 10^{20} m^{-3} for a sufficiently long time (few seconds). In this conditions matter is in plasma state; a short introduction about plasma is discussed at the end of this section. The remaining part of this section is focused on general concepts about fusion and plasma physics.

The net energy gain Q in steady state for a fusion reactor is defined as the ratio of output power P_{out} to input power P_{in}.

The criterion for a power plant to succeed is a Q factor larger than 1 and it must take into account the losses due to energy conversion in coupling the power inside the reactor and in extracting electric energy. Power balance, in which $Q = 1$, is called *break-even* condition. The input power is described by auxiliary power P_{aux} supplied by external heating system and the output power is the result of fusion P_{fusion} so that it is possible to write:

$$Q = P_{\text{out}}/P_{\text{in}} = P_{\text{fusion}}/P_{\text{aux}} \tag{1.3}$$

Ideally in a thermonuclear reactor the self sustainability is $P_{\text{aux}} = 0$ and so $Q \to \infty$: this is possible if the energy from α-particles is used to heat the plasma itself (the additional term is reported in the following equations as P_α). The self-sustainability condition can be relaxed by maintaining a low energy inflow in a regime in which the outcome energy is high enough to have a positive gain factor.

During the ignition phase the heating power is redistributed by increasing the kinetic energy dW_{k}/dt and lost due to transport phenomena P_{trans}. The equation is given by 1.4:

$$P_{\text{heat}} = P_{\text{aux}} + P_\alpha - P_{\text{Br}} = dW_{\text{k}}/dt + P_{\text{trans}} \tag{1.4}$$

where P_{Br} are the Bremsstrahlung losses and P_α the power for α-particles. The energy confinement time τ_E describes the temporal evolution of the transport phenomena and is defined as eq.1.5.

$$\tau_{\text{E}} = W_{\text{k}}/P_{\text{trans}} = W_{\text{k}}/(P_{\text{heat}} - dW_{\text{k}}/dt) \tag{1.5}$$

Moreover formulas in eq. 1.6 and eq. 1.7 are considered for a 50/50 mixture of deuterium and tritium ($n_{\text{D}} = n_{\text{T}} = n_{\text{e}}$) [1]. While eq. 1.8 is the kinetic energy for a plasma of volume V_p, temperature T and density n_e.

$$P_{\text{Br}} = C_{\text{B}} T^{1/2} n_{\text{e}}^2 V_{\text{p}} \tag{1.6}$$

$$P_\alpha = n_{\text{T}} n_{\text{D}} \langle \sigma v \rangle E_\alpha V_{\text{p}} = \frac{n_{\text{e}}^2}{4} \langle \sigma v \rangle E_\alpha V_{\text{p}} \tag{1.7}$$

$$W_{\text{k}} = 3 n_{\text{e}} V_{\text{p}} k_{\text{B}} T \tag{1.8}$$

Where $\langle \sigma v \rangle$ is the rate coefficient i.e. a convolution of the collision cross-section σ and the velocity v, E_α the energy carried by the α-particles and V_{p} the plasma volume. Using equations 1.6, 1.7, 1.8 and the approximation $P_{\text{fusion}} = 5 P_\alpha$ (so from eq.1.3 $P_{\text{aux}} = 5 P_\alpha/Q$) eq. 1.4 can be written as:

$$\frac{n_{\text{e}}^2}{4} \langle \sigma v \rangle E_\alpha \left(\frac{Q+5}{Q} \right) - C_{\text{B}} T^{1/2} n_{\text{e}}^2 = \frac{3 n_{\text{e}} k_{\text{B}} T}{\tau_{\text{E}}} + \frac{d}{dt} \left(3 n_{\text{e}} k_{\text{B}} T \right) \tag{1.9}$$

The steady-state $d/dt = 0$, the conversion efficiency for input power sources η_{in} [2] and the conversion efficiency of output thermal energy to electric energy η_{out} [2] are considered to find the formula for the product $n_{\text{e}}\tau_{\text{e}}$ in eq. 1.10.

$$n_{\text{e}}\tau_{\text{E}} = \frac{3(1 - \eta_{\text{in}}\eta_{\text{out}})k_{\text{B}}T}{\eta_{\text{in}}\eta_{\text{out}}\frac{\langle\sigma v\rangle E_\alpha(Q+5)}{4Q} - C_{\text{B}}(1 - \eta_{\text{in}}\eta_{\text{out}})T^{1/2}} \tag{1.10}$$

To summarize, in order to provide the necessary kinetic energy to achieve fusion in a reactor, specific conditions are needed: these conditions concern the density n, the temperature T and confinement energy time τ_E. The product of these terms is called *triple product* and is a threshold value for fusion reaction in a power plant. Lawson was the first who gave the minimum temperature for fusion: in a fusion reactor the power density from fusion must exceed the Bremsstrahlung radiation and this happens at 3 keV for D-T plasma while at 20 keV for D-D plasma (see figure 1.3*(a)*) [3]. The minimum of eq.1.10 for the break-even condition ($Q = 1$) for a D-T plasma is at 15 keV (see eq.1.11):
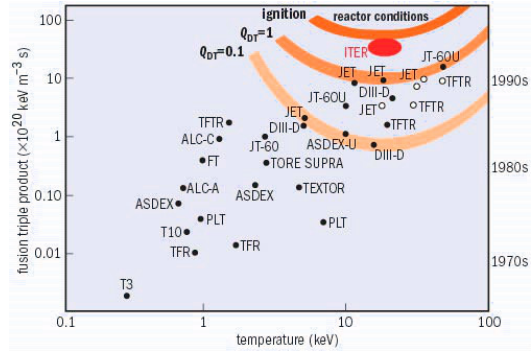
$$n_e\tau_E = 10^{20}\text{s m}^{-3} \tag{1.11}$$

The Lawson criterion is based on the triple product $n\tau_E T_e$ and in this case is given by eq. 1.12

$$n_e\tau_E T_e > 1.5 \cdot 10^{20}\text{keV s m}^{-3} \tag{1.12}$$
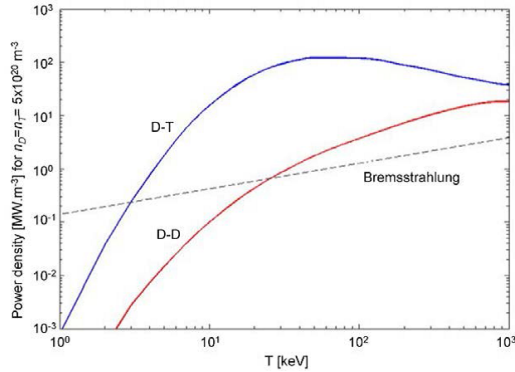
(a) *Minimum temperature for fusion.*

(b) *Plasma testbeds in relation with the Lawson's criterion.*

Figure 1.3: left: Power density for a plasma density of $n_D = n_T = 5 \cdot 10^{20} m^{-3}$ (plotted with data from [4] pag. 45); right: characteristics of several test reactors in terms of $n\tau_E$ vs. T [5]

The ignition criterion ($Q \to \infty$) gives the minimum for eq.1.10 at a temperature of 30 keV and the triple product is given by the eq.1.13.

$$n_e\tau_E T_e > 8.1 \cdot 10^{21} \text{ keV s m}^{-3} \tag{1.13}$$

In figure 1.3*(b)* the rate of increase in performances of fusion experiments is shown. The solid dots represent results from machines that use or have used a deuterium plasma while in open dots results from a tritium-deuterium plasma are represented.

As mentioned before, the mixture of deuterium and tritium, which constitutes the fuel of nuclear plants, is in plasma state. To raise the triple product up to fusion requirements, and in particular the density n, it is essential to confine the plasma. Two techniques are developed:

- Inertial confinement: the reactor consists in a system of lasers that heats a compressed pellet of fuel. This system aims to extract fusion energy before the system expands and cools down due to a Rayleigh Taylor instability (interface instability) [6].

- Magnetic confinement: as explained below, the charge carriers inside the plasma follow the magnetic field lines and are trapped in closed trajectories inside the plasma volume. In this way it is possible to contain and confine plasma in a finite volume. The easiest possible configuration for a confined plasma is a linear column, however the main issue are losses of particles at the edges of the column: the solution is a toroidal shape of the vessel in which coils produce a magnetic field. Different magnetic field configurations are possible in a torus-shape vessel in which the plasma is magnetically confined. To avoid sausage and kink instabilities [6] and to prevent charge separation, a combination of poloidal and toroidal component is used for the magnetic field. Such configuration is used in Tokamak and Stellarator devices (see figure 1.4).
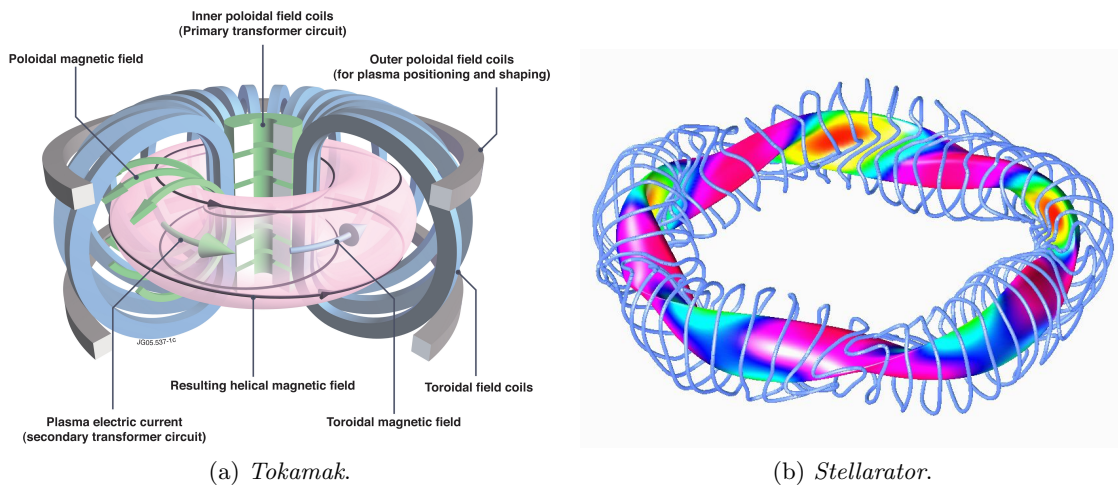

(a) *Tokamak.*   (b) *Stellarator.*

Figure 1.4: Use of magnetic field with both toroidal and poloidal components. Left: examples of facilities based on Tokamak configuration are EFDA-JET [7] in Great Britain and DIII-D [8] in the USA; Right: large Stellarator at LHD [9] in Japan and Wendelstein-7X [10] in Germany.

The easiest way to obtain a plasma from a gas is heating such gas until it is ionized to a non negligible amount inside a globally neutral volume. The long-range Coulomb interaction makes the description of particle dynamics hard to treat with analytic methods. Therefore a mean force field is usually introduced to describe the effect of all the surrounding charged particles on the trajectory of one of these charge carriers. A charge undergoes a shielding due to the immediately response of the plasma to a charge imbalance: this phenomenon is the so-called Debye shielding and it is characterized by a typical length called the Debye Length λ_D(eq.1.14).

$$\lambda_D = \sqrt{\frac{\epsilon_0 k_B T_e}{n_e e^2}} \tag{1.14}$$

where T_e is the electron temperature, n_e the electron density, e the electron charge, k_B the Boltzmann constant and ϵ_0 the permittivity of the vacuum. This means that, at a distance comparable to λ_D from the charge imbalance centre, charges with opposite sign completely shield the potential and particles spaced more than λ_D are not affected by the charge.

Another phenomenon connected to the screening of a charge imbalance is the *space charge compensation*. Consider a volume in which the majority of charged particles have the same charge e.g. negative ions, the electrostatic repulsion makes the negative ions spread but the

potential attracts positive charges that counteract the dispersion. This model is used to describe negative ion beams whose divergence, a parameter that measures the dispersion of the beam, depends on the density of the background gas. The background gas, formed by neutrals, is ionized by beam particles and it supplies the space charge compensation with positive ions: the higher the background gas pressure, the closer to the beam source the beam compensation takes place and the lower the beam divergence [11].

Generally, inside a medium and in particular in a plasma, charged particles are basically driven by electric field and by inhomogeneities: it is straightforward to introduce the diffusion coefficient and the electrical mobility (eq.1.15 and eq.1.16) [6].

$$\mu = \frac{q}{m\nu_c} \tag{1.15}$$

$$D = \frac{k_B T}{m\nu_c} \tag{1.16}$$

where ν_c is the collision frequency, q the electric charge, m the mass of the particle, k_B the Boltzmann's constant and T the temperature. The equation for the drift velocity v_d, that describes the velocity of a charged particle, obtained for this model is reported in eq.1.17:

$$v_d = \mu E + D\frac{\nabla n}{n} \tag{1.17}$$

In plasmas, additionally, the separation of charges due to internal electromagnetic fields creates a charge imbalance which, in turn, creates an electric field which opposes the charge separation. This mechanism is called *ambipolar diffusion* and in this way plasma is kept together and prevents the charge separation.

The presence of a magnetic field introduces an anisotropy into the system. Basically it affects the motion of single particles and, consequently, the collective motion of the plasma: taking into account one single orbit the magnetic field adds a gyrating component to the orbit due to the Lorentz Force (eq.1.18):

$$\mathbf{F} = q(\mathbf{E} + \mathbf{v} \times \mathbf{B}) \tag{1.18}$$

where $\mathbf{F}$ is the resulting force applied to a particle with charge q, $\mathbf{E}$ is the electric field, $\mathbf{B}$ is the magnetic field and $\mathbf{v}$ is the velocity of the particle. It is important to highlight that only charged particles are affected by the Lorentz force.

The gyrating component has a frequency called *cyclotron frequency* (eq.1.19) and, in the plane perpendicular to the B field, it gives a curved component with specific radius called *Larmor radius* (eq.1.20).

$$\omega_c = \frac{|q|\,B}{m} \tag{1.19}$$

$$r_L = \frac{mv_\perp}{qB} \tag{1.20}$$

where m is the mass of the particle, $v_\perp$ is the component of the velocity perpendicular to the $\mathbf{B}$ field vector and q is the charge. Charged particles are called *magnetized particles* when the Larmor radius is smaller than the scale of the system where that particles are studied.

Returning to the case of motion in a plasma, the diffusion coefficient and the mobility change slightly the formulation and new values depend on the orientation with respect to the $\mathbf{B}$-field: in parallel direction the coefficient are unaffected while perpendicularly they are described by eq.1.21 and eq.1.22 [6].

$$\mu_\perp = \frac{\mu}{1 + \omega_c^2/\nu_c^2} \tag{1.21}$$

$$D_\perp = \frac{D}{1 + \omega_c^2/\nu_c^2} \tag{1.22}$$

where ω_c is the cyclotron frequency.

The presence of a general force $\mathbf{F}$ perpendicular to the magnetic field $\mathbf{B}$ causes the particle to drift in a direction perpendicular to both: the velocity due to this drift is given by eq.1.23.

$$\mathbf{v}_F = \frac{\mathbf{F} \times \mathbf{B}}{qB^2} \tag{1.23}$$

this formula can be specialized in the case of the presence of electric field $\mathbf{E}$ ($E \times B$ drift) eq.1.24 and in case of inhomogeneities due to pressure gradient (so called *diamagnetic* drift) eq.1.25.

$$\mathbf{v}_{E \times B} = \frac{\mathbf{E} \times \mathbf{B}}{B^2} \tag{1.24}$$

$$\mathbf{v}_{\text{diam}} = \frac{\nabla p \times \mathbf{B}}{qnB^2} \tag{1.25}$$

where p is the pressure, ∇p is the pressure gradient. The two types of drift explained above are significantly different: for the $E \times B$ drift there is no charge separation so both electron and ions drift in the same direction (no dependence on q), on the other side the diamagnetic drift implies opposite currents.

1.2 ITER

ITER (The Way in Latin) will be the first experimental device for fusion with a energy gain of about $5 - 10$ times and will open the way to a commercial use of fusion for producing sustainable and clean energy (overview in figure 1.5(a)). The project is a collaboration of EU, USA, Russia, Japan, India, China and South Korea and is being built in Cadarache(FR) [12].

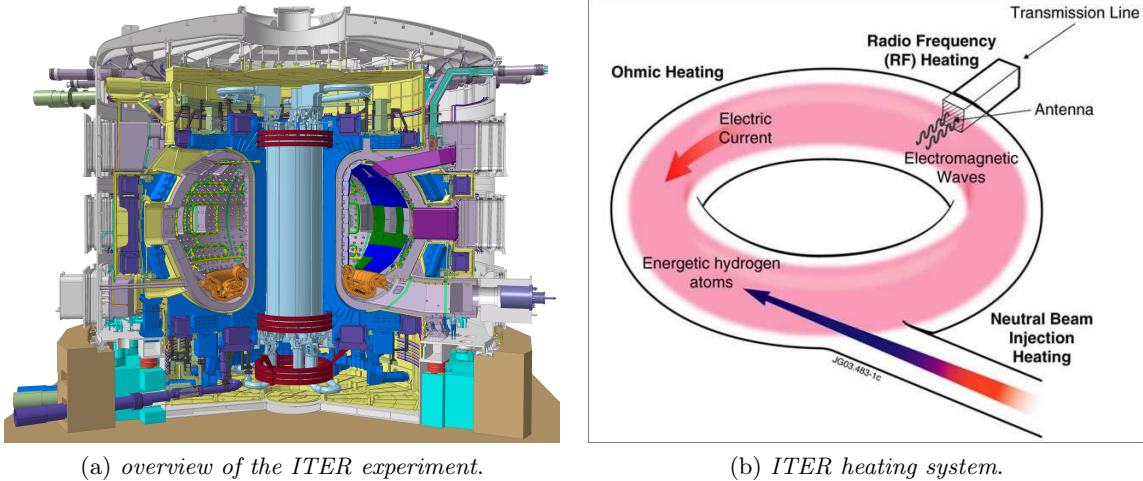(a) *overview of the ITER experiment.*   (b) *ITER heating system.*

Figure 1.5: Right: overview of the ITER experiment [12]; left: ITER heating system [12].

1.2.1 General features of the experiment

The ITER main goals [12] can be summarize as:

- Production of 500 MW of fusion power from 50 MW of input power: ITER is designed to produce a tenfold return on energy (Q=10).

- Bridge the gap between today's smaller-scale experimental fusion devices and the demonstration fusion power plant (DEMO) of the future: scientists will be able to study plasmas under conditions similar to those expected in a future power plant.

- Achieve a deuterium-tritium plasma in which the reaction is sustained through internal heating

- Test tritium breeding: demonstration of the feasibility of producing tritium within the vacuum vessel with a fusion reaction starting from lithium.

- Demonstration of the availability, reliability and of the safety characteristics of a fusion device.
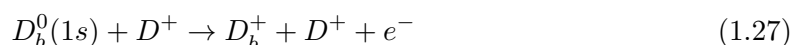
ITER main parameters are reported in table 1.2. Before operating with D-T plasmas, preliminary stages of hydrogen and deuterium plasma will be performed in order to test operating systems and components of the machine. The temperature required to reach operating conditions is around 15 keV hence two additional heating systems will be used: RF waves and neutral beam injectors (NBI) (see fig.1.5 *(b)*). The first is based on producing RF waves and coupling them into the plasma with respect to the cyclotron frequency of the species (e.g. $\approx 100MHz$ for ions and $\approx 100GHz$ for electrons). The matching of the frequency is necessary to enhance the power deposition on the plasma: the mechanism behaves like a resonance system so that the maximum efficiency is reached for the resonance frequency that in this case corresponds to the cyclotron frequency. In the case of neutral beam injectors the heating system consists in a beam of high energetic atoms of hydrogen or deuterium injected into the fusion plasma where they are ionized and deposit their energy during consecutive collisions.

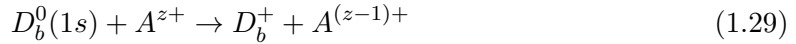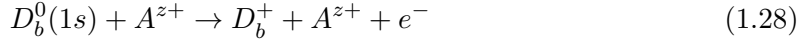| Parameter	Value
Fusion power	500 MW
Power gain factor Q	10
Pulse length	up to 3600 s
Plasma major radius	6.2 m
Plasma minor radius	2.0 m
Plasma current	15 MA
Toroidal field at 6.2 m radius	5.3 T

Table 1.2: ITER facility parameters [12]

1.2.2 Principles of neutral beam heating

The two main purposes of a neutral beam injector are heating the plasma and driving plasma current in order to sustain the poloidal magnetic field. The neutral beam heats the plasma through collisions and it is desirable to release the highest amount of power in the plasma core and not in the edges: for this purpose it is necessary to achieve the correct beam energy otherwise the beam would be too weak to reach the core or strong enough so as to reach the first wall of the vessel due to incomplete beam absorption. The processes through which the energy deposit take place are charge exchange (eq.1.26), ionization by collisions with ions (eq.1.27), ionization by collisions with impurities (eq.1.28), ionization by electron (eq.1.29) and impurity (eq.1.30) by charge exchange. In the following formulas the notation $_b$ indicates particle in the beam, while D and A the deuterium and impurity respectively.

$$D_b^0(1s) + D^+ \rightarrow D_b^+ + D \tag{1.26}$$

$$D_b^0(1s) + D^+ \rightarrow D_b^+ + D^+ + e^- \tag{1.27}$$

$$D_b^0(1s) + A^{z+} \rightarrow D_b^+ + A^{z+} + e^- \qquad (1.28)$$

$$D_b^0(1s) + A^{z+} \rightarrow D_b^+ + A^{(z-1)+} \qquad (1.29)$$

$$D_b^0(1s) + e^- \rightarrow D_b^+ + 2e^- \qquad (1.30)$$

The cross sections for these processes as functions of the beam energy (deuterium beam) are shown in fig.1.6.
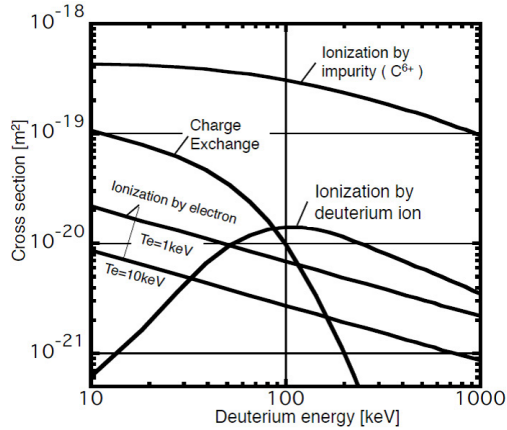

Figure 1.6: Beam energy dependence of charge exchange, ion, impurity and electron ionization cross-sections [1]

A NBI beam line system (overview fig.1.7(a)) is composed of an ion source where hydrogen or deuterium ions are generated and then extracted and accelerated to the desired energy by an extraction/acceleration stage. A neutraliser cell is placed after the ion source: as a result a fraction of ions, see fig.1.7(b), is converted into energetic neutrals, usually with a charge exchange process with collisions against a background gas. The procedure of neutralization is necessary to inject the neutral beam into the magnetically confined plasma. In order to get rid of the ions that are still un-neutralized downstream the neutraliser, a bending magnet is placed after the neutralization stage and it leads the charged particles to an ion dump.
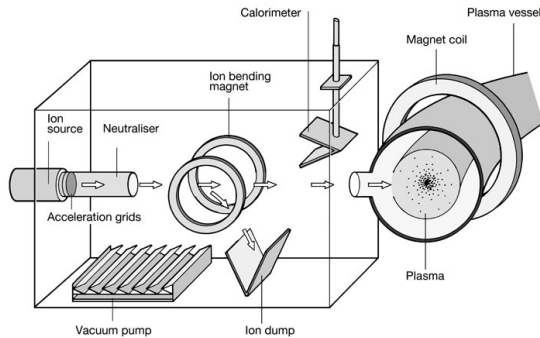
(a) *NBI scheme.*
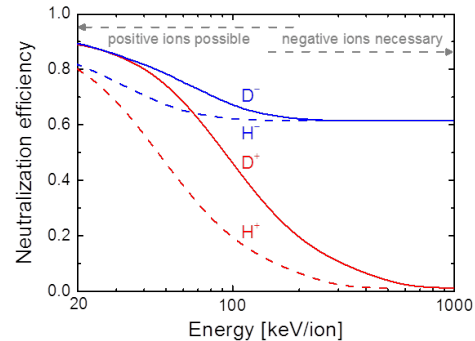
(b) *Neutralization efficiency.*

Figure 1.7: left: Scheme of a neutral beam injector; right: neutralization efficiency of positive and negative ions as a function of energy [1]

The power efficiency of a NBI beamline is mainly determined by the neutralization efficiency in the neutralizer. As seen in fig.1.7(b) positive ions cannot be used at beam energy above 100 keV for H atoms (or respectively above 200 keV for D atoms) because of the low power efficiency: for high energy beams the use of negative ions is mandatory.

1.3   Neutral beam injector

In the following section the general features and requirements of a NBI beamline for ITER will be discussed. The main topic of this thesis concerns the beam after the acceleration and neutralisation stages and therefore ion dumping will not be treated (general concepts are discussed in [1]). In figure 1.8 the design of a neutral beam injector for ITER is shown.
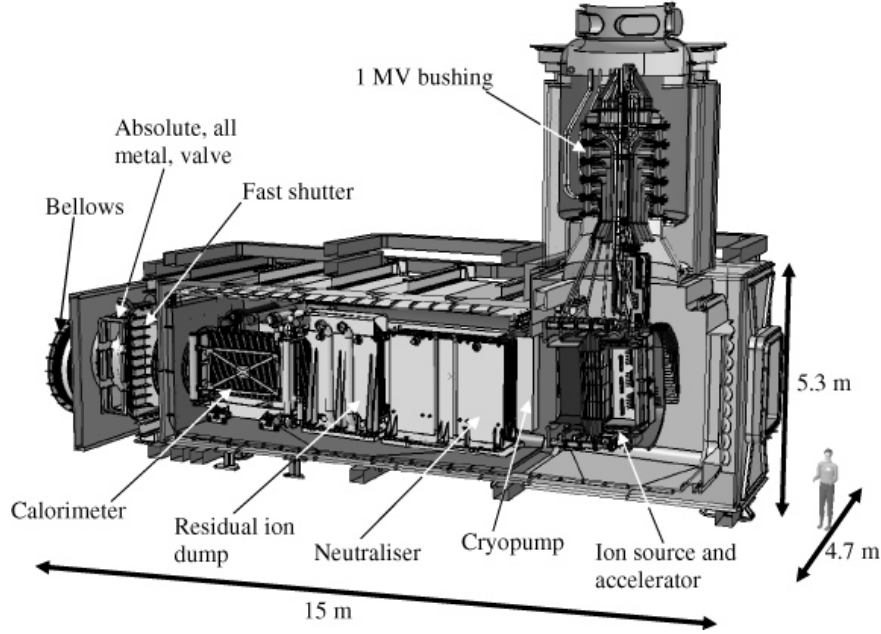
Figure 1.8: Neutral beam injector scheme [13][12].

In table 1.3 are reported the requirements for ITER neutral beam injector.

Parameter	ITER requirements
Number of beamlines	2
Injection Power	33 MW (16.5 MW each source)
Beam Energy	1000 keV (D_2) and 870 keV (H_2)
Source dimensions	1.9×0.9 m^2
Source pressure	0.3 Pa
Extraction area	0.2 m^2
Extracted current	57 A for D beam
	66 A for H beam
Accelerated current	40 A for D beam
	40 A for H beam
Electron content (j_e /j_{ion})	≤ 1
Pulse length	3600 s (D_2) and 1000 s (H_2)
Uniformity	$\pm 10\%$
Divergence	≤ 7 mrad

Table 1.3: ITER neutral beam system source requirements and parameters [13][1].

1.3.1   Negative ion sources

There are two ways to produce plasma in the ion source: with an arc discharge or with an RF source. The first method produces electrons through a discharge between a row of tungsten wires and the chamber: the wires are heated up to 2000-3000 K and the thermionic electrons are accelerated so as ionize a gas in order to form a plasma. The main issue of this method is the wire consumption due to sputtering and evaporation thus wires need to be changed every six months [14]. Moreover tungsten impurities are introduced in the source with a higher consumption of caesium in the volume expansion region (caesium seeding will be introduced later). The latter way aims to ionize a gas using an electromagnetic oscillating field induced by RF coils: again the electrons produced are accelerated and ionise the gas

producing a plasma. RF coils are represented as windings around the driver in fig.1.10. Due to the high consumption of tungsten and caesium and the maintenance needs the arc discharge source was not deemed suitable for the purpose, instead the RF source was chosen for the ITER NBI system [13][15]. The volume in which plasma is ignited and produced is called *driver region* and the *driver* is the mechanical where the RF coils are wound up.

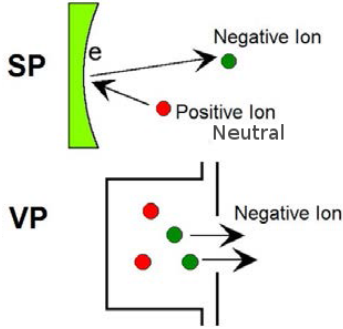There are two main processes for negative ion creation [1][16]:

1. Surface production (SP);

2. Volume production (VP).

The methods are summarized in fig.1.9.

In the surface production method a surface with low work faction is put in contact with the plasma: positive ions and neutrals are driven towards the surface and, after the impact, converted into negative ions and reflected back. The work function is kept low by coating the surface with caesium layer. On the other hand the negative ion beam has a large divergence and, additionally the work function is difficult to control.

Figure 1.9: Schematics of the principles of two methods to produce negative ions [1].

The volume process involves a hydrogen plasma: the negative ion density reaches high levels due to dissociative electron attachment to ro-vibrationally excited hydrogen/deuterium molecules (eq.1.31 and eq.1.32)[16].

$$H_2 + e \rightarrow H_2^*(\nu) + e \tag{1.31}$$

$$H_2^*(\nu) + e \rightarrow H + H^- \tag{1.32}$$

The main problems of the volume process are the separation of energetic electrons, that could destroy the H^-, and the negative ion density decrease due to loss mechanism (neutralisation) with energetic electrons. Because of these loss mechanisms, plasma is generated in the driver region and then it diffuses into an *expansion region* (also called tandem plasma chamber) in which a filter magnetic field, that prevents the energetic electron from going into the extraction region and reduces the total number of electrons, is present and lets the exited negative ions free to drift to the extraction region (see fig.1.10).
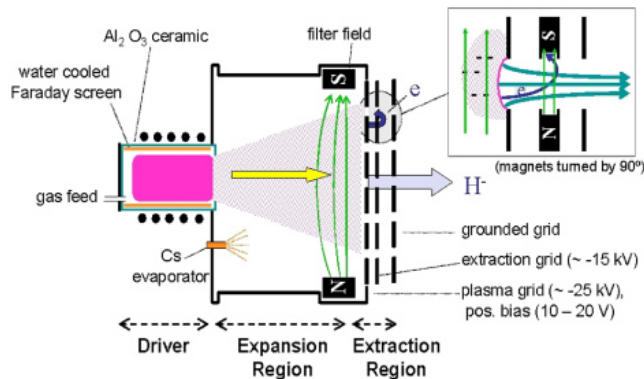

Figure 1.10: Top view of the IPP prototype source [17] [18]

In the expansion region the ion current is increased significantly thanks to caesium seeding into the volume production source: effects both for volume and surface production are discussed in [19] and in [20].
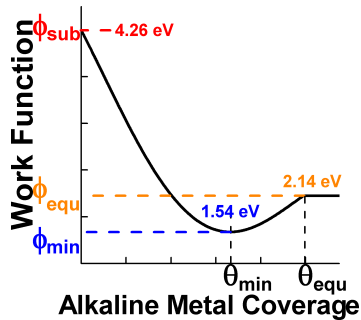
Figure 1.11: General trend of wall work function (molybdenum substrate) with respect to the caesium layer thickness [21] (work function for layer thicker than θ_{equ}) and [22], [23] (work function for layer thinner than θ_{equ}).

In particular, in case of surface production, it is important to lower the work function of the surface that is the site of such process: in this way electrons need less energy to be extracted from the surface and this mechanism enhances the probability to obtain negative ions from positive ions or neutrals impinging the surface. A typical plot for the surface work function is reported in relation to the thickness of the caesium layer deposited on the surface itself(fig.1.11): the work function shows a minimum in correspondence to the value θ_{min} and after this minimum it increases again up to a stable value, the flat region starts from the thickness of θ_{equ} and is the work function of pure caesium. The optimum value of thickness can be controlled by means of the surface temperature so that it is important to keep it controlled and stable.

1.3.2 Extraction, acceleration stages

The extraction and acceleration systems are composed of different potential steps applied to grids that are perpendicular to the beam axis. Basically the system is composed of three grids: the *plasma grid* that is in contact to the plasma volume, the *extraction grid* which extracts the ions from the plasma beam and the *grounded grid* that is kept to the ground potential in order to accelerate the negative ions (for example see fig.2.4). Due to technical reasons, it is easier to keep at high potential the source rather than the tank downstream the acceleration system: indeed the dimensions of the source are much more contained than the dimensions of the tank which includes the beam diagnostics. As a result it is advantageous to choose the smallest volume possible for the high voltage.
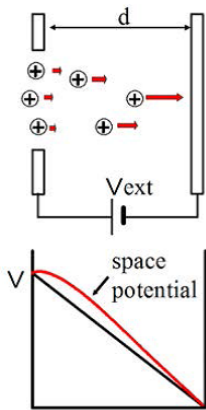

Figure 1.12: Schematics of ion extraction by two electrodes [1]

The number of ions that can be extracted by an applied electrical field from an ideal plane electrode is proportional to the electric field applied between the electrodes and the one due to the space charge located in between the electrodes (fig.1.12). By solving the Poisson equation for planar electrodes the Child-Langmuir Law is obtained (see eq. 1.33[24]).

$$j_{\mathrm{ex}} = \frac{4\epsilon_0}{9}\sqrt{\frac{2Ze}{m}}\frac{U_{\mathrm{ex}}^{3/2}}{d^2} \tag{1.33}$$

where j_{ex} is the extracted current density, Z is the ion charge number, m the mass of extracted ions, d the distance between the electrodes and U_{ex} is the extraction voltage. Taking into account a circular aperture with radius a, it is possible to calculate the current I_{ex} for one aperture. The case of N apertures is shown in eq.1.34.

$$I_{ex} = N\pi a^2 j_{ex} = N\frac{\pi\epsilon_0}{9}\sqrt{\frac{2Ze}{m}}\left(\frac{2a}{d}\right)^2 U_{\mathrm{ex}}^{3/2} \tag{1.34}$$

Then it is possible to write $I_{\mathrm{ex}} = PU_{\mathrm{ex}}^{3/2}$ where $P = I_{\mathrm{ex}}/U_{\mathrm{ex}}^{3/2}$ is called the *perveance* value. It is possible to vary the perveance acting both on the extracting potential U_{ex} or on the extracted current I_{ex}: U_{ex} is fixed by the experimental set-up of the extraction system while, in order to increase I_{ex}, it is possible to increase the power of the RF generators. Increasing the power coupled by the RF generator inside the plasma also increases the dissociation rate (reactions in eq.1.31 and eq.1.32) inside the plasma volume and, in turn, it increases the

amount of neutrals available for surface production [25]. The final result is a higher amount of negative ions that can be extracted.

From the formula 1.34 it is possible to find the maximum extracted current given the extracting potential.

The extraction and acceleration system can be described as a system of lenses because from the plasma volume it is possible to form several small beams called *beamlets*. In figure 1.13 *(a)* the formation of a beamlet from the plasma is shown, while in figure 1.13 *(b)* the beamlet optics at the end of the acceleration stage is depicted. In figure 1.13 *(b)* three cases in which the final width of the beamlet is affected by the grid system parameters are shown. The best perveance is the value for which the beam width is at a minimum; the other two situations in which the beam optics is far from the optimum are called *under-perveant* and *over-perveant* with the perveance value lower and larger than the best perveance value respectively.

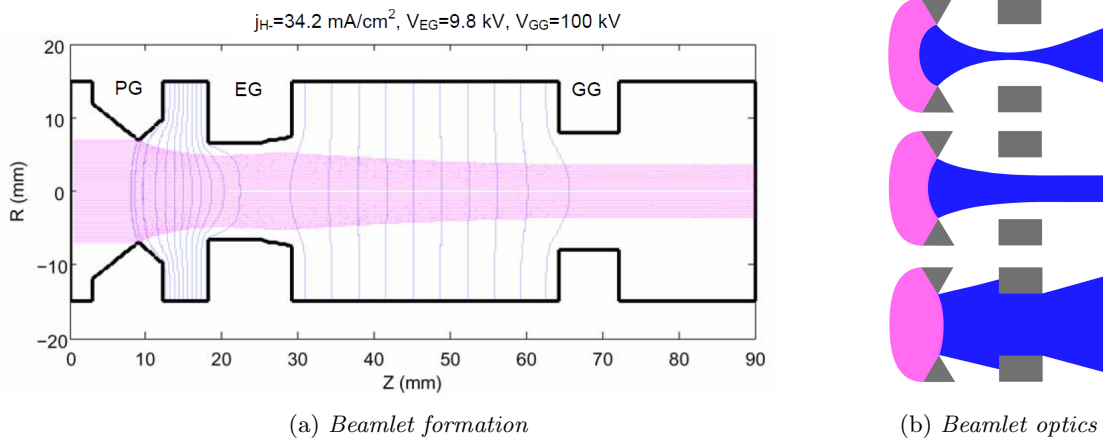(a) *Beamlet formation* (b) *Beamlet optics*

Figure 1.13: Right: SLACCAD simulation of the beam optics: equipotential lines (blue) and particle trajectory (magenta) are estimated by integration of the Poisson's equation [26]; Left: Effect of the perveance on beamlet optics in three different cases: from top to bottom the under perveant case, the best perveance value and the over perveant case.

The electric field acts like a lens focusing or defocusing the single beamlet and, for the acceleration stage, a rectifying effect is expected on the beamlet.

A fraction of the total amount of ions is neutralised in the extraction and acceleration system before being accelerated up to the final desirable energy: this is referred to as *stripping* and calculations performed for ITER estimate a stripping fraction of about 30% [27].

Ion source requirements for ITER NBI have been fulfilled separately in different test facilities such as the ion source prototypes present at the IPP institute whose design is shown in fig.1.10. In BATMAN (**Ba**varian **T**est **Ma**chine for **N**egative ions) in 2005 the requirements for the extracted current densities, the pressure and the electron/ion ratio have been fulfilled with an extraction area of 0.52 m × 0.26 *m* and pulse length < 6 s [18]. The pulse length required for ITER NBI (up to 3600 s) was achieved in MANITU (**M**ulti **A**perture **N**egative **I**on **T**est **U**nit) with an extraction area of 0.03m^2 [18]. Except for an energy of 979 keV reached by Megavolt [28] in Japan, all the studies performed on NBI are at energy lower than 1 MeV (ITER parameters in tab.1.3) therefore, in the framework of the ITER project, a dedicated ITER full size injector [29] is under commissioning at the Consorzio RFX in Padova, Italy. SPIDER [30] (**S**ource for the **P**roduction of **I**ons of **D**euterium **E**xtracted from an **R**F plasma) and MITICA [29] (**M**egavolt **ITER** **I**njector and **C**oncept **A**dvancement) the full size ion source and the injector will be developed in Padova

with two separated testbeds respectively. The IPP test facility ELISE is an intermediate step between SPIDER and the small ion sources MANITU and BATMAN because it has an extraction area of approximately 1000 cm^2 (half the extraction area of the ITER NBI ion source).

Chapter 2

The ELISE test facility

ELISE (**E**xtraction from a **L**arge **I**on **S**ource **E**xperiment) is a negative ion source facility located at IPP in Garching bei München. The experiment aims to achieve an ITER-relevant extracted current density of negative ions at ITER relevant filling pressure and pulse length using an ion source that is half-size of an ITER source and is designed to be an intermediate step between the prototype ion sources of BATMAN and MANITU and the full-size ITER source [18]. The test facility and the beam diagnostics will be described respectively in section 2.1 and 2.2.

2.1   General features of ELISE

The ELISE experiment aims to be as close as possible to the ITER NBI design but with some modifications implemented for a better diagnostic access. An overview of the experiment is given in fig.2.1*(a)* while the experimental parameters are reported in table 2.1. The extraction area of the ion source is approximately 0.1 m^2. The total applied acceleration voltage is 60 kV instead of 1 MV required for ITER: this difference is due to the purpose of the ELISE experiment that mainly aims to develop the ion source and not the acceleration system.

Isotope	H, D (limited)
Extraction area	1000 cm^2
Apertures	640 with ∅ 14 mm
Source size (expansion region) (W × H × D)	1.0 m × 0.86 m × 0.235 m
U_{HV}	60 kV
U_{ex}	≤ 12 kV
P_{RF}	360 kW
Pulse length:	
Plasma	Up to 3600 s
Extraction	10 s every 180 s

Table 2.1: Parameters of the ELISE experiment [31].

The experiment is placed inside a concrete shell for radiation protection due to neutron production during D^- operation. The ion source is shown in fig.2.1*(b)*.

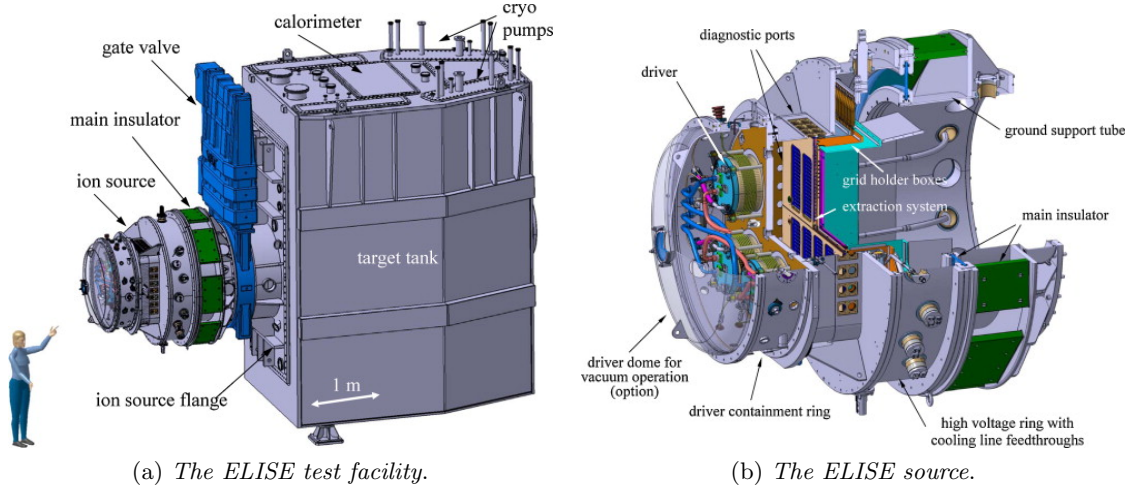(a) *The ELISE test facility.* (b) *The ELISE source.*

Figure 2.1: right: The ELISE test facility; left: ELISE source with the extraction system and the HV insulation [32].

The four drivers for the ELISE facility, whose design is shown in fig.2.2, have a cylindrical shape: the RF coils, connected to an oscillator (1 MHz frequency, power $\leq$ 180 kW, continuous wave operation) are wound up around a Al_2O_3 cylinder and the back is covered by the so called *driver black plate*. Permanent magnets are mounted in the driver back plate to reduce plasma losses on it. A water-cooled Faraday screen shields the alumina cylinder from the erosion of the plasma [18]. The plasma parameters inside the driver are about $T_e \approx 10\,\text{eV}$ and $n_e \approx 10^{18}\,\text{m}^{-3}$ [17]. Two of the drivers are equipped with a starter filament that, through thermionic emission, produces the first electrons to ignite the plasma. In the driver back plate the gas supply is also present.
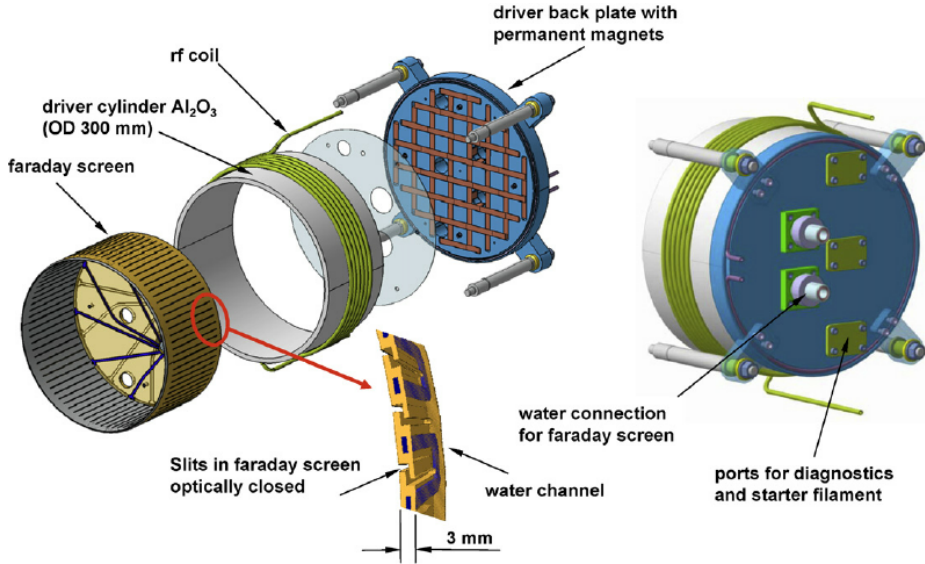

Figure 2.2: Design of a ELISE driver [32].

Downstream of the driver region there is the expansion region: inside this region the caesium is injected (see sec.1.3.1). Two caesium ovens are installed at the sides of the source with nozzles pointing towards the drivers. The evaporation rate of the ovens is measured by surface ion detectors (SID) [33].

The beam is composed of negative ions created by positive ions and neutrals impinging the first grid facing the plasma; the trajectories of negative ions are bent due to the extraction

16

potential and the particles flow inside the grid system. Each small beam is created in correspondence to the apertures on the grids: in the case of ELISE the apertures of the grids are aligned, the negative ions in the vicinity of the apertures react to the extraction voltage and a small beam, called *beamlet*, is extracted from the plasma.

The number of the apertures is 640 grouped in 8 main groups, each one called *beamlet group*. For each beamlet group there are 80 apertures arranged in 16 rows of 5 beamlets: the design of the apertures is shown in fig.2.3 *(a)* while in fig.2.3 *(b)* the arrangement of the apertures in the grid is shown.

(a) *Design of the apertures*
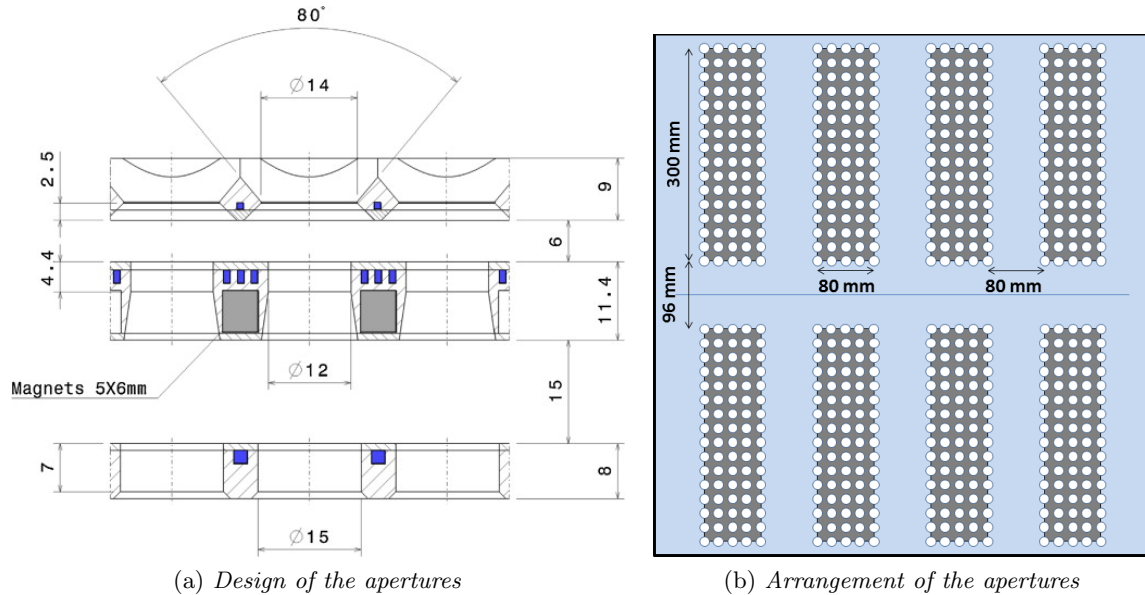

(b) *Arrangement of the apertures*

Figure 2.3: Left: Design of the apertures [31]; Right: arrangement of the apertures in the grid system.

ELISE is equipped with a *bias plate* mounted at 7 mm above the plasma grid and coated with molybdenum on the side in contact with the plasma. 8 windows are designed in correspondence to the beamlet groups, 12.5 mm larger than the edges of the apertures in all directions (fig.2.4*(a)*) [31].

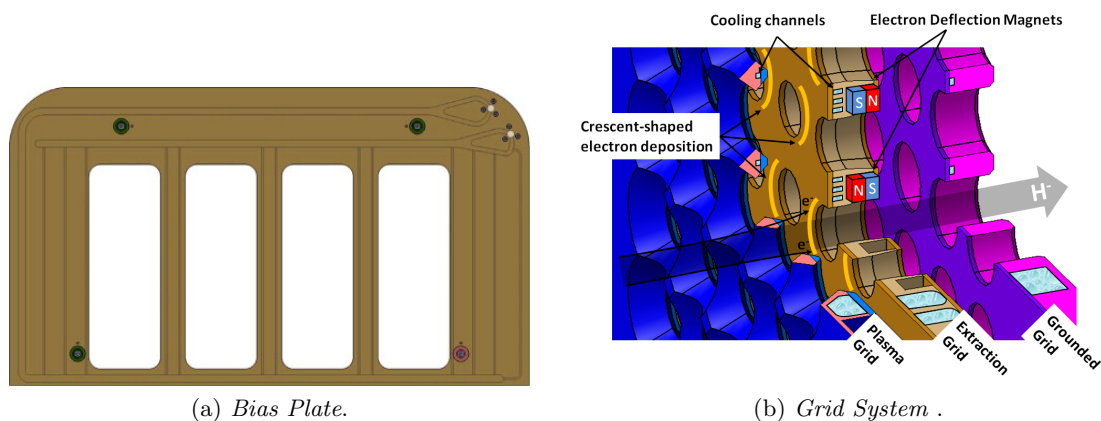(a) *Bias Plate.*

(b) *Grid System .*

Figure 2.4: Left: bias plate top segment with window frame like openings and embedded cooling channels. It is electrically insulated with respect to the PG [31]; Right: section of the three-grid extraction system: plasma grid (PG), extraction grid (EG) and grounded grid (GG)

The bias plate extends the source body potential towards the plasma centre. The result is a change in the potential distribution in the source volume close to the plasma grid that leads to a reduction of the co-extracted electrons [34]. For more stable operations, the potential difference is current-driven and in this work we will refer to the bias current I_{Bias}. The main purpose of the bias is to diminish the amount of electrons near the plasma grid and consequently decrease the number of electrons that pass the first grid. On the top part of figure 2.5 the effect of the bias on the extracted ion current density and on the electron/ion ratio is shown: the first is not greatly affected by the bias variation, the latter instead shows a strong decrease (about a factor 4).
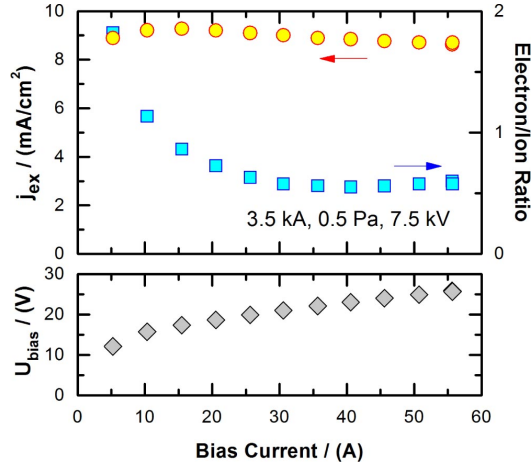

Figure 2.5: Top: effect of the bias current on the source performance at the test facility ELISE: extracted current density (in yellow) and electron to ion ratio (in blue). Operation in hydrogen, $U_{ex} = 7.5$ kV, $I_{PG} = 3.5$ kA, source filling pressure of 0.5 Pa. Bottom: bias voltage dependence on bias current [33]

The extraction and acceleration system is shown in fig.2.4(b). The first grid facing the plasma is the *Plasma Grid* (PG) and it is responsible for beamlet creation: the surface that faces the plasma is the site for surface ion production. The filter field is created by a current called *plasma grid current I_{PG}* that flows from the bottom to the top. The effect of the filter field on the ratio of extracted electron/ion and on the extracted ion current density is shown in figure 2.6. The second grid is the *Extraction Grid* (EG) usually kept at $U_{\text{ex}} = 2 - 11$ kV positive potential. The third grid represents the acceleration stage and is called *Grounded Grid* (GG) because it is at ground potential. The grids are cooled by a complex system of embedded water channels. The electric scheme of ELISE is shown in figure 2.7.

(a) *Effect of the PG current on the source performance*

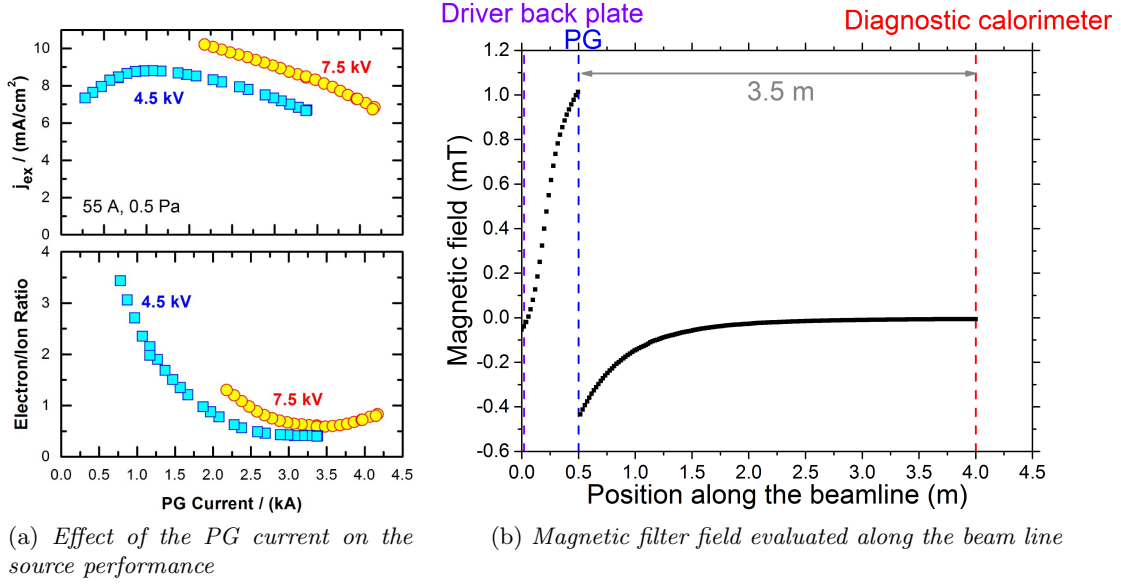(b) *Magnetic filter field evaluated along the beam line*

Figure 2.6: Left: Effect of the PG current on the source performance at the test facility ELISE for different extraction voltages. Top: negative ion extracted current density. Bottom: Electron to ion ratio. Operation in hydrogen, source filling pressure of 0.5 Pa, bias current 55 A [33]. Right: Magnetic filter field due to a $I_{\mathrm{PG}} = 1$ kA plotted from the driver back plate to the beam dump (represented by the diagnostic calorimeter) along a line parallel to the beamline, courtesy of Riccardo Nocentini
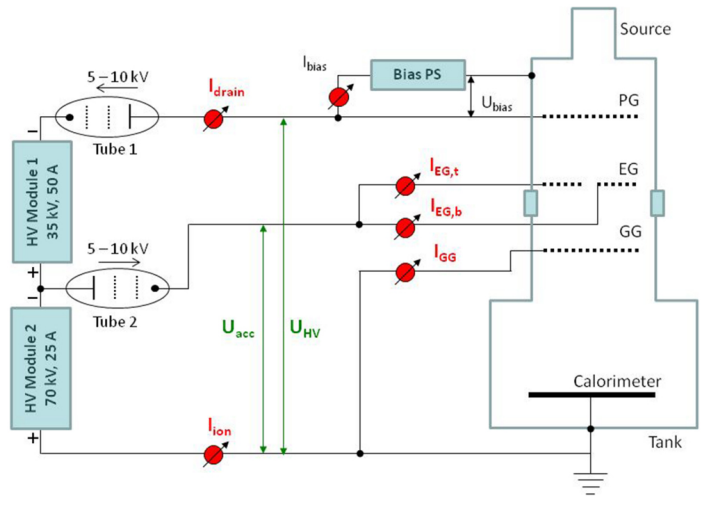

Figure 2.7: Scheme of the HV circuit of ELISE with the voltage and current measurements. The voltage is regulated by tetrodes [35].

In the experimental set up it is possible to vary the total high voltage U_{HV} up to 60 kV and the extraction voltage U_{ex} up to around 15 kV: the acceleration voltage (U_{acc}) is then the difference between those two ($U_{\mathrm{acc}} = U_{\mathrm{HV}} - U_{\mathrm{ex}}$) [36]. The electrical currents flowing onto each grid and the total current back to the HV power supply are measured separately: the currents flowing to the EG and the PG can be caused by both electrons and negative ions but it is reasonable to assume that they are only due to electrons for the EG and due to ions and electrons for the PG, while for the GG are assumed only a small amount of ions (the majority passes and reach the calorimeter).
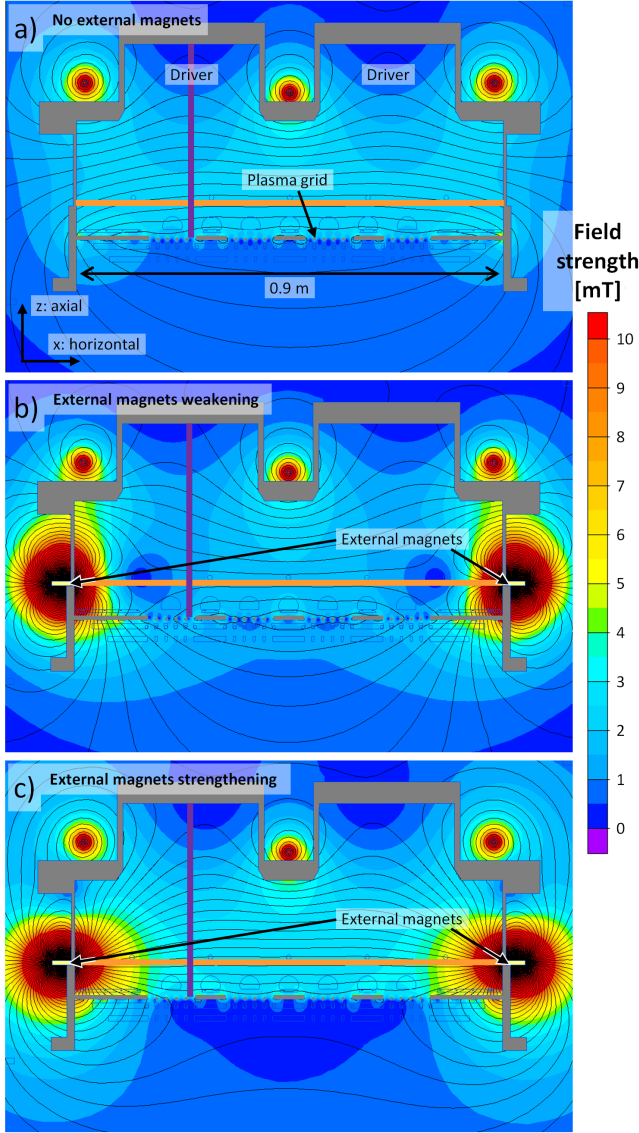
Figure 2.8: 2D structure of the field strength resulting in ELISE from the superposition of the PG filter field (I_{PG} = 2.5 kA) and external magnets. a) Standard field, without external magnets. b) External magnets in the weakening configuration. c) External magnets in the strengthening configuration [37]. In the picture are also shown the returning conductors placed on the sides of the drivers.

It is possible to place external permanent magnets in the expansion region: the resulting field can strengthen or weaken the filter field created by the PG current. A plot of the possible configurations with the simulation of the resulting magnetic field is shown in fig.2.8. These magnets are located in the plasma region in order to study the effect of the magnetic field on the plasma properties in the source region. The PG filter field changes its sign at the PG position while the magnets affect both the plasma and the beam downstream of the PG by a magnetic field with the same sign (see fig.2.6 (b)): in the case of the weakening configuration the external field and the filter field have different signs in the plasma region and the same sign in the beam region, for the case of the strengthening configuration is vice-versa. The plasma drift and the beam deflection, due to the $E \times B$ drift (eq.1.24) and to the Lorentz's force (1.18) respectively, are difficult to define quantitatively because it is not possible to divide clearly the effect or to investigate the effects on the beam and on the plasma separately. In addition to that, in a long distance the magnets can affect also the beam after the grid system but in a negligible way compared to the vicinity of the permanent magnets.

The optics of a beam can be described through the perveance P, defined by eq.2.1:

$$P = \frac{I}{U_{ex}^{3/2}} \qquad (2.1)$$

In the case of ELISE, I is the electrically measured ion current (in the figure 2.7 I_{ion}) and U_{ex} is the difference between U_{HV} and U_{acc}. The maximum value of perveance P_0 can be calculated through the use of eq.1.34 and it is completely determined by the geometry of the grids and by the ion type: for ELISE, the value for the maximum perveance is $P_0^H = 14.84 \cdot 10^{-5}$ in hydrogen and $P_0^D = 20.99 \cdot 10^{-5}$ in deuterium. The value P/P_0 is evaluated for every shot. It is important to highlight that the perveance value P is a locally averaged value and it does not take into account local variations of the extracted ion

current: in the case of ELISE the 8 beamlet groups, in most cases, overlap and constitute 2 beam *segments* on the calorimeter. Image 2.10 *(b)* shows the temperature profile and the two beam segments are clearly distinguishable with a different heat distribution. The beam segments have different power deposition and consequently different ion current while the extraction voltage is the same for both segments: the result is a different perveance value associated with the two parts.

It is useful to say a few words on how all the measurements and diagnostic results are stored: for each beam pulse (see sec.3.2 for a better description of the operations in ELISE) a univocal number is assigned and all the signals (separately stored as video, plain text, images, spectra and so on) relative to that beam pulse are renamed with this number. In order to assign the correct name, the timing of the trigger and the creation date of the file are compared. The raw data from the diagnostics are stored in large hard drivers and the results from the analysis made on that signals are collected in several databases, each one connected to different group of diagnostic or to a single diagnostic from which it is possible to retrieve several information (for example the manometer gives only one pressure value while from a spectrum it is possible to obtain the width and the height for all the spectral lines).

Databases are text files, created for each day and named like $YYYY\_MM\_DD.txt$, containing several lines one for each beam pulse performed on that day. In every line the first field in the pulse number and following fields are the beam pulse main parameters (set up parameter, beam duration etc.); the following parameters can be general or related to a specific diagnostic. Each field is separated from the next one by the symbol |. The main database for example reports set-up parameters from the drivers and the grids, pressure values measured in different positions along the beam-line, electrically measured currents, water calorimetry of the beam dump and other general parameters on the beam such as the normalized perveance. Other databases come from the beam emission spectroscopy (see sec.2.2.3) and from the optical emission spectroscopy. Some diagnostics, such as the diagnostic calorimeter and the tungsten wire calorimeter, do not have an automatic routine that analyses the raw data, therefore are used in a qualitative way (immediate check during the beam pulse). The first part of this work aims to create a database for all the old operating days and for future beam pulses.

2.2 Beam diagnostics

In ELISE the beam is characterized by means of three beam diagnostics along the beam line: a tungsten wire calorimeter, beam emission spectroscopy (BES) and a diagnostic calorimeter. The set up is shown in fig.2.9: the support for the BES and for the tungsten wire calorimeter is the same and is placed at $1.8\,m$ from the grounded grid, while the diagnostic calorimeter, which works also as beam dump, is placed at 3.5 m from the GG.
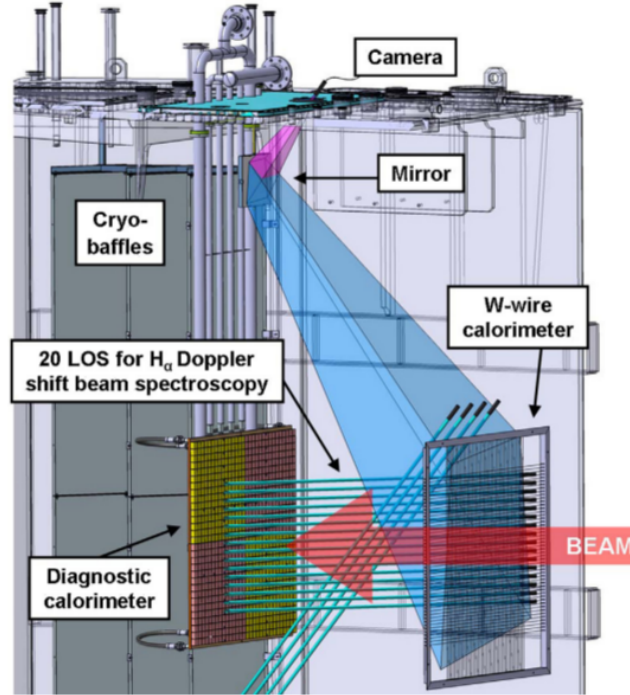

Figure 2.9: Beam diagnostics of ELISE test facility [38]

2.2.1 Diagnostic calorimeter

The diagnostic calorimeter has the main function to stop the beam and to perform an analysis of the beam itself. For this purpose in the calorimeter thermocouples of type K are installed whose positions are shown in fig.2.10 *(a)*. Another diagnostic is water calorimetry: in this case the analysis is performed by measuring the temperature difference in the water flowing inside the pipes used for the cooling system. In addition, an infra-red camera looks at the calorimeter from a distance of about 2 m through a window in the vacuum vessel in order to evaluate the beam imprint on the surface: the goal of this thesis is to elaborate the data from the IR camera and to obtain a quantitative analysis of the 2D profile of the beam.

The calorimeter is made of copper and segmented in 30×30 blocks whit a square surface of $0.038\,m \times 0.038\,m$ and a thickness of $0.025\,m$. The blocks are adjacent to each other with 2 mm gap. The total calorimeter surface is $1.2\,m \times 1.2\,m$. The bottom of the calorimeter, to which the blocks are connected, is composed of four plates (fig.2.10(a)). The surface of the calorimeter facing the beam is coated, in order to reduce the reflectivity, with a blackening molybdenum disulfide coating (D-321R) [39].

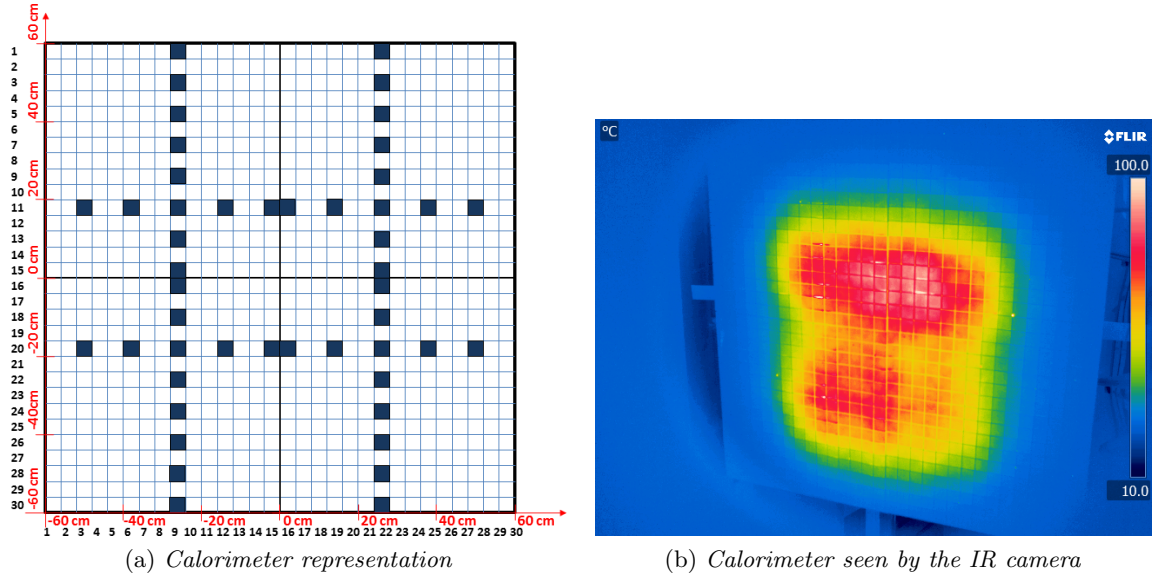(a) *Calorimeter representation*   (b) *Calorimeter seen by the IR camera*

Figure 2.10: Left: the diagnostic calorimeter of ELISE is made of 4 plates (thick black squares). Each plate is slotted in such a way to form 15×15 square elements (shown in thin blue lines). Blue squares show the blocks in which thermocouples are integrated [38]. The numbers on the left side and on the bottom enumerate the blocks inside one column or one row, red axes describe the reference system chosen for the following analysis. Right: frame captured by the IR camera during the beam.

The segmentation on the calorimeter surface reduces transversal heat conduction and allows the analysis of the beam profile through the measure of the temperature distribution on it. A IR camera FLIR A655sc (focal length 13.1 mm, field of view FOV $45° \times 33.7°$, F number $f/1.0$, spectral band $7.5 - 14~\mu$m [40])is used for the temperature measurement. The IR camera has a resolution of 640×480 pixels and it looks at the calorimeter though a port in the tank, part of the port is visible from the camera view. An example of one frame captured by the IR camera is shown in fig.2.10*(b)*. The perspective of the camera view is inclined because the camera looks at the calorimeter from one side of the tank. The analysis of the calorimeter will be discussed in the following chapters.

2.2.2 Tungsten wire calorimeter

The tungsten calorimeter is positioned at 1.8 m from the GG and is composed of 100 tungsten wires with a diameter is 0.2 mm. The wires are placed in two planes perpendicular to the beam axis: in the first plane the wires are drawn vertically and in the second one horizontally; the two planes are spaced 10 mm. The ion beam heats the W calorimeter up to 2600 K and the thermal equilibrium is reached in about 1 s. The wires are held by a system of small springs that keep the wires stretched: those holding systems avoid the wire bending due to the thermal expansion. The light emitted due to black body emission is collected by an optical CCD camera situated out of the vessel (through the reflection on a front surface mirror). From the light intensity emission it is possible to retrieve information on the beam profile: it is noticeable that for low beam divergence the eight beamlet groups are distinguishable (e.g. fig.2.11) [38].
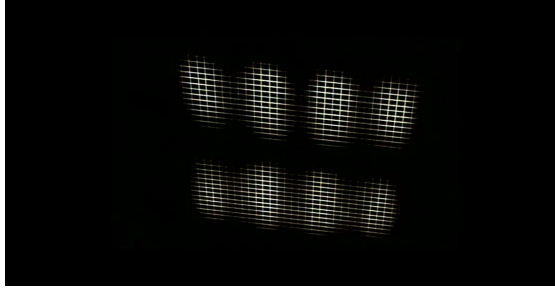
Figure 2.11: Image of W-wire calorimeter

2.2.3 Beam Emission Spectroscopy (BES)

Placed at 1.8 m from the GG and installed on the same support as the tungsten wire calorimeter, the H_α Doppler shift beam emission spectroscopy (BES) is allocated. This diagnostic is composed of 20 lines-of-sight (LOS) each one measuring the light emission from the H_α line at a certain position: in this way it is possible to characterize quantitatively the beam at ELISE measuring divergence and stripping losses (see chapter 1.3.2).

The LOS are arranged along 2 different axes: 16 are placed in the vertical direction (50 mm spacing) and investigate the vertical beam profile and 4 are in the horizontal direction (160 mm spacing) in order to investigate the horizontal beam profile. The lines-of-sight are not looking perpendicularly to the beam: the collimator lenses are inclined with a 50 degree angle (see fig.2.9) and the light collected is transmitted by optical fibers to an Acton spectrometer with a focal length of 0.75 m [38]. The performed measurement is the integral along the line so that the information acquired are referred to the entire path along the LOS.

The physical principle behind the spectroscopy is the Doppler effect applied to a particle moving with velocity v: the light emitted by the particle upon interaction with the background gas is shifted from the spectral value in a rest frame and the obtained wavelength is reported in eq.2.2. In the case of BES the angle θ between the trajectory of the emitting particle and the optic axis introduce a correction to the formula.

$$\lambda = \frac{1 + \beta \cos \theta}{\sqrt{1 - \beta^2}} \lambda_0 \qquad (2.2)$$

where $\beta = v/c$ and c is the speed of light. An example of output signal is the spectrum plotted in fig.2.12 (a) : the unshifted H_{alpha} peak is at $\lambda_0 = 656.3\,nm$ due to slow particles (first peak from right), the second peak is the so-called stripping peak caused by ions that are neutralized (lose their extra electron) before being accelerated up to the final energy (see sec.1.3.2, calculation in [27]) and the third one is the Doppler-shifted peak and corresponds to the energy of the neutrals accelerated to full energy E_{tot}. The Doppler peak width ε is correlated to the beam divergence. From the height and the width of the Doppler peak the beam intensity and beam divergence respectively are retrieved. The stripping peak is corresponding to the energy of the extraction stage E_{ex} and the integral value of the stripping peak I_s with respect to the Doppler peak I_m represents the stripping fraction f_s.

As explained, the analysis of the Doppler peak gives information on the divergence along that line: a Gaussian fit is performed on the Doppler peak in order to obtain the full width half maximum (FWHM) that represents the divergence ε.
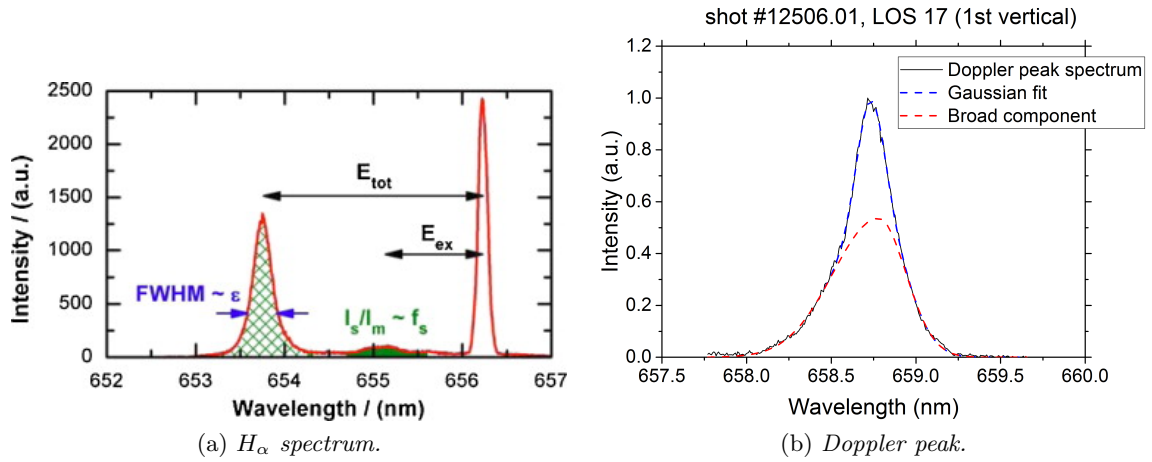
(a) H_α spectrum.

(b) *Doppler peak.*

Figure 2.12: In *(a)* the H_α Doppler shift spectrum of a typical negative hydrogen ion beam is shown (from the MANITU testbed) [38]. In *(b)* an example of a fit on the Doppler peak is shown: in blue the Gaussian fit of the peak and in red the asymmetric Gaussian fit for the broad component. Courtesy of Marco Barbisan.

Investigations on the shape of the Doppler peak point out the presence of an asymmetric component with a larger width: this component can be identified because it enlarges the peak basis [41].This fraction of the peak, the so-called *broad component*, can be estimated with a Gaussian fit but the real shape is impossible to retrieve: the analysis only improves the fit on the left and right tail of the peak. In figure 2.12 *(b)* an example of Doppler peak fitted with a Gaussian function and a possible fit for the broad component are shown.

In order to investigate the broad component two half Gaussian curves with different width are superimposed to the normal peak. The reliability of the beam width value retrieved from the BES spectra depends on the correctness of the fit on the Doppler peak and, consequently, on the fitting formula chosen for the broad component.

Some results in order to better understand the broad component and how it affects the beam are shown in section 4.7.

Chapter 3

IR analysis of the calorimeter

3.1 General principles of thermography[42]

A black-body radiator is an object that theoretically absorbs radiation at all the possible wavelengths to which it is exposed and emits radiation at any wavelength. More precisely, the *Kirchohhof law* also states that the emissivity $\varepsilon(\lambda)$ and the absorptance $\alpha(\lambda)$ are the same at the same wavelength λ.

The spectral distribution of black-body radiation is given by the *Planck law* that calculates the intensity of radiation w_λ for the wavelength λ (eq.3.1):

$$w_\lambda = \frac{8\pi h c^2}{\lambda^5 \left(e^{\frac{hc}{\lambda k_{\mathrm{B}} T}} - 1 \right)} \tag{3.1}$$

where c is the speed of light, h is the Planck constant, k_{B} is the Boltzmann constant and T is the temperature of the black-body radiator. The wavelength $\lambda_{\max}$ for which the maximum of intensity occurs depends on the temperature T and is described by the *Wien law* eq.3.2:

$$\lambda_{\max} = \frac{b}{T} \tag{3.2}$$

where $b = 2898\,\mu\mathrm{m} \cdot \mathrm{K}$ and T is expressed in K. By integrating Planck law over all possible wavelengths (from $\lambda = 0$ to $\lambda \to \infty$), eq.3.3, i.e. the *Stefan-Boltzamann law*, is obtained:

$$W = \sigma T^4 \tag{3.3}$$

where W is the total radiation emitted, σ is the so called Stefan-Boltzmann constant and T is the temperature in kelvin. A real object behaves quite differently from a black-body radiator and in particular the absorption and emissivity coefficients are lower than unity. The light impinging on the object can undergo three different processes: radiation can be absorbed, reflected or transmitted through the object, described by the absorptance (α_λ), reflectance (ρ_λ) and transmittance (τ_λ) coefficients respectively. These coefficients obey to eq.3.4 (valid for each λ):

$$\tau_\lambda + \rho_\lambda + \alpha_\lambda = 1 \tag{3.4}$$

The emittance of a real object is lower than the one of the blackbody and is described by a coefficient, the emissivity ϵ, that ranges from 0 to 1 (1 represents the black-body radiator): so the total emitted radiation by a real object is described by eq.3.5.

$$W = \epsilon \sigma T^4 \tag{3.5}$$

Upon knowing the radiation emitted and the emissivity ϵ it is possible to retrieve the temperature of the object .

In order to properly analyse the radiation emitted by an object, it is important to take into account the environment in which both the object and the detector are placed. The scheme in figure 3.1 represents the situation of interest in the case of ELISE.
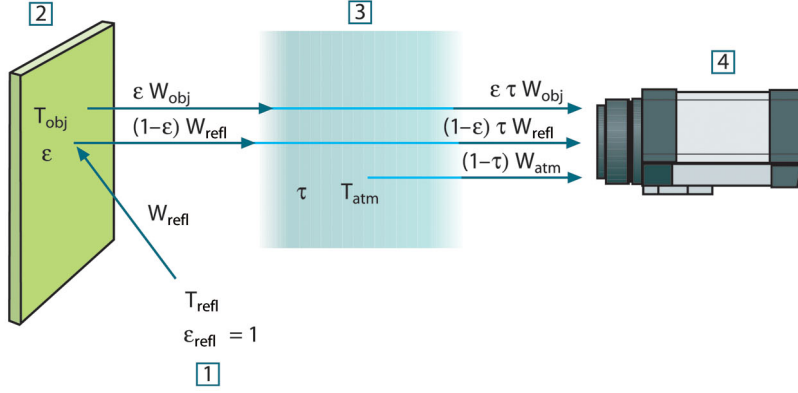

Figure 3.1: A schematic representation of the general thermographic measurement.1: Surroundings; 2: Object; 3: Atmosphere; 4: Camera.[42]

Figure 3.1 reports the reflected emission with a power W_{refl}(as a black-body emitted power) emitted by the environment at T_{refl}; it also shows the temperature of the object T_{obj} and its emitted power W_{obj} (again as a black body radiation) and eventually the atmosphere with its temperature T_{atm} and its emitted power W_{atm} are shown. These quantities must be corrected with the correspondent coefficients and the total power collected by the detector is:

$$W_{\text{tot}} = \tau \epsilon W_{\text{obj}} + \tau (1 - \epsilon) W_{\text{refl}} + (1 - \tau) W_{\text{atm}} \qquad (3.6)$$

The corresponding signal, indicated with S_{tot}, is proportional to W_{tot}. S_{atm} and S_{refl} can be estimated from T_{atm}, T_{refl}, d that is the distance between the camera and the calorimeter and from the emissivity ϵ. These parameters are given to the software that elaborates the results. S_{obj} is given by eq.3.7.

$$S_{\text{obj}} = \frac{1}{\epsilon \tau} S_{\text{tot}} - \frac{1 - \epsilon}{\epsilon} S_{\text{refl}} - \frac{1 - \tau}{\tau \epsilon} S_{\text{atm}} \qquad (3.7)$$

From S_{obj} (in digital units) it is possible to calculate the radiation emitted by the object M:

$$M = \frac{S_{\text{obj}} - J0}{J1} \qquad (3.8)$$

where $J0$ and $J1$ are calibration constants of the IR camera processing software. The emitted radiation (in W/m^2) is given by:

$$M(T) = \int r(\lambda) M(\lambda, T) d\lambda \qquad (3.9)$$

where $r(\lambda)$ is the response of the camera with respect to the wavelength and $M(\lambda, T)$ is the Planck law. Then the integral is approximated by:

$$M(T) \approx \frac{R}{e^{B/T} - F} \qquad (3.10)$$

where R, B and F are chosen to best fit eq.3.10 and are provided by the manufacturer of the infra-red camera. Finally the temperature T_{obj} is given by eq.3.11.

$$T_{\text{obj}} = \frac{B}{log(\frac{R}{M_{obj}} + F)} \qquad (3.11)$$

3.2   Data processing

ELISE operates in different experimental conditions in order to investigate physical properties of the plasma and the beam. It is possible to perform long plasma pulses (usually up to 3600 s) but, due to available HV power supply, extraction can only last for short time (10 s every 180 s): due to this it is possible that inside the same plasma pulse different beam blips take place and it is important to report in the database all the measured values from the diagnostics during both the HV phase and the plasma phase for each extraction. All the measurements are recorded continuously but the values reported in the database are calculated by averaging each single value in a temporal window: in the second half of the beam pulse for the HV phase and 1.5 s before the end of the RF phase. The measurements are taken in two different intervals during the time trace in order to be able to assess the influence of high voltage phase on the signals collected during the extraction phase (plasma blips). Figure 3.2(b) shows the typical phases of a pulse at ELISE with respect to the H_α emission: the first phase shows the U_{HV} pre-trigger, which occurs some time before the U_{HV} is switched on: this time is needed in order to ignite the plasma at increased power and to reach the plasma stabilisation; the second represents the HV phase and the third the plasma phase[43].
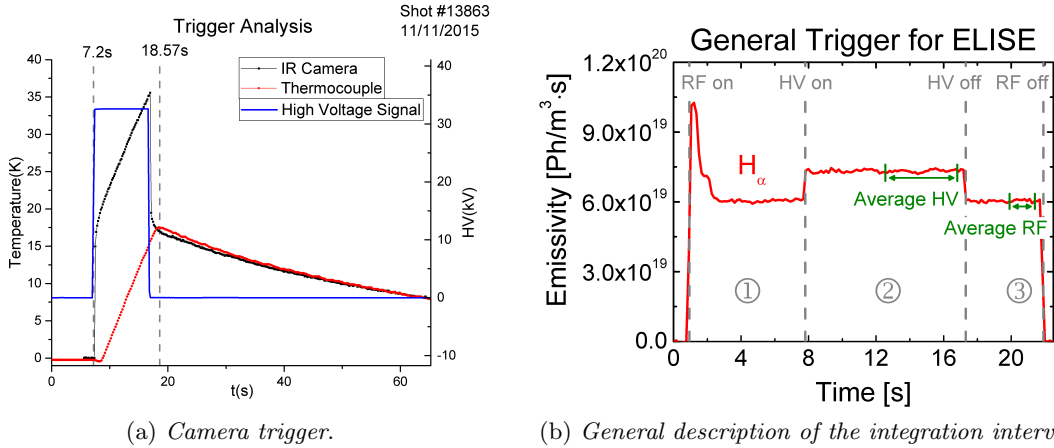
(a) *Camera trigger.*   (b) *General description of the integration intervals.*

Figure 3.2: Description of the time traces from different signals. Figure *(a)* shows the temperature difference of one block of the calorimeter (in black) compared with the thermocouples signals(in red): the temperature during the extraction phase increases significantly and about 2 s after the HV phase the temperature retrieved by the IR analysis and the one measured by thermocouples match together. Figure *(b)* describes the H_α signal (from the BES) during the typical phases of a pulse at ELISE[43].

The IR camera looks directly to the diagnostic calorimeter through a window situated on the vacuum vessel. The camera starts recording with a frequency of 6.25 Hz accordingly to the high voltage trigger and stops after one minute. The records are stored and renamed according to the shot number. For every operational day the focus of the camera should be adjusted in the morning. In figure 3.2(a) time traces of the signals from the IR camera, from the thermocouples and from U_{HV} are shown: during the extraction phase the temperature calculated from the IR camera is overestimated. The phenomenon can occur due to a not perfect adhesion of the blackening layer to the surface: this layer, before thermalizing with the copper surface, emits an intense black-body radiation; Another hypothesis is the presence of particles that are removed from the surface by the beam and that emit a strong radiation. About 2 s after the HV off the temperature matches the thermocouple measurements. This shape of the signal from the IR camera does not affect the calorimetry results: indeed the

main point is that the measure consists in the subtraction of the environment temperature from the final temperature. Therefore the main point is to choose properly two frames from the video clip taken by the IR camera that represent the two temperatures: the first frame is chosen taking into account a precise amount of time from the RF power on (the same time as the U_{HV} pre-trigger) and the second frame is chosen by adding to the U_{HV} pre-trigger the beam duration and the time necessary to the signal to match the thermocouple signal (eq.3.12 and 3.13).

$$\text{Frame}_1 = t_{\text{U}_{\text{HV}}} f_{\text{FLIR}} \tag{3.12}$$

$$\text{Frame}_2 = (t_{\text{U}_{\text{HV}}} + t_{\text{BD}} + t_{\text{DT}}) f_{\text{FLIR}} \tag{3.13}$$

where $t_{U_{HV}}$ is the HV pre-trigger, t_{BD} the beam duration, t_{DT} is the delay after the beam off and f_{FLIR} is the recording frequency (6.25 Hz) of the IR camera. In figure 3.2(a) the frames for the selected shot are indicated in dashed lines.

Figure 2.10(b) shows a frame taken during a beam blip: it is noticeable that the perspective is inclined. The distance between the IR camera and the center of the calorimeter is 2 m and a minor part of the calorimeter (three blocks placed bottom right) is not seen by the camera. As explained in section 2.2.1 the surface of the calorimeter is segmented and the frame is composed of 30×30 blocks. In order to avoid transversal heat conduction, each block is separated from the others by a small gap: this gap should not be taken into account in the thermographic evaluation (in figure 2.10(b) the calorimeter without the pixels in correspondence to the insulating gap). The gaps are described through lines in the image (fig.3.3(a), the lines were calculated by Antonio Pimazzoni in [44]) which are converted in pixels and subtracted from the original image (fig.3.3(b)); two additional pixels from the sides of the lines (left and right for vertical lines and up and down for the horizontal) are removed from the image (particular in fig.3.3(c)). This analysis is performed for both frames (before and slightly after the beam blip).
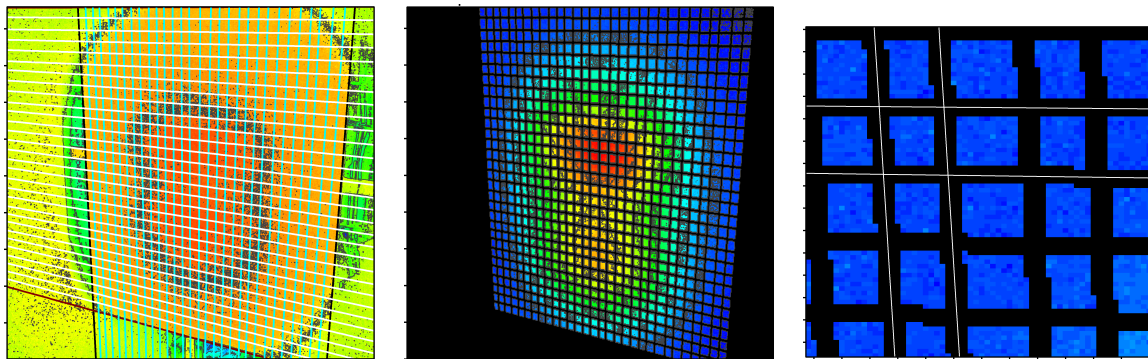
(a) *Insulating gaps described by lines.* (b) *Image without outer parts and insulating gaps.* (c) *Particular.*

Figure 3.3: Left: calorimeter seen by the IR camera and lines that describe the insulating gaps; Center: results from the subtraction of the insulating layers and outer portions; Right: Pixels inside the blocks are coloured, while the pixel in correspondence to the insulating layer are removed (in black), the lines that corresponds to the insulating gaps are plotted in white.

Every file recorded from the IR camera is converted into an ASCII file containing two 640×480 matrices that correspond to the two frames used for the analysis. Each frame is an image that contains the signals in digital units, namely the units used by the camera to store the signal value onto each pixel. By using the formulas reported in section 3.1 a matrix of 640×480 radiance values is generated. From the radiance it is possible to find the temperature through the emissivity (see eq. 3.6). The temperature is calculated for each pixel and the temperature of a block is found by averaging all the pixels inside the block.

From the temperature also the power density and the current density can be determined using eq. 3.14 and eq. 3.16 respectively.

$$P_{dens} = \frac{c_{Cu} m \Delta T}{t_{BL} l^2} \tag{3.14}$$

where P_{dens} is the power density i.e. the deposited power per unit surface, c_{Cu} is the copper specific heat (390 j/kg K), m is the mass of one block (eq. 3.15), t_{BL} is the beam duration in seconds, $l = 0.038$ m is the dimension of one block.

$$m = l^2 h \rho = V \rho \tag{3.15}$$

where $h = 0.025$ m is the thickness of one block and $\rho = 8920$ kg/m^3 is the copper density.

$$j = \frac{P_{dens} l^2}{U_{tot} S} = \frac{P}{U_{tot} S} \tag{3.16}$$

where P is the power on one block, U_{tot} is the HV potential applied and $S = 985$ cm^2 is the total surface considering all the apertures $(640 \times \pi (0.7 \, \text{cm})^2)$. The results from the analysis are shown in fig.3.4(a), (b), (c).

(a) *Temperature difference.*

(b) *Current density.*
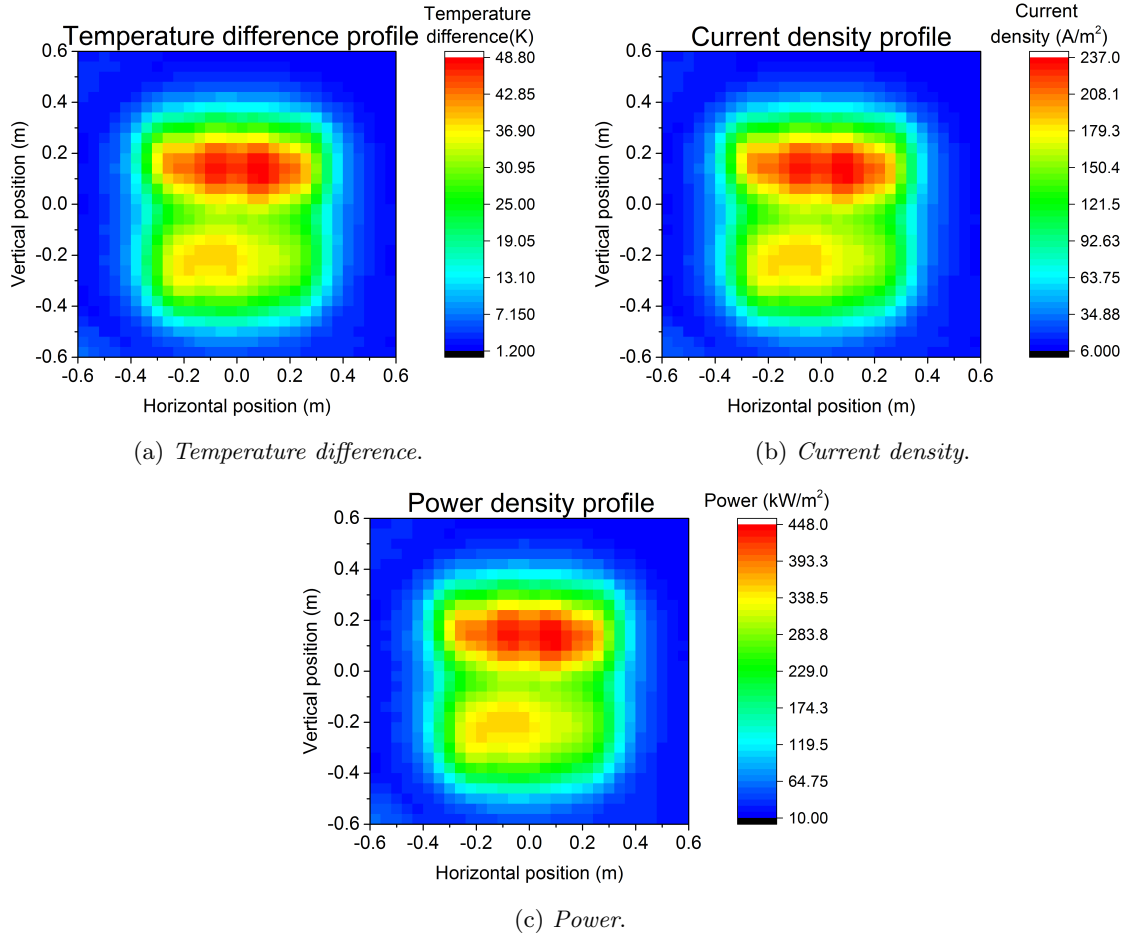
(c) *Power.*

Figure 3.4: 2D plots of the 30×30 blocks of the calorimeter shot #13294.01

What is obtained till now are 30×30 matrices that describe the temperature variation between the two frames under investigation, the power and current deposited by the beam on the calorimeter.

The next step is extrapolating the beam parameters from the $2D$ profile given by the power matrix: a two dimensional fit is performed on the power profile. A detailed discussion

on the fitting formula is given in [44]. The fitting formula is a linear combination of eight bi-dimensional Gaussian functions, each centered at the geometric projection of the beamlet group center on the calorimeter. During the fitting procedure one single horizontal width and one single vertical width are used for all Gaussian functions of the top segment; analogously two other values are used for all Gaussian functions of the bottom segment.

The width of those guassians is supposed the same along the vertical and horizontal direction but different for the beam top and bottom. The formula is reported in eq.3.17.

$$ f(x,y) = \sum_{i=1}^{4} A_i exp\left[-\frac{(x-x_i)^2}{2\sigma_{x_{top}}^2} - \frac{(y-y_{top})^2}{2\sigma_{y_{top}}^2} \right] + \sum_{i=5}^{8} A_i exp\left[-\frac{(x-x_i)^2}{2\sigma_{x_{bot}}^2} - \frac{(y-y_{bot})^2}{2\sigma_{y_{bot}}^2} \right] $$
(3.17)

The parameters consist in the amplitudes A_i with $i = 1\ldots8$, the widths σ_x^{top} σ_x^{bot} σ_y^{top} σ_x^{bot} and the position of the centers of the beam segment top and bottom y_{top} and y_{bot} for the top and bottom beam segments respectively. The positions of the Gaussian function peaks are described by x_i along the horizontal direction and by y_{top} and y_{bot} along the vertical direction. The values x_i are given by the geometric projection of the beamlet group centers on the calorimeter. y_{top} and y_{bot} are parameters of the fit whose initial values are given by the geometric projection of the beamlet group centers on the calorimeter. In figure 3.5 a scheme of the fitting parameters is shown.
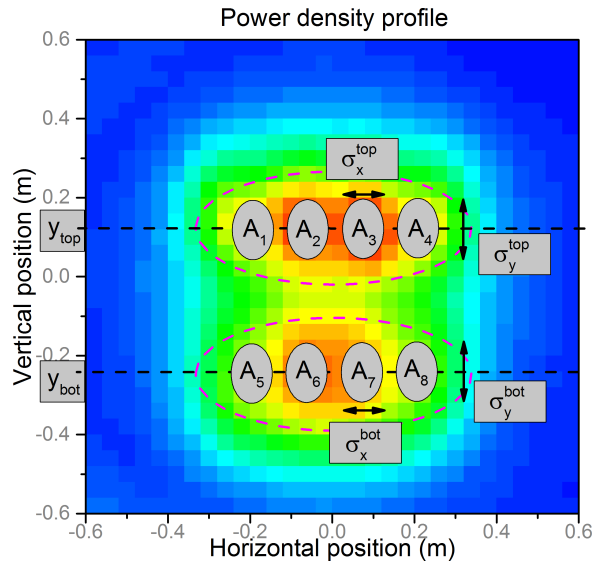

Figure 3.5: Scheme of the bi-dimensional fit performed on the 30×30 power matrix: the parameters of the fit are written on the image, the violet dashed lines indicate the top and bottom beam segments. The eight Gaussian functions describe the eight beamlet groups shown in figure 2.4.

From the fitting parameters it is possible to reconstruct the 2D profile and compare it with the 30×30 measured matrix. Moreover it is possible to retrieve the current density associated with each beam segment and, as a final result, to calculate the normalized perveance related to each beam segment. It is important to underline that the beam segment center positions y_{top} and y_{bot} are not given as a distance from the geometric center of the calorimeter but using the coordinates defined in figure 2.10 *(a)*. The position on the calorimeter of the segment centers is reported for the shot #14609.01 in figure 3.6 *(a)*. As demonstrative example for the fit program, in figure 3.6 the original matrix, the fitted matrix and the residuals are shown. The residuals, in this case, have fluctuations in the order of 10% (for example the red and orange points in fig. 3.6 *(d)*are at about 10%). The database for the IR calorimetry is provided with the residual value in terms of power density $[kW/m^2]$

averaged over the 900 blocks. In general shots performed in good caesiation conditions of the source and well fitted by the Gaussian functions have an averaged residual value below $15\,\mathrm{kW/m^2}$. In any case, before considering the fit results realistic, it is advisable to look at the power matrix and, in case of further uncertainty, to the raw data i.e. the frames from the IR camera. Since the power is related to each block, it is possible to find the power density by dividing the power by the surface of one block ($0.038\,\mathrm{m}\times0.038\,\mathrm{m}$).

(a) *Frame from the IR camera.*

(b) *Power matrix.*

(c) *Fitted matrix.*

(d) *Residuals.*
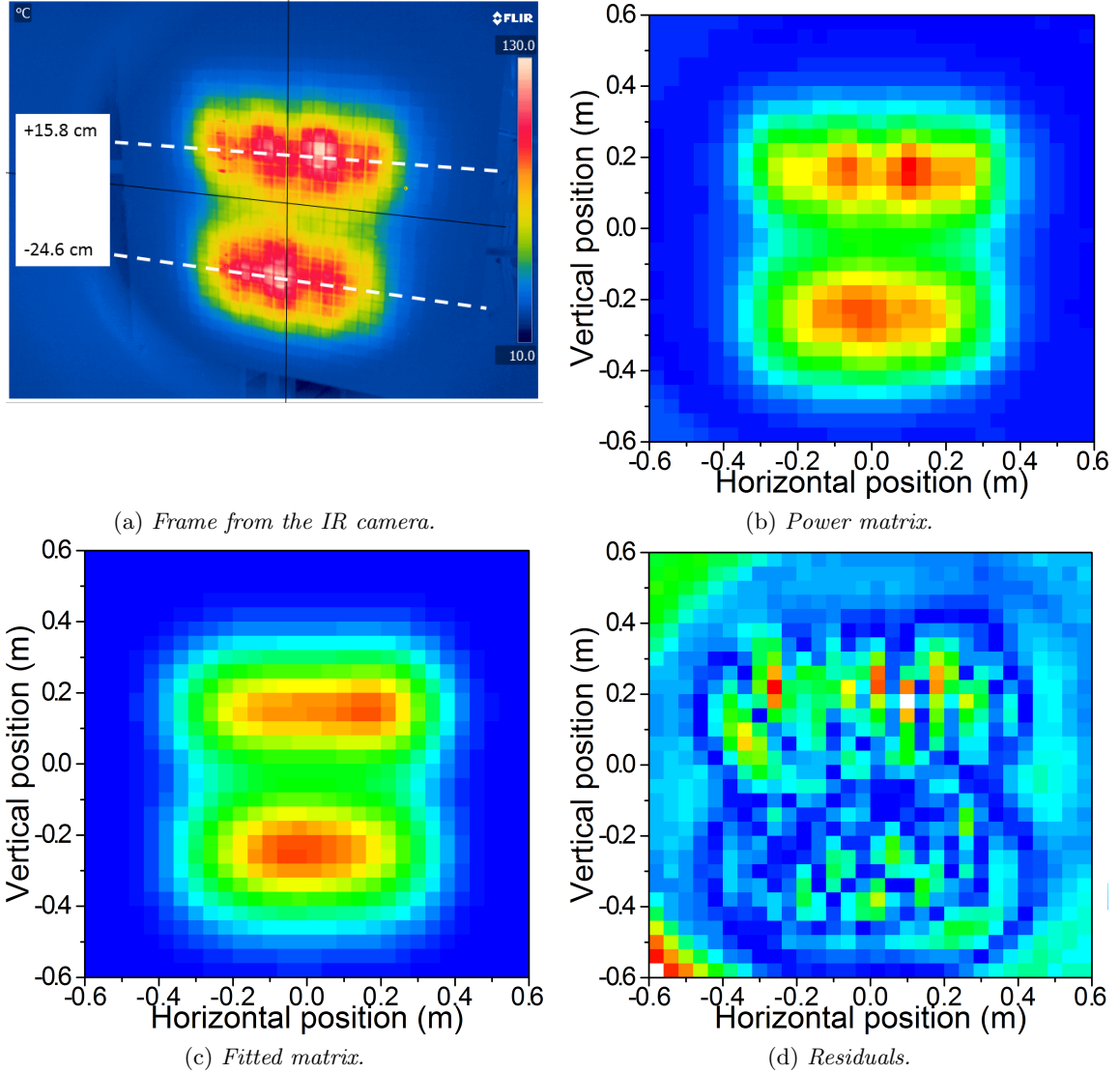
Figure 3.6: Example of the analysis performed on the calorimeter, shot #14609.01 performed on 26/11/2015. Figure *(a)* shows a frame in which the geometric calorimeter center is outlined in solid lines; with dashed lines the beam segment centers are plotted. Figure *(b)* shows the matrix elaborated from the raw data (FLIR data). Figure *(c)* is the fitted matrix calculated from eq. 3.17. Figure *(d)* are the residuals as the absolute values of the difference between the fitted and the original matrix: three of the corners have a higher mean value because the camera view covers also part of the window and these points are not considered in the fitting routine [44]. Figures *(b)* and *(c)* have the same colour scale while for figure *(d)* it was reduced to a 10%: this means that the residuals are about 10%.

The fitting parameters used for the evaluation are reported in tab.3.1, the last column shows the results for the example in fig.3.6.

Parameter	lower constraint	initial value	upper constraint	Fit #14609.01
A1	$5\% \cdot A/8$	$80\% \cdot A/8$	$190\% \cdot A/8$	(0.454 ± 0.008) kW
A2	$5\% \cdot A/8$	$80\% \cdot A/8$	$190\% \cdot A/8$	(0.493 ± 0.009) kW
A3	$5\% \cdot A/8$	$80\% \cdot A/8$	$190\% \cdot A/8$	(0.474 ± 0.010) kW
A4	$5\% \cdot A/8$	$80\% \cdot A/8$	$190\% \cdot A/8$	(0.604 ± 0.008) kW
A5	$5\% \cdot A/8$	$80\% \cdot A/8$	$190\% \cdot A/8$	(0.405 ± 0.009) kW
A6	$5\% \cdot A/8$	$80\% \cdot A/8$	$190\% \cdot A/8$	(0.578 ± 0.010) kW
A7	$5\% \cdot A/8$	$80\% \cdot A/8$	$190\% \cdot A/8$	(0.533 ± 0.011) kW
A8	$5\% \cdot A/8$	$80\% \cdot A/8$	$190\% \cdot A/8$	(0.437 ± 0.009) kW
σ_x^{top}	0.03 m	0.1 m	0.5 m	(0.1 ± 0.001) m
σ_x^{bot}	0.03 m	0.1 m	0.5 m	(0.097 ± 0.002) m
σ_y^{top}	0.03 m	0.15 m	0.5 m	(0.118 ± 0.001) m
σ_y^{bot}	0.03 m	0.15 m	0.5 m	(0.135 ± 0.001) m
y_{top}	0 m	0.205 m	0.32 m	(0.158 ± 0.001) m
y_{bot}	-0.42 m	-0.205 m	-0.08 m	(-0.246 ± 0.001) m

Table 3.1: Fit parameter: initial value and lower/upper constraints; last columns fit results for the shot#14609.01.

where A is the total power calculated from the blocks situated in correspondence to the projection of the beamlet group centers on the calorimeter. The reliability of this fitting formula was tested in [44].

The distance between the centers of two successive blocks is 4 cm and the output errors for the parameters σ_x, σ_y and y are obtained from the minimisation routine of the order of $1-3$ mm. The error calculated by the fit is underestimated: a better value for the error, considering a uniform distribution, can be calculated from the measurement resolution by eq.3.18.

$$\sigma^{\text{upperlimit}} = \frac{4 \text{ cm}}{\sqrt{12}} = 1.15 \text{ cm} \tag{3.18}$$

This value gives an indication on the real error that should be considered for the fit parameters.

In addition to that the quality of the fit depends on the 30×30 power matrix: the larger the width of the beam the more difficult the evaluation of y and therefore the larger the error associated with the parameter. The vertical profile, far from the best beam optics, is characterized by two peaks almost overlapping with a flat top part while for good beam optics the beam segment profile has a peaked shape: in fig.3.7 *(a)* and *(b)* the vertical profile in case of good and bad beam optics respectively is shown (the corresponding 30×30 matrices with the power profile are shown in figure 4.7). In particular for the case in figure 3.7 *(b)* the vertical profile is well described by the fit but the Gaussian that represents the bottom beam is largely affected by the Gaussian function of the top beam segment. In this case the definition of the peak position for the bottom segment has a large uncertainty.
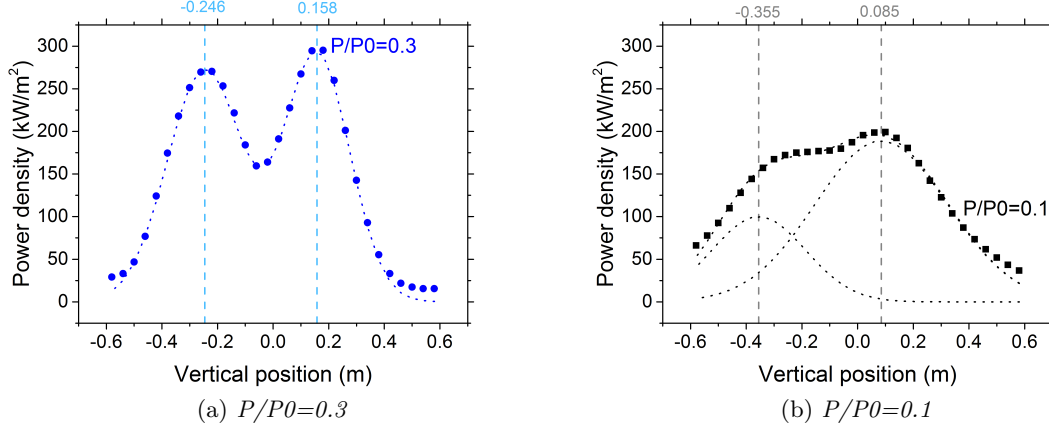
(a) *P/P0=0.3*   (b) *P/P0=0.1*

Figure 3.7: Vertical profiles of shots #14609.01 and#14600.01 left and right respectively. The best beam optics is arount $P/P0 = 0.25$ so *(a)* has a good beam optics, while *(b)* is far from the best beam optics. Each point is the calculated by averaging the power density along the corresponding horizontal line of blocks, the dotted lines are retrieved in the same way but from the fitted matrix, the additional dotted curves in figure *(b)* are the values retrieved averaging only the top and bottom beam segments from the fitted matrix.

Another problem related to the fit is the definition of the horizontal width: in fig.3.6 an example of overestimated σ_x is shown. The beamlet groups on the top segment are distinguishable but in the profile resulting from the fitting procedure they are completely superimposed, even the borders are not defined. The amplitude of the Gaussian functions retrieved by the fit represents the intensity related to the beamlet group. The 8 amplitudes are parameters of the fit and the resulting values, e.g. the one in table 3.1, show that for the beamlet placed in the center (A_2 and A_3 for the top beam segment and A_6 and A_7 for the bottom beam segment) the amplitude is larger than for the beamlet placed laterally (A_1 and A_4 for the top beam segment and A_5 and A_8 for the bottom beam segment). This effect is only apparent and it is due to the overlap in the central part between the beamlet group and the tails of the power distribution coming from the adjacent beamlet groups. So the fit might not describe properly the beamlets groups and their amplitude: as a consequence the horizontal width has a higher error than the value resulting from the fitting procedure, as already mentioned.

35
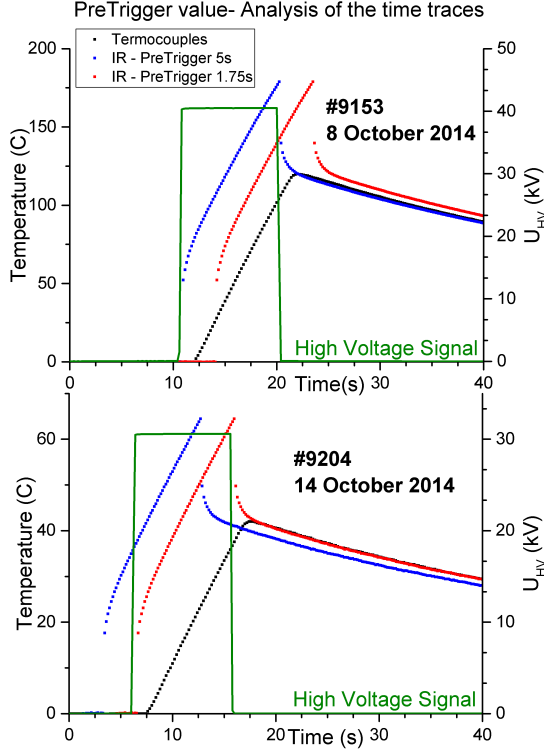
Figure 3.8: Pretrigger change in October 2014

The pre-trigger value used in eq.3.13 was changed in autumn 2014 and during the analysis it was found from which date the new value is set. The value can be modified by a knob in the triggering system and the modification was not written in the log book: at that time the IR camera was used only for a qualitative check of the beam. The analysis developed in this thesis aims to use the calorimeter in a quantitative way and thus the pre-trigger value has a basic importance for the definition of the second frame.

In fig.3.8 three signals from two consecutive dates are plotted as function of the time: the U_{HV} signal, the temperature difference for one block from the thermocouple and the corresponding temperature retrieved by the IR analysis. The pre-trigger value adds a temporal shift on the signal from the IR analysis and, since the temperature of the thermocouple and from the IR analysis should be the same, the correct value is the one for which the two signals overlap.

The correct value changes in two consecutive operating days therefore on October 14, 2014 the numerical value of the pre-trigger was changed from 5 s to 1.75 s.
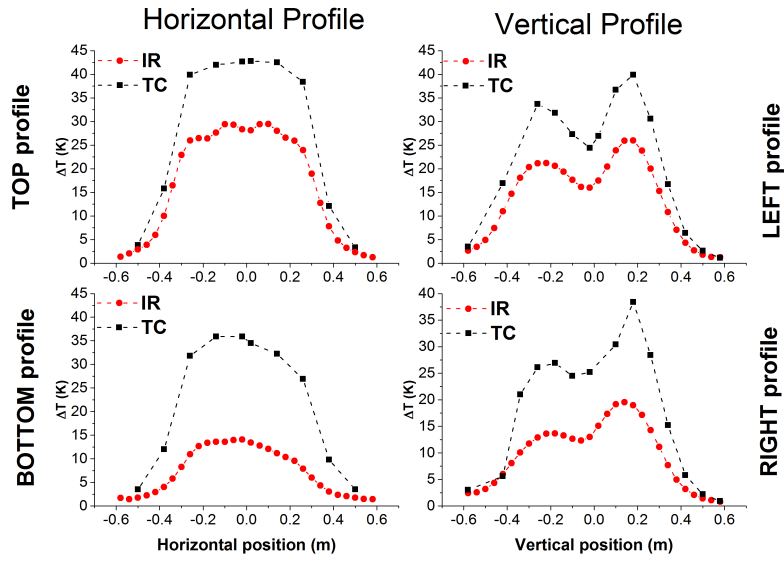
3.2.1 Emissivity calibration and analysis

Based on [44], $\epsilon = 0.83$ was chosen for the emissivity value. At the end of the analysis, from a benchmarking against other diagnostics, a discrepancy was found between the power calculated from the IR camera and the correct value: in fig.3.9 the comparison between the thermocouples (red points) and the temperature of the blocks in which the thermocouples are placed (black points) is shown.

After a general check of the program it was found that the emissivity value was changed. Two hypotheses can be inferred about this difference: first that the emissivity value has changed due to the re-coating of the calorimeter surface happened between February and August 2015 and second that the emissivity value has a gradual decrease due to deterioration of the windows transmittance. The first hypothesis was excluded because before and after the re-coating of the calorimeter the emissivity value was comparable so an analysis of the emissivity value was performed for every shot present in the database. The results are plotted in fig.3.10 as function of the shot number and of the date.

Figure 3.9: Comparison between thermocouple signals (back) and IR temperature (red) calculated with $\epsilon = 0.83$, position of thermocouples shown in fig.2.10
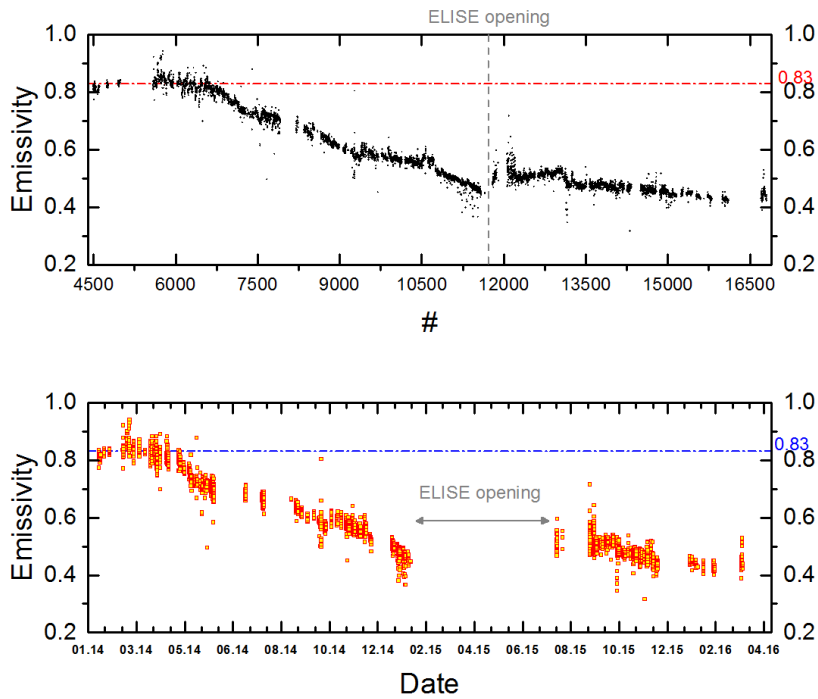

Figure 3.10: Epsilon variation in shot number (top) and date (bottom), $\epsilon = 0.83$ used for first analysis is reported in dashed line.

To compute the correct value for the emissivity an iterative procedure was adopted: since the formula 3.7 is not invertible, the temperature was calculated by increasing the emissivity value from 0.2 to 1 with a step of 0.01 and the temperature which value was closer to the one for the thermocouples gives the correct value for ϵ.

year	month	emissivity
	1	0.82
	2	0.85
	3	0.83
	4	0.80
	5	0.76
2014	6	0.71
	7	0.69
	8	0.66
	9	0.63
	10	0.58
	11	0.58
	12	0.55
2015	1-12	0.49
2016	1-3	0.44

Table 3.2: Emissivity value chosen for each period: the value is an average of all the value found for each shot.

The emissivity value can be different for each thermocouple because a dependence on the temperature can be present. Nevertheless this analysis was performed only on four thermocouples. These thermocouples are positioned at block coordinates (9,11), (22,11), (9,20) and (22,20) (see fig.2.10(a)) in the central region of the calorimeter, where the power deposition is higher. The final value for the emissivity is an average amongst all four values.

Since for the analysis of the profile the emissivity must be set in advance, inside the program an averaged value of emissivity for different intervals of time is included. The emissivity values chosen for each period are reported in tab.3.2: in 2014 the decrease was significant so that the decision was to include a different value for each month; in 2015, due to the ELISE opening, and in 2016 there were only a few days of operations and a single value was adopted.

The new data are evaluated with an emissivity value $\epsilon = 0.44$: the analysis of the emissivity can be updated only *ex post facto*. Some of the video collected by the camera were not properly focused: this means that the light collected in a pixel does not belong only to the surface covered by that pixel but also to nearby regions (the so-called *cross-talk* effect). In order to investigate the effect on the evaluation and the emissivity value, a series of shots were taken with the same experimental set-up but different focusing condition: the focus is counted in number of click from the 0, where 0 indicates the best focus. Three images are reported in fig.3.11, the de-focusing effect in one direction or in the other is not distinguishable at a first glance.
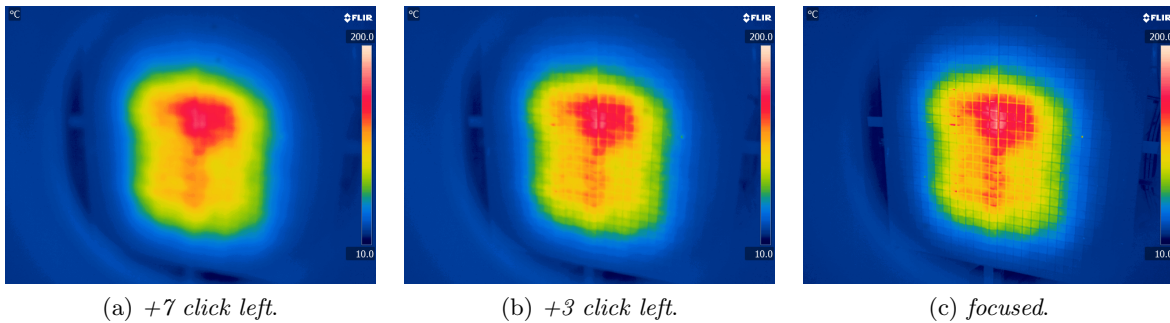

(a) *+7 click left.*   (b) *+3 click left.*   (c) *focused.*

Figure 3.11: Effect of the focus on the image: from left to right shots #18103.01, #18101.01 and #18098.01

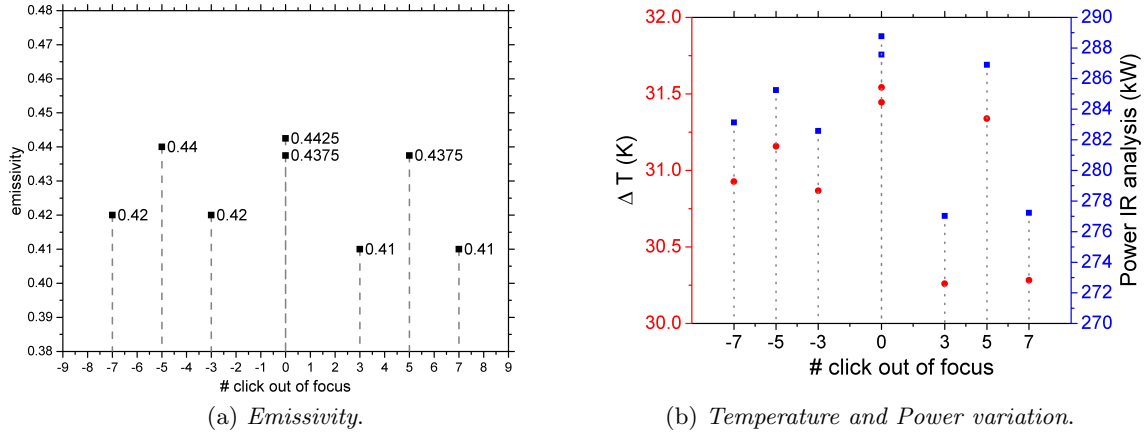(a) *Emissivity.* (b) *Temperature and Power variation.*

Figure 3.12: Effect of the focus on the emissivity (left) and on the temperature variation and power deposited (right).

The defocused images give an emissivity value decreased about 10% (see figure 3.12 *(a)*). The same variation occurs on the temperature and the power density (see figure 3.12 *(b)*). This analysis is limited because the thermocouples analysed are in the central position and the colours in this region are not significantly affected by the focus. The higher variation is expected for the blocks on the edges of the calorimeter.

3.3 Comparison with other diagnostics

In the following sections the initial cross-checks against other diagnostic systems are reported: these comparisons can verify the reliability and validity of the analysis. In particular in 3.3.2 global properties are analysed, such as the total power deposited by the beam on the plates and on the total calorimeter in connection with the water calorimeter and to the ion current. The beam profile is analysed in comparison with the BES diagnostic in sec.3.3.1.

3.3.1 Beam profile

As explained in sec.2.2.3, from the analysis of the BES it is possible to retrieve information about the local characteristics of the beam. One of the first check was the comparison of the profile given by the BES and by IR analysis. As the signals from the BES are integrals along one line-of-sight, in order to make the two profile comparable, the 30×30 matrix was reduced to a vertical or horizontal sequence by averaging along rows or columns respectively. The IR analysis demonstrates the capability to distinguish the profile changes among shots inside the same experimental campaign. In figure 3.13 the signals and the profile from the two diagnostic systems are shown: it is noticeable that the colour ordering is preserved between BES an IR thermography; moreover the profile appears similar to the same ratio of the peaks and comparable width, while the position of the peaks is preserved as well.
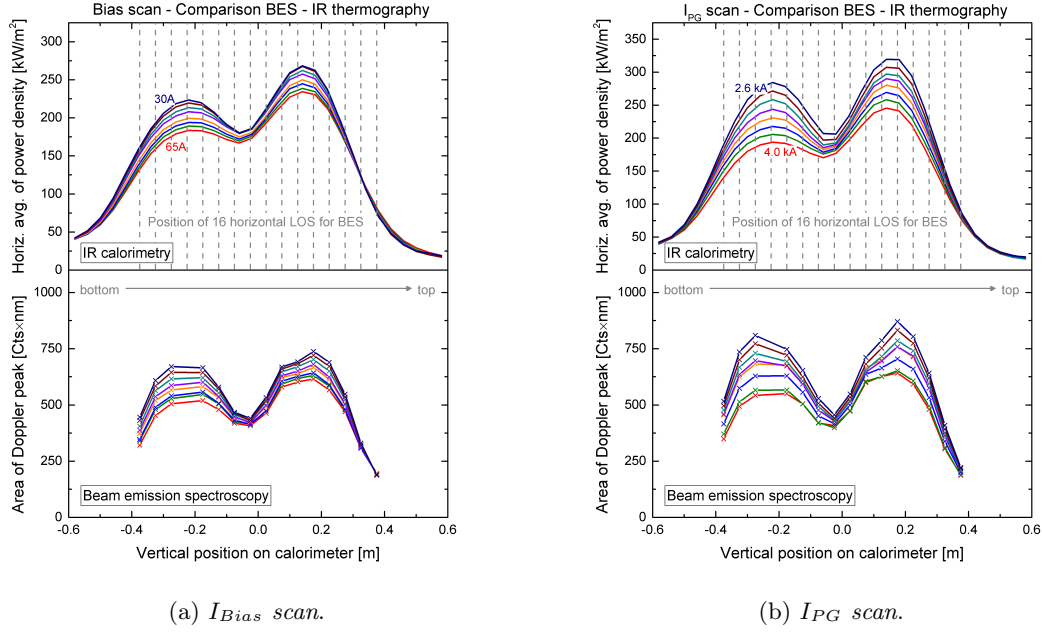
(a) I_{Bias} scan.
(b) I_{PG} scan.

Figure 3.13: Beam profile from the IR analysis compared to BES analysis

3.3.2 Benchmarking against other diagnostics

The water calorimetry performed on the diagnostic calorimeter allows measuring for every shot, the total heat absorbed by the calorimeter: the heat deposited on the block surfaces is transmitted to the back side and removed by the water cooling system. The data reported in the database have the unit of current density (A/cm^2) and therefore for the total power deposited on the calorimeter it is necessary to use eq.3.19.

$$P_{WC} = (j_{WC} * S) * U_{HV} = I_{WC} * U_{HV} \qquad (3.19)$$

where S is the total surface of the apertures in the grid system and U_{HV} is the high voltage potential. The total power is deposited on the total surface of the calorimeter (1.2 m × 1.2 m). To compare this quantity to the power measured by the IR analysis it in necessary to scale the power from the total calorimeter by a factor R that takes into account the ratio between the surfaces of the two diagnostics (eq.3.20).

$$R = \frac{900 \times 0.038\text{m} \times 0.038\text{m}}{1.2\text{m} \times 1.2\text{m}} \qquad (3.20)$$

The result of the comparison is shown in fig.3.14(a) and the two diagnostics are in good agreement.

The electrically measured ion current, multiplied by the total high voltage U_{HV}, gives another measure for the beam power: also in this case a linear relationship is expected even if not a 1-1 relation because it is not possible to evaluate the real area of the impinging ions. Nevertheless the two diagnostics are in good agreement taking in account that the edges of the beam are not measured by the calorimeter and therefore part of the information is lost. The results are shown in fig.3.14(b).
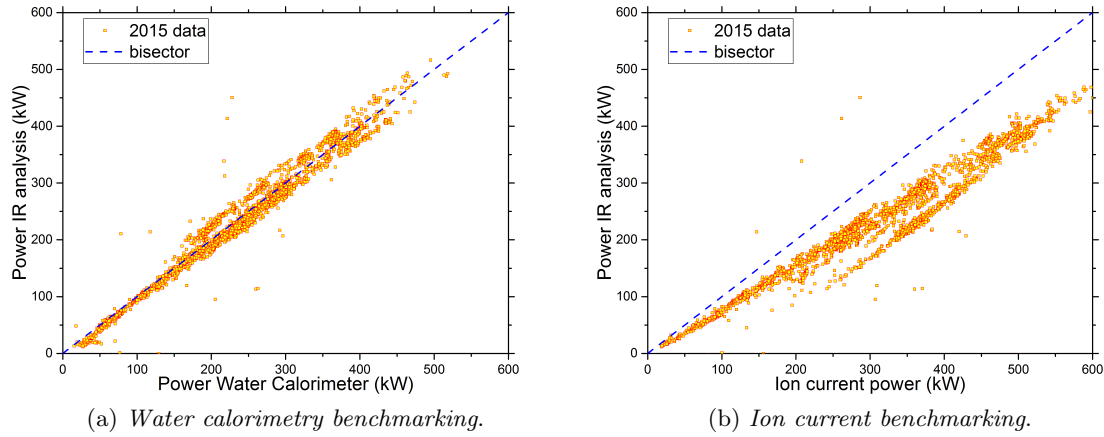
(a) *Water calorimetry benchmarking.*   (b) *Ion current benchmarking.*

Figure 3.14: Benchmarking of the total power against the water calorimeter and the ion current electrically measured

In figure 3.14*(b)* two populations are identifiable due to the different trends with respect to the ion current power. The different slope is due to the stepwise change of the emissivity value embedded inside the program: in a period in which the emissivity is supposed constant, the power evaluation does not follow the real power and this results in a different slope.

The water calorimeter measures the power deposited on each plate of calorimeter separately: the power distribution on the plates gives a quantitative information on the distribution of the beam on the calorimeter. The power distribution on the plates calculated by the IR analysis is in agreement with the water calorimetry.

(a) *IR analysis.*   (b) *Water calorimetry.*
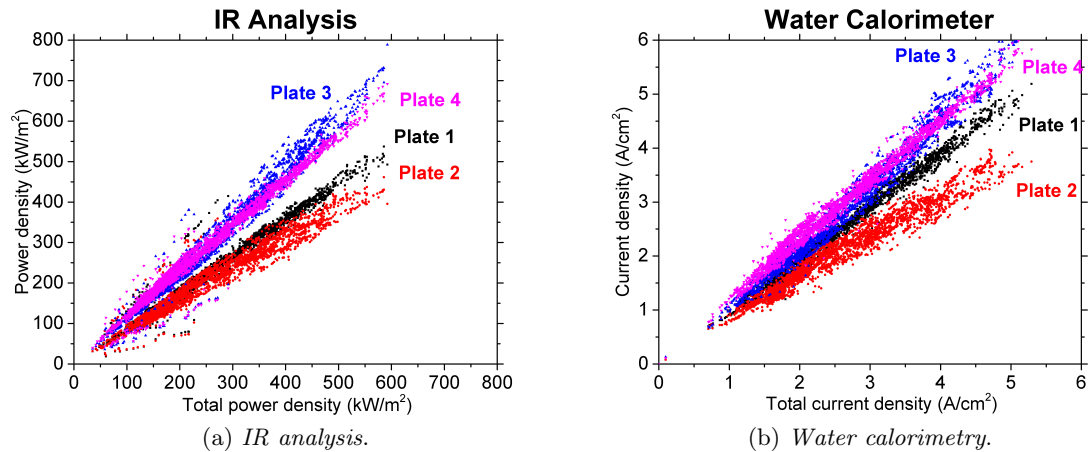
Figure 3.15: Benchmarking of the power density from the four plates between the water calorimeter and the IR thermography for the year 2014

(a) *IR analysis.*

(b) *Water calorimetry.*
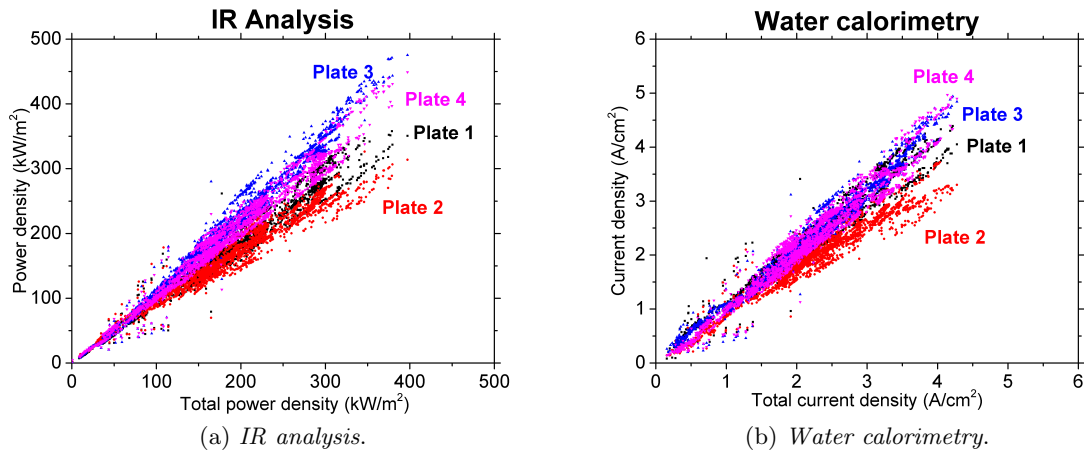
Figure 3.16: Benchmarking of the power density from the four plates between the water calorimeter and the IR thermography for the year 2015

The distribution of the beam on the four plates is reproduced by the IR analysis: in figures 3.15 and 3.16 all the analysed shots for the year 2014 and 2015 are shown. In 2014 the power deposited on the calorimeter was higher than in 2015 and it results in a wider range of the axes. Moreover in 2014 the plates placed in the bottom part (plates #3 and #4) have endured a greater thermal deposition rather than the top plates (#1 and #2) while in 2015 the heat deposition is more homogeneous on the plates. Similar figures to 3.14, 3.15 and 3.16 were shown also in [44]; the present ones are the results from the automatic evaluation which is the preliminary work of this thesis.

Chapter 4

Beam Analysis

The main hypothesis of the fit described in section 3.2 is the possibility to divide the beam in two independent *beam segments*: the bottom and the top part of the beam. Inside the beam segments the eight beamlet groups are grouped (4 beamlet groups per beam segment). The fit is two-dimensional and for each of the beamlet groups inside the beam segment the same vertical and horizontal width is assumed. In the following the beam segment center is the vertical position on the calorimeter of the peak obtained from the fit. The coordinates used in the following graphs are shown in fig.2.10. In paragraphs 4.1, 4.2 and 4.3 the effect of parameter variation on the beam properties is mainly discussed, while in 4.5 and 4.6 the effects of the drifts that take place inside the source volume are analysed also in correspondence to changes of the magnetic configuration in the expansion region. As a general introduction for the chapter *summary graphs* are shown: in these graphs all the analysed shots are collected unsorted and only general dependences are shown. With the help of these general plots, correlations and dependences are highlighted.

In figure 4.1 the dependence of the center of the beam segments on the normalized perveance is highlighted; in section 4.1 this relation is investigated with dedicated perveance scans.
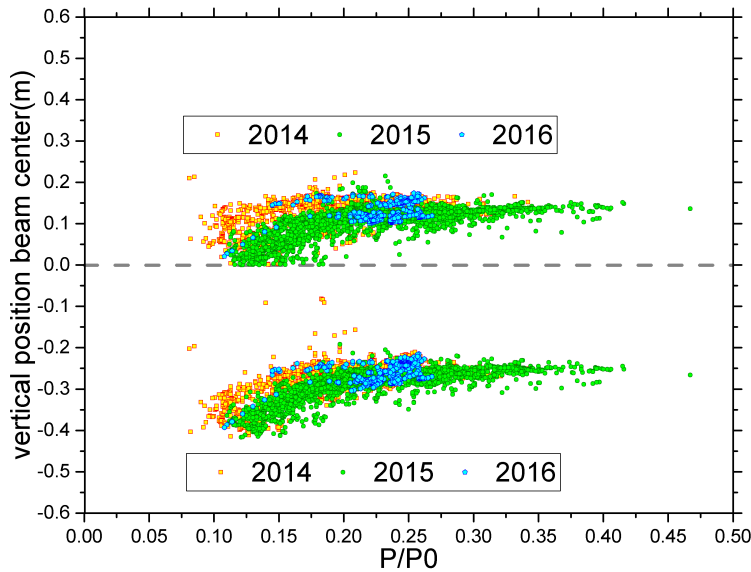

Figure 4.1: centers of the top and bottom beam segments in function of the normalized perveance P/P_0. The vertical scale covers the entire vertical size of the calorimeter: this outlook is useful to compare the vertical displacement of the beam with the real size of the calorimeter.

Other well-known dependences such as the correlation between beam width and perveance are shown in figures 4.3 and 4.4 for data collected in 2014 and 2015 respectively. The beam width is proportional to the divergence of the beam measured by the BES: the trend shown in figures 4.3 and 4.4 is equivalent to the one for the beam divergence shown in 4.2.
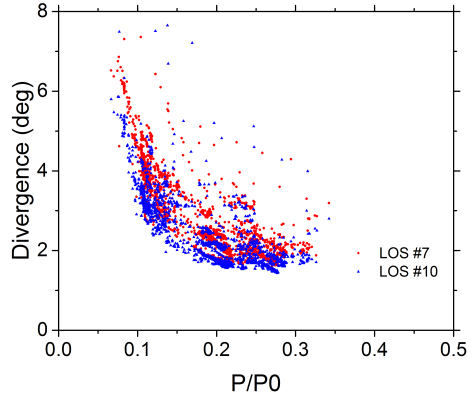

Figure 4.2: Results of the divergence measured by on line-of-sight of the BES. The minimum is between $P/P0 = 0.2$ and $P/P0 = 0.25$. Data plotted belongs to shots in 2015 with hydrogen.

The beam width is expected to exhibit a minimum in correspondence with the best perveance value. Along the vertical direction σ_y shows for the top segment a minimum between $P/P0 = 0.25$ and $P/P0 = 0.3$ for both 2014 and 2015. In horizontal direction, σ_x does not reach the minimum, which seems to lie at perveance values larger than $P/P0 = 0.4$ considering data in 2014. Regarding σ_y, the bottom beam segments not as well defined as the top segment.

The beam segment at the bottom is not defined as well as the top segment: this problem can be connected to the relatively not well defined 2D imprint of the bottom beam segment on the calorimeter, which in general has a lower intensity, and the resulting difficulty in the definition of parameters.
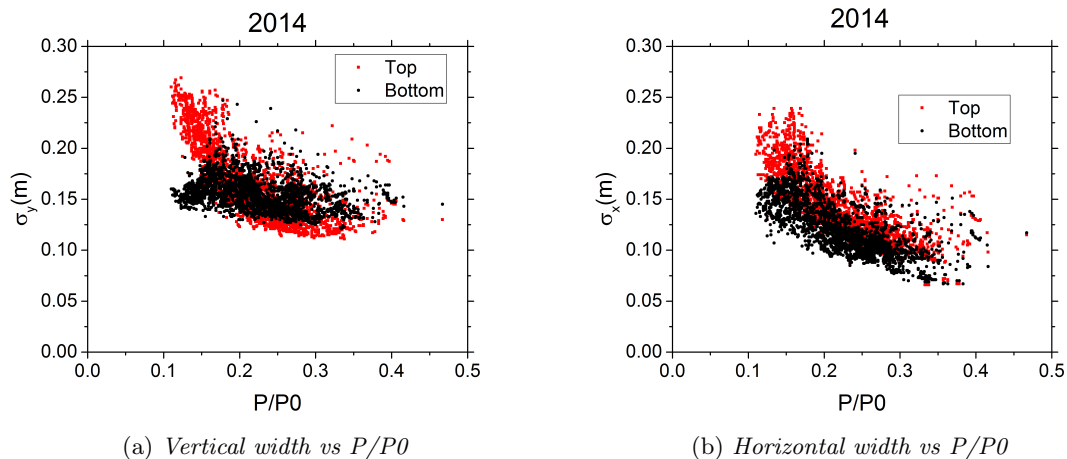

(a) *Vertical width vs P/P0*

(b) *Horizontal width vs P/P0*

Figure 4.3: Vertical width (left) and horizontal width (right) vs normalized perveance P/P_0 analysis on 2014 shots

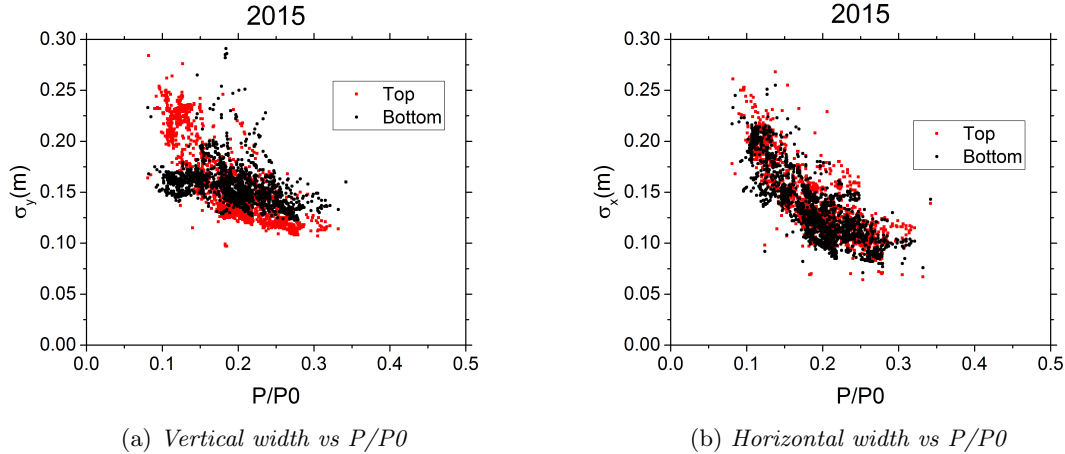(a) *Vertical width vs P/P0* (b) *Horizontal width vs P/P0*

Figure 4.4: Vertical width (left) and horizontal width (right) vs normalized perveance P/P_0 analysis on 2015 shots

These plots show the beam optics behaviour with respect to the normalized perveance: as explained in section.1.3.2 the extraction and acceleration stages act like a lens system focusing or de-focusing the beam. Among the output parameters from the fitting process, the two that describe the vertical and horizontal width of the beam are σ_y and σ_x respectively, which represent in each direction the half width at 60% of the height of the fitting Gauss curve.

The distance between the centers of two beamlet groups, along the vertical and horizontal direction, is 39.6 cm and 16 cm respectively (see figure 2.3*(b)*) so a possible criterion to define a beamlet group as distinguishable from the other is to say that σ should be lower than half the distance between the centers of two successive beamlet groups in the grid. The results are written in eq.4.1.

$$\begin{cases} \sigma_y \leq \frac{39.6\,\text{cm}}{2} \\ \sigma_x \leq \frac{16\,\text{cm}}{2} \end{cases} \tag{4.1}$$

In this way $\sigma_x < 8$ cm and $\sigma_y < 19.8$ cm.

This criterion seems to be too strict taking into account the graphs in fig.4.3 *(a)* and fig.4.4 *(a)* because one third of the points are higher than the limit for σ_y. The case of σ_x is particular because almost all the points are above the limit. For $\sigma_y = 25$ cm the half width of $\frac{39.6\,\text{cm}}{2}$ is reached at 73% of the height while, for $\sigma_x = 25$ cm, the half width of $\frac{16\,\text{cm}}{2}$ is reached at 95% of the height. The conclusions are that for the vertical width the fit works properly but with larger uncertainty for σ_y larger than 20 cm while for σ_x the beamlet group are mostly indistinguishable; however the fit takes advantage of the constraint due to the profile at the edges of the beam to improve the reliability of the results.

4.1 Perveance scan

For the ELISE grid system the optimum perveance is around 0.2 - 0.23 measured by the BES diagnostic[33]: in the following paragraphs the terms *under-perveant* and *over-perveant* will be referred to scans performed with a normalized perveance respectively lower and higher than the optimum perveance. The perveance can be changed by the variation of both the extracted current and the extraction voltage. The relationship between perveance and ion current is shown in figure 4.5*(a)*: shots in the database are selected choosing the same parameters such as bias current, extraction voltage, acceleration voltage, ion type and filling pressure. The ion current increases linearly with $P/P0$.

As explained in sec.1.3.2, the current increases when the RF power is increased: the plot in fig.4.5(b) shows a linearity in the operative range. Actually the ion current saturates and reaches a plateaux after a certain value of RF power therefore power scans are performed in the linear region.
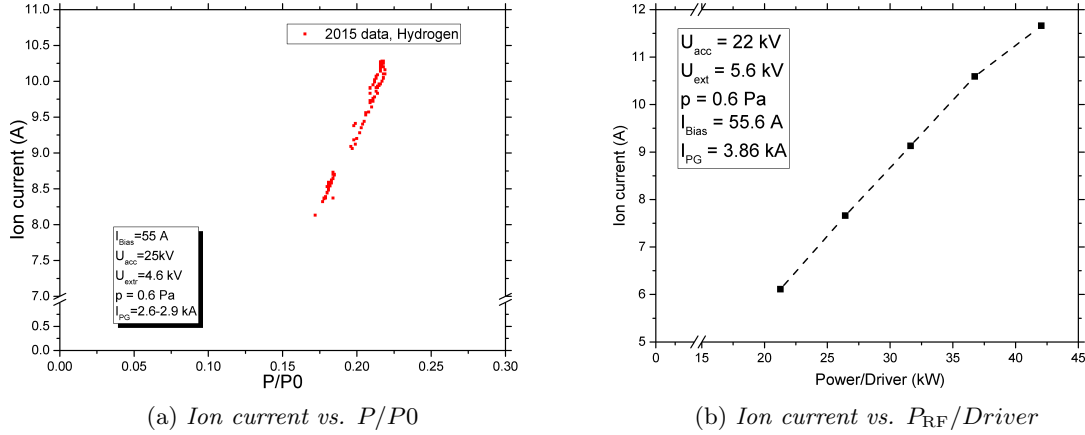

(a) *Ion current vs. $P/P0$* (b) *Ion current vs. $P_{RF}/Driver$*

Figure 4.5: Linear dependence of the perveance on the ion current

In general a *scan* is a sequence of beam blips in which usually only one parameter is changed. In order to perform a reproducible scan the source must be well caesiated: this means a stable value of extracted current density and electron to ion ratio less than 1 in hydrogen and less than $1.5 - 2$ in deuterium. Scans are used to investigate the plasma behaviour under different conditions and changing parameters in a controlled way.

4.1.1 Extraction voltage scan

In the following perveance scan the extraction voltage U_{ex} was changed and the same extracted current was kept: the perveance scan was repeated for two different values of extracted current density. The width of the beams decreases for increasing $P/P0$, which means decreasing U_{ex} (see eq.2.1), till it reaches a minimum. For the horizontal width the optimum beam optics is in correspondence to the minimum of the two curves around $P/P0 = 0.2 - 0.25$. However for the vertical width the trends are not similar: the two curves seem to not have the same minimum and the bottom beam segment does not reach a minimum at all. The two trends are shown in fig.4.6.

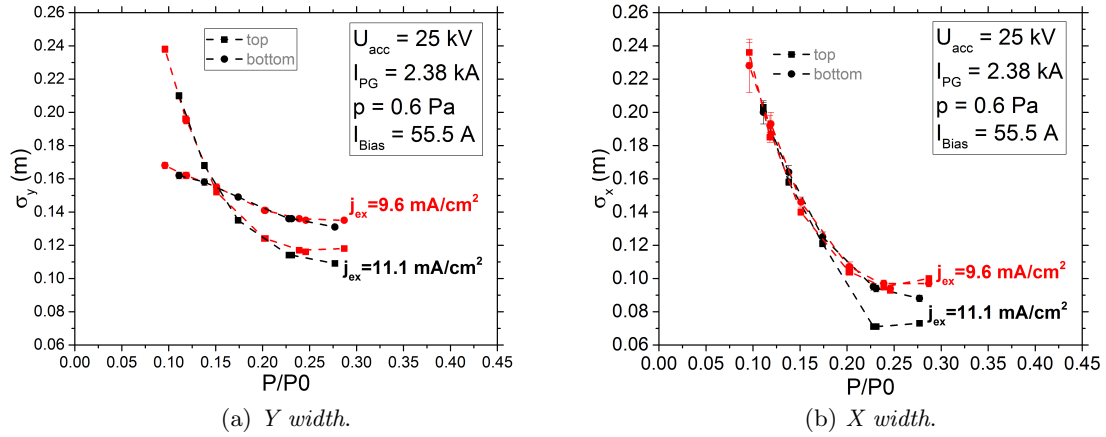(a) *Y width.*   (b) *X width.*

Figure 4.6: Vertical (left) and horizontal (right) width retrieved from the fit procedure. According to this scan the best beam optics along the horizontal direction is at $P/P0 = 0.2 - 0.25$ while along the vertical direction seems to be at about $P/P0 = 0.25 - 0.3$.

Figure 4.7 shows the physical meaning of the perveance: in *(a)* the divergence of the beam is such that the imprint covers most of surface of the calorimeter while, in *(b)*, the profile is more defined and the beamlet groups are distinguishable because of the low divergence.

(a) $P/P0 = 0.1$ (b) $P/P0 = 0.3$
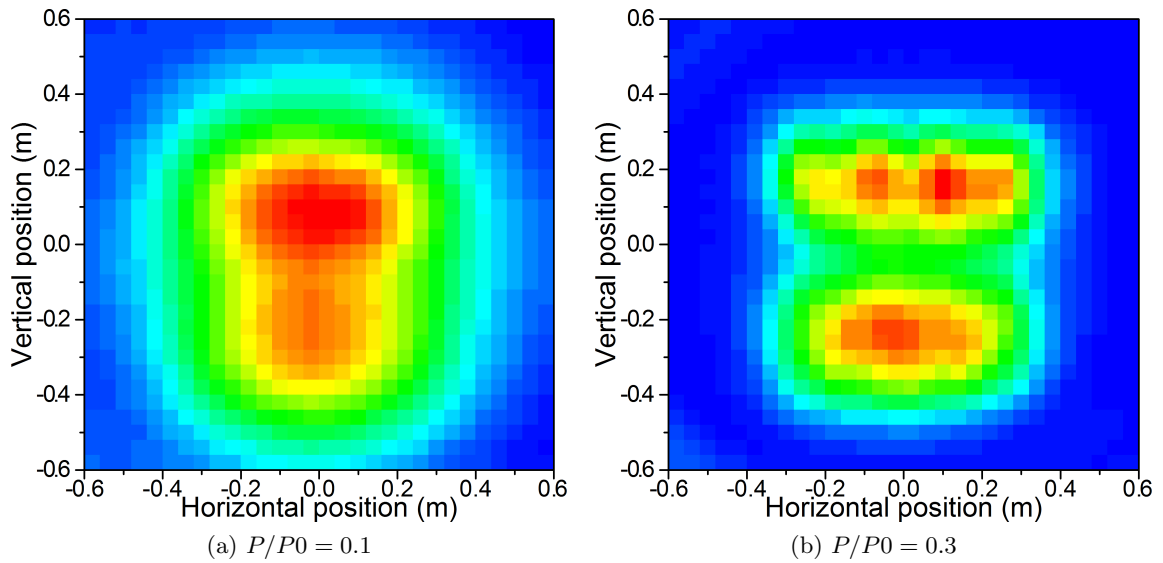
Figure 4.7: 2D profile of the power on the calorimeter for shots #14600.01 and #14609.01. In these two figures the effect of the perveance on the beam imprint is visible: on the right the beamlet groups are distinguishable and the perveance is close to the best perveance while for the figure on the left the beamlet groups form two spots on the calorimeter and the perveance value is far from the best perveance value.

While the beam optics is connected to the quality of the beam in a quite intuitive way (see fig.1.13), the connection between the perveance and the displacement of the beam is not so obvious. In fig.4.8 this relationship is shown.
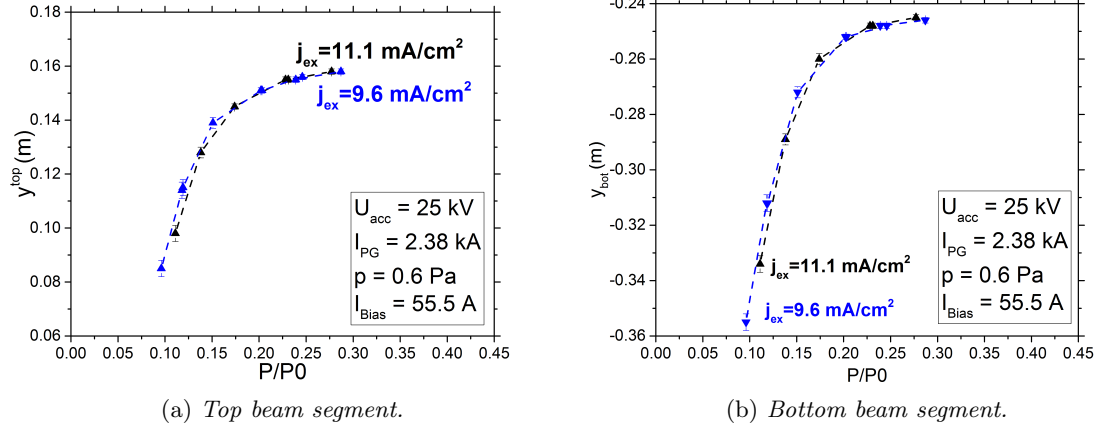
(a) *Top beam segment.* (b) *Bottom beam segment.*

Figure 4.8: Position of the beam segments on the calorimeter along the vertical direction. Data from a perveance scan (extraction scan) considering two different values of extracted current.

The total displacement of the two beam segments, that move slightly in parallel, is considerable: the value is 12 cm for the bottom and 8 cm for the top segment. The extraction voltage affects the velocity of the particle and, due to the Lorentz force, the higher the particle velocity the less the trajectory is bent. As the particle velocity is proportional to the extraction potential and the perveance is inversely proportional to the extraction potential ($P \propto U_{\mathrm{ex}}^{-3/2}$), one can expect a increase of the beam displacement by increasing the perveance. The Larmor radius (eq.1.20) increases proportionally with the velocity and, in a long distance, the impinging point onto a target moves accordingly: figure 4.9 shows the case of negative ions in a uniform magnetic field, the field vectors point accordingly to the configuration of ELISE.
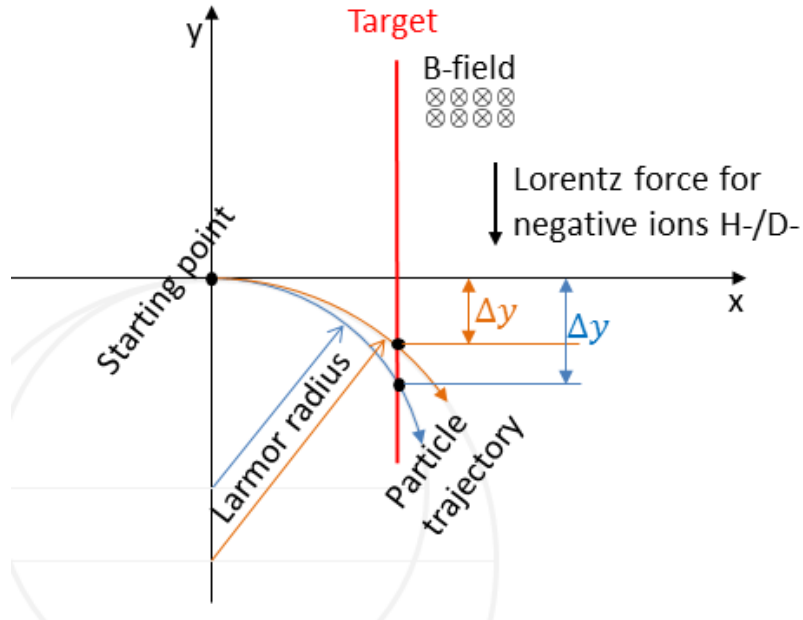

Figure 4.9: Scheme of the position on a target of a particle affected by the Lorentz force, the velocity and magnetic fields are chosen in agreement with the configuration in ELISE but considering a uniform magnetic field.

As the particle velocity increases, the deflection on the target decreases. The beam

imprint on the calorimeter, keeping the same magnetic field, should move upwards in the calorimeter. The effect seen in fig.4.8 is opposite: the beam is usually positioned at 0.16 m and -0.24 m for the top and bottom segment respectively and moves upwards as the energy increases: this assumption comes from the measured position of the beam segments on the calorimeter in case of deuterium that has a higher mass and so it is less affected by drifts.

The influence is not so strong because in 3.5 m the displacement is 12 cm and thus the deflection is $\arctan(0.1/3.5) = 1.6°$ for the analysed scan. The deflection is visible and the power profiles corresponding to the cases $P/P0 = 0.1$ and $P/P0 = 0.3$ are shown in fig.4.7 (a) and (b) respectively.

In order to understand the final deflection of the beam in relation to the perveance a finite element analysis was performed. A line, perpendicular to the grids and connecting the grounded grid to the calorimeter, is divided into small interval of dimension Δx each one labelled with the index i. The simulation aims to find the final position on a target of a particle moving in a magnetic field starting from a vertical position of 0 0. The initial velocity, parallel to the beam-line is given by eq.4.2.

$$v_\parallel^0 = \sqrt{\left(\frac{2qU_{\text{ex}}}{m}\right)} + \sqrt{\left(\frac{2qU_{\text{acc}}}{m}\right)} \tag{4.2}$$

where m is the particle mass, q its charge, U_{ex} the extraction voltage and U_{acc} the acceleration voltage. The velocity parallel to the magnetic field is given iteratively by eq.4.3

$$v_\perp^i = v_\perp^{i-1} + a_\perp^i \cdot \Delta t^{i-1} \tag{4.3}$$

where Δt^i is given by eq.4.4 and $a_\parallel^i$ from eq.4.5.

$$\Delta t^i = \frac{\Delta x}{v_\parallel^i} \tag{4.4}$$

where $\Delta x = 1.9$ cm.

$$a_\perp^i = \frac{q v_\parallel^{i-1} B^i}{m} \tag{4.5}$$

For each point the perpendicular velocity $v_\parallel^i$ is calculated by using the conservation of energy (eq:4.6)

$$v_\parallel^{i+1} = \sqrt{(v_\perp^i)^2 + (v_\parallel^i)^2 - (v_\perp^{i+1})^2} \tag{4.6}$$

The simulation is done for $U_{\text{acc}} = 25$ kV and the realistic magnetic field whose trend as a function of the position along the beam line is shown in figure 2.6 $U_{\text{ex}} = 2 \div 12$ kV. A summary diagram is shown in figure 4.10.

x	B	$v_\parallel$	dt	$a_\perp$	$v_\perp$	y
PG (0 cm)	0	$= \sqrt{\frac{2\,q\,U_{acc}}{m}} + \sqrt{\frac{2\,q\,U_{ex}}{m}}$	$= \frac{\Delta x}{v_\parallel^i}$	0	0	0
0,2 cm	B^i	$= \sqrt{(v_\parallel^{i-1})^2 + (v_\perp^{i-1})^2 - (v_\perp^i)^2}$	$= \frac{\Delta x}{v_\parallel^i}$	$= \frac{q\,v_\parallel^{i-1} B^i}{m}$	$= v_\perp^{i-1} + a_\perp^i * dt^{i-1}$	$= y^{i-1} + v_\perp^i * dt^{i-1}$
0,4 cm	B^i	$= \sqrt{(v_\parallel^{i-1})^2 + (v_\perp^{i-1})^2 - (v_\perp^i)^2}$	$= \frac{\Delta x}{v_\parallel^i}$	$= \frac{q\,v_\parallel^{i-1} B^i}{m}$	$= v_\perp^{i-1} + a_\perp^i * dt^{i-1}$	$= y^{i-1} + v_\perp^i * dt^{i-1}$
...	B^i	$= \sqrt{(v_\parallel^{i-1})^2 + (v_\perp^{i-1})^2 - (v_\perp^i)^2}$	$= \frac{\Delta x}{v_\parallel^i}$	$= \frac{q\,v_\parallel^{i-1} B^i}{m}$	$= v_\perp^{i-1} + a_\perp^i * dt^{i-1}$	$= y^{i-1} + v_\perp^i * dt^{i-1}$

Figure 4.10: Iterative calculations for the finite element simulation.

The result, as a function of the normalized perveance $P/P0$ is shown in fig.4.11. The position of the beam in the calorimeter from the IR evaluation has a completely different trend with respect to the simulation with one particle.
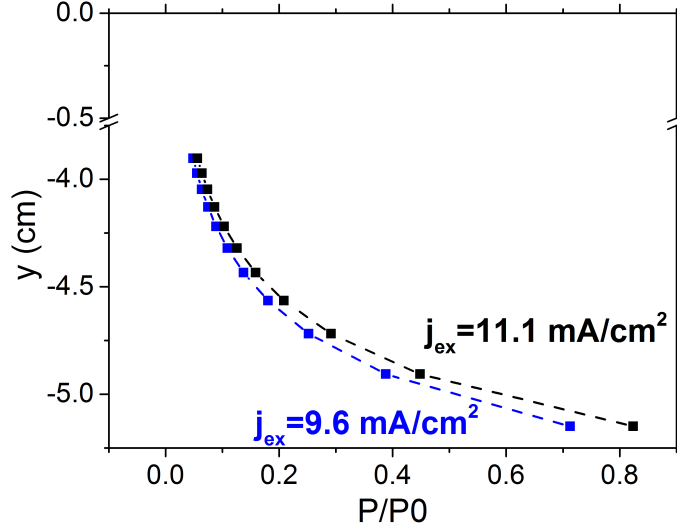

Figure 4.11: Simulation of the final vertical position of a particle starting from $y = 0$ m in function of $P/P0$ considering $j_{ex} = 11.1$ mA/cm^2 in black and $j_{ex} = 9.6$ mA/cm^2 in blue.

The absolute value is not expected to match the experimental data due to side affects such as space charge compensation and collisions with the background gas Apparently the trend of the position with respect to the perveance is not due to the Lorentz force on the beam but to another phenomenon. Since the same trend occurs also in power scan (see section 4.1.2), in which the extracted current is changed with a fixed extraction potential, it is possible that the phenomenon is connected to the beam optics and to the way in which the beamlets are formed from the plasma volume. This phenomenon is still under investigation. A possible explanation is introduced in [45] and it is related to inhomogeneous extraction of particles at the PG.

4.1.2 Power scan

The perveance scan performed by varying the extracted current is a power scan because of the linear relationship between the RF power and the extracted current shown in fig.4.5 *(b)*. Due to the relation with the perveance, the width of the beam segments has a minimum. In the case of the horizontal width, shown in fig.4.12 *(b)*, the minimum is approximately at the same extracted ion current, while for the vertical width the two minima (fig.4.12 *(a)*) are placed in a different position and the bottom part has a very different shape and range of variation. The different shape of the bottom beam segment along the vertical direction could be explained with a different optics related to the beam segment and a consequent variation of the normalized perveance associated to that beam segment. Again the fit seems to have some problems of convergence and, what is recognizable as a minimum, could be only a flat curve without any dependence on the perveance.
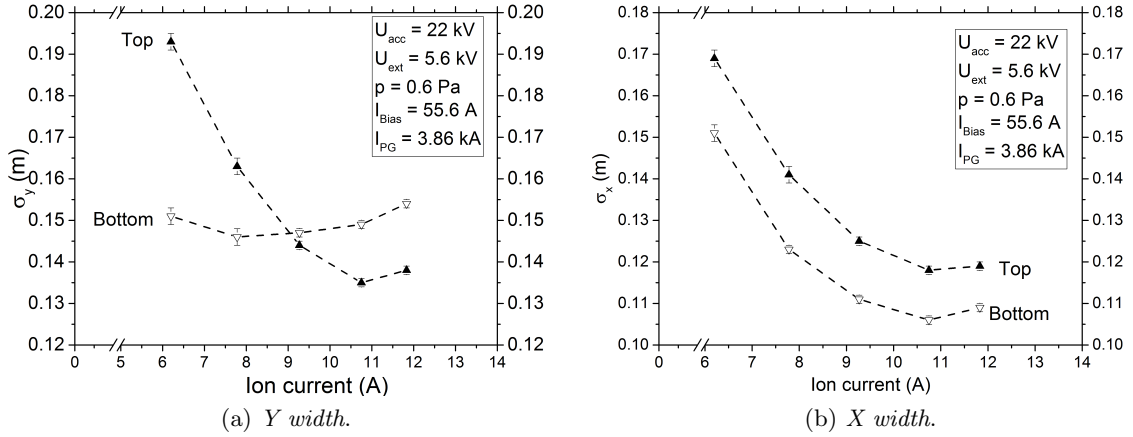
(a) *Y width.*   (b) *X width.*

Figure 4.12: Vertical(left) and horizontal(right) width from the fit, data belong to a power scan but data are plotted in function of the extracted ion current

For what concerns the displacement of the center of the beam segments, shown in figure 4.13 *(a)*, they are shifted by about 6 cm both in vertical and horizontal direction by changing the ion current by 6 A. The plot of the segment positions in function of the normalized perveance $P/P0$ is shown in figure 4.13 *(b)*. The trend has some similarities with the one shown in figure 4.8 because decreasing the perveance the beam is deflected more to the bottom of the calorimeter. This supports the hypothesis of a dependence of the beam displacement on the beam optics.

(a) *Beam segment position vs. Ion current.*   (b) *Beam segment position vs. normalized perveance.*
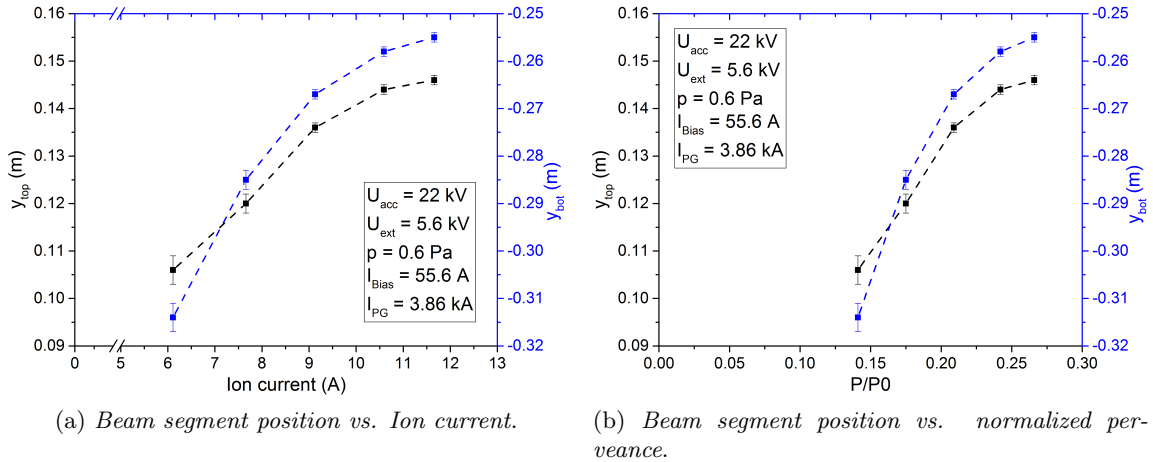
Figure 4.13: Beam segment position on the calorimeter as a function of the extracted ion current (left image) and of the normalized perveance (right image).

4.2 Acceleration scan

The effect of the acceleration stage on the beam optics is comparable to the one of the extraction voltage: figure 4.14 shows the beamlet group trend of the width which is comparable to a perveance scan (see figure 4.6). Actually in the extraction stage, beamlets are extracted from a plasma that appears at the grid system without a preferential direction of the particles, while before the acceleration stage the particles move along a direction (perpendicular to the grids) and are arranged in a beamlet. The horizontal width of the beam, shown in fig.4.14*(b)*, has the typical trend of a perveance scan: the optimum beam optics

corresponds to the minimum of the curves for the top and bottom beams. The vertical width behaves differently for the top and the bottom beam segments: the bottom beam segment in the vertical direction (figure 4.14 *(a)*) is much broader than the top beam segment. They seem to have different beam optics due to different extracted current; moreover the two minima seem not to correspond to the same value of potential.
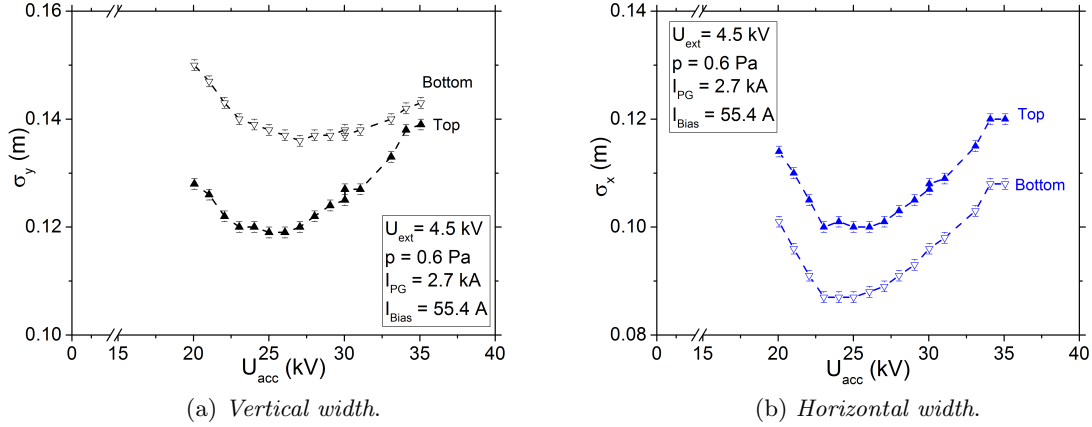

(a) *Vertical width.*

(b) *Horizontal width.*

Figure 4.14: Vertical (left) and horizontal (right) width retrieved from the fitting procedure. The best optics is for a ratio $U_{ex} - U_{acc}$ of $4.5\,kV - 25\,kV$.

Concerning the beam segment centers it is noticeable that the two segments react differently with increasing voltage: the shift of the bottom segment is larger than the one for the top segment.

In figure 4.15 *(a)* and *(b)* the position of the beam segment top and bottom respectively is plotted against the acceleration voltage U_{acc}. Two acceleration scans are analysed with different RF power P_{RF} per couple of driver: in black the acceleration scan $P_{RF} = 75\,kW$ and in red the one with $P_{RF} = 60\,kW$ per couple of drivers (top and bottom).

For the same value of acceleration voltage, the beam segment position for the scan at $P_{RF} = 75\,kW$ is situated above on the calorimeter than the position in case of $P_{RF} = 60\,kW$ (for both top and bottom beam segments). It is possible to verify that the results from the fit are reproducible: taking into account the error bars, the points at the same acceleration voltage overlap; e.g. the measure at $25\,kV$ is repeated four times.
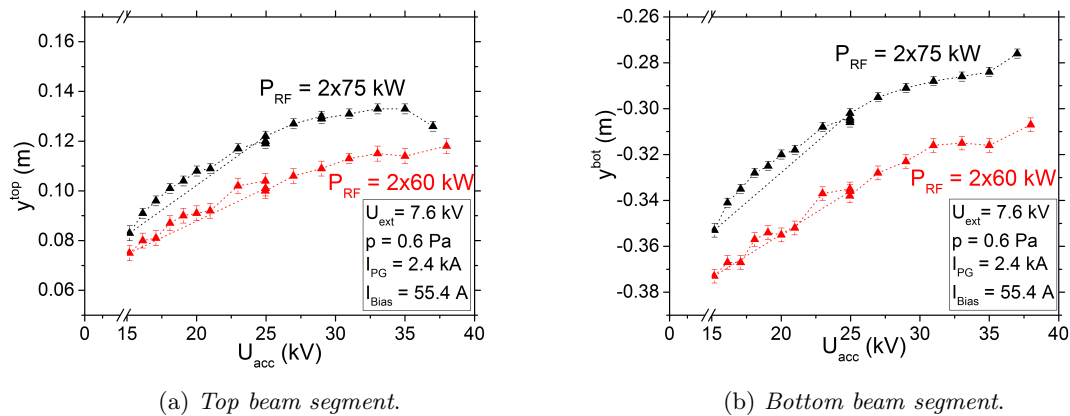

(a) *Top beam segment.*

(b) *Bottom beam segment.*

Figure 4.15: Top (left) and bottom (right) displacement for two different P_{RF} values.

The acceleration voltage affects the velocity of the particles. The effect of the Lorentz

force on the trajectory of a particle is easily explained for one particle: for a negative ion if U_{acc} increases also the velocity increases and the Larmor radius is smaller. It is possible to apply the same finite element analysis used in section 4.1.1 changing the extraction voltage and plotting the final position of the particle after 3.5 m from the grounded grid. In figure 4.16 results with the realistic magnetic field whose trend as a function of the position along the beam line is shown in figure 2.6 and with $U_{\text{ex}} = 7.6$ kV are shown.
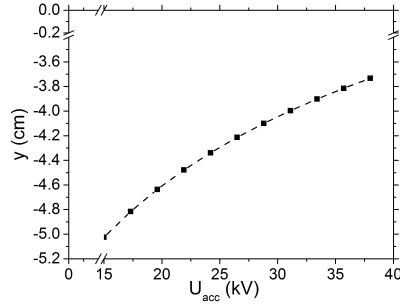
Figure 4.16: Finite element analysis of the final position of a particle that moves in a magnetic field constant in a configuration similar to the ELISE experiment, vector fields oriented such as in figure 4.9

The trend qualitatively matches the experimental results from the calorimeter IR analysis: increasing the acceleration potential the beam segment positions move upwards. Anyway the variation is about 1 cm in the simulation and of about 6 cm in the experimental results. This result supports the hypothesis that the effect of the perveance on the beam segment position is due to phenomena that take place in the source volume.
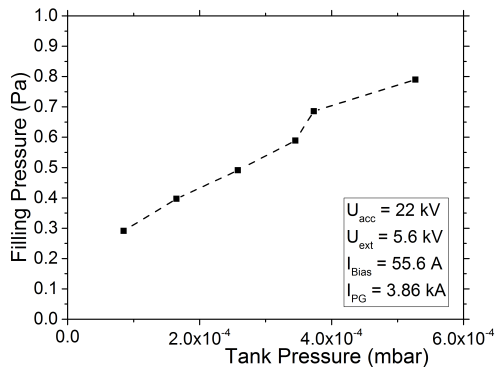
4.3   Pressure scan

Figure 4.17: Linea relationship between the filling pressure and the tank pressure

The space charge compensation reduces the spreading of the beam downstream of the grid system: the higher the pressure the higher the number of positive ions (created due to collisions with the background gas) available for the space charge compensation. As space charge compensation takes place inside the tank downstream of the grid system, the relationship between the fit parameters and the tank pressure gives the influence of tank pressure, via space charge compensation, on beam propagation. However the ITER-relevant parameter is the filling pressure inside the source, so the parameters are studied as a function of that pressure. The pressure in the tank, in which the background gas is present, has a linear trend with respect to the filling pressure: in figure 4.17 the dependence for the pressure scan analysed afterwards is shown.

A decreasing width as a function of pressure is expected and this is confirmed by the experimental results in figure 4.18 both for the two beam segments and for the vertical and horizontal width.
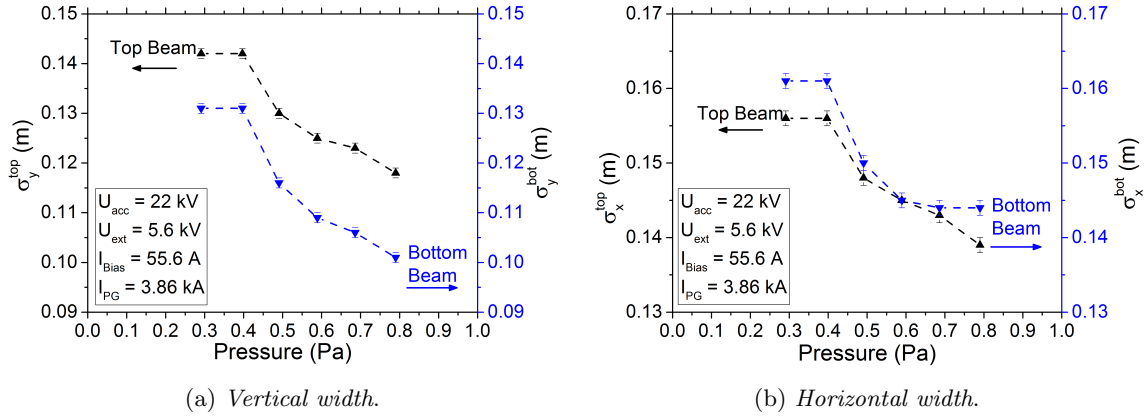
(a) *Vertical width.* (b) *Horizontal width.*

Figure 4.18: Vertical (left) and horizontal (right) width evaluated by the fit.

Figure 4.19 shows the vertical position of the beam segments: a slight movement (about one centimeter) of the beam upwards with increasing the pressure. The ions are neutralised earlier along the beamline if the pressure is higher. This leads to a lower deflection of the beam due to the Lorentz force because, after the neutralisation, neutrals are unaffected by the magnetic field.
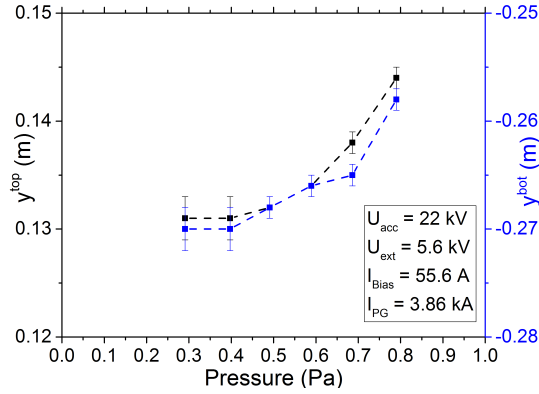

Figure 4.19: Beam segment positions on the calorimeter: in black and blue for the top and bottom beam segment respectively.

4.4 The $E \times B$ drift and the influence of the external magnets

In the following scans the influence of the external magnets on the beam and on the plasma will be analysed. In the plasma region the $E \times B$ varies by changing both the magnetic field, created by the I_{PG} current and by the external magnets, and by changing the electric field due to the voltage associated to the bias current I_{Bias}. On the other hand the beam is influenced by the external magnets and by the I_{PG} current via the Lorentz force and the result is a deflection of the beam. The case of external magnets is even more difficult to analyse. The volume of plasma affected by the $E \times B$ drift is larger the stronger is the magnetic field but the drift velocity is less (see eq.1.24). Downstream of the grid system, due to the change in sign of the filter field at the PG, the strengthening configuration diminish the effect of the Lorentz force on the beam because the magnetic field is weakened by the external magnets. The opposite happens with the weakening configuration: the Lorentz force deflects more the beam because the filter field and the field created by the

external magnets have the same direction. These two effects simultaneously influence the final imprint on the calorimeter and this makes the interpretation of the results particularly challenging.

The effect of the filter field and of the external magnets on the plasma is larger compared to the effect on the beam: the intensity of the field is much higher upstream and within one meter downstream the PG (see fig.2.6 *(b)*) and, in any case, in the plasma volume the B-field is a factor 2 larger. For deuterium, which is heavier than hydrogen, the beam deflection is less pronounced so it is easier to give an interpretation to the results because they are mainly due to what happens in the plasma region. In hydrogen the drifts play an important role upstream and within the grid system as well as on the beam resulting in a more difficult interpretation. The beam width is larger in hydrogen than in deuterium: in deuterium the beam profile on the calorimeter is more defined thus the fit procedure gives more reliable results.

4.5   Bias scan

The bias potential influences the plasma near the PG by varying the electric field. In the figures 4.20 and 4.21 bias scans in relation with three different magnetic configurations are shown: with the permanent magnets weakening or strengthening the filter field due to the I_{PG} current and without external magnets (but with the filtering field due to the I_{PG}). In all cases in the plasma region a $E \times B$ drift (eq.1.24) is present with the E-field created by the bias potential.

In the figures 4.20 and 4.21 the vertical position of the beam segments by changing I_{bias} with external magnets in hydrogen and deuterium respectively is shown. The description results easier in deuterium because the ion is heavier than hydrogen and the beam is less affected by drifts: from figure 4.21 it is visible that for same bias current the imprint on the calorimeter is more on the top for higher magnetic field (the highest point is the one with the strongest magnetic field). This is well visible for the top beam segment but it is not so clear for the beam segment on the bottom: the two segments seem to have different behaviour even if comparable trends for the same magnetic configuration.
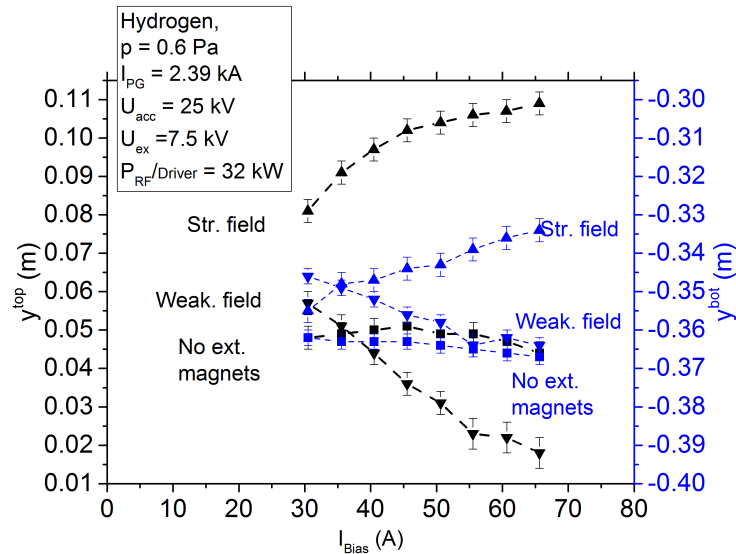

Figure 4.20: Beam position on the calorimeter. Left axis (black points): top segment, right axis (blue points): bottom segment.

Looking at the dependence by changing the bias current (keeping the same magnetic

configuration) the position of the fitted beam segments on the calorimeter moves slightly downwards: this trend is not explained with the $E \times B$ drift because the higher the potential the stronger the drift upwards. It is necessary to note that the variation is slight and it disappears in the case of hydrogen. Anyway the trend may be due to a different ion distribution into the plasma region.
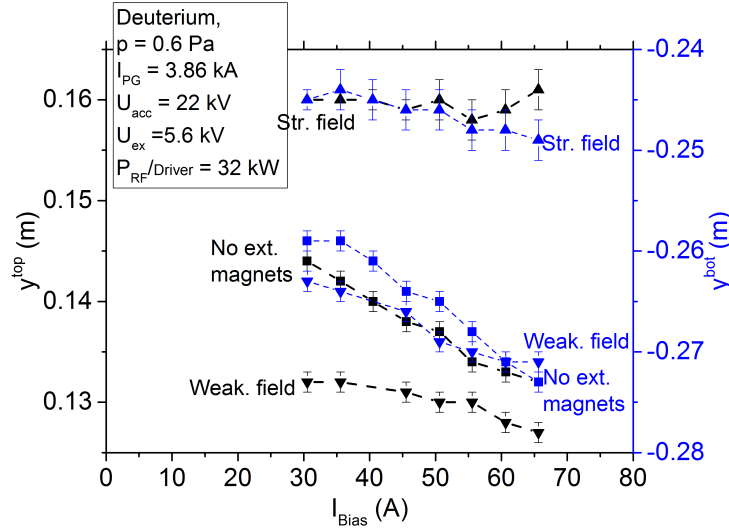

Figure 4.21: Beam position on the calorimeter. Left axis (black points): top segment, right axis (blue points): bottom segment.

In hydrogen the beam is much more affected by drifts that take place inside the extraction and acceleration stage and downstream the grid system. This can be observed by comparing the scales between the plots in figures 4.20 and 4.21: in deuterium for $I_{\text{Bias}} = 65A$ the total variation in position on the calorimeter between the weakening and strengthening configuration is about 4 cm, while in hydrogen at the same bias current the difference amounts to 10 cm. In hydrogen the configuration without external magnetic field has a flat trend, not influenced by the bias electric field while in deuterium it shows a small decrease (less than 1 cm). While the trend is symmetric for top and bottom beam segments (both increase or decrease in the same variation of I_{Bias}) the absolute value of variation is less for the bottom part than for the top.

For what concerns the beam width, in deuterium the ions are heavier and less affected by drifts.

As it is shown in fig.4.23 in deuterium the trends are flat and only a small dependence is present in the case of the strengthening field. The absolute values of σ_x that are about $10 - 14$ cm compared to the distance between two successive beamlet groups (16 cm) show that the fit was able to distinguish the beamlet groups both for the top and for the bottom beam segment. In figure 4.24 the power matrix in case of deuterium for the strengthening configuration is shown: the shape is defined and the beamlet groups are distinguishable.

On the other hand results in hydrogen are shown in figure 4.23: the absolute values of σ_x show the inability for the fit to distinguish the beamlet groups inside the beam segment. The horizontal distance between beamlet groups is 0.16 m while the upper value is $\sigma_x = 24$ cm. In figure 4.24(a)) an example for hydrogen in the strengthening field configuration is shown: the beam is less defined and the beam segments are broader moreover it is not possible to distinguish the beamlet groups.

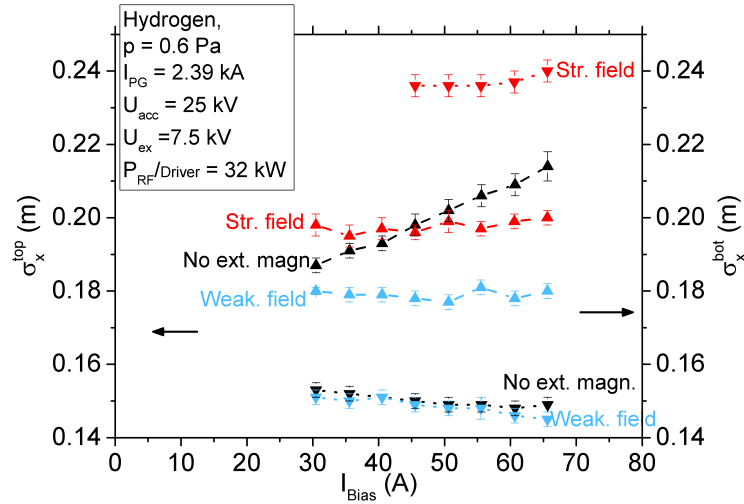From figures 4.22 and 4.23 it is not possible to recognize a clear dependence on the bias current.

Figure 4.22: Beam segment width in horizontal direction, the three configuration are reported in different colours (red for the strengthening field, blue for the weakening one and black for only I_{PG} filtering field), the top beam segment is referred to the left axis while the bottom one to the right axis. For the strengthening configuration the results below $I_{Bias=45A}$ for the bottom segment are not available because the fit does not converge.
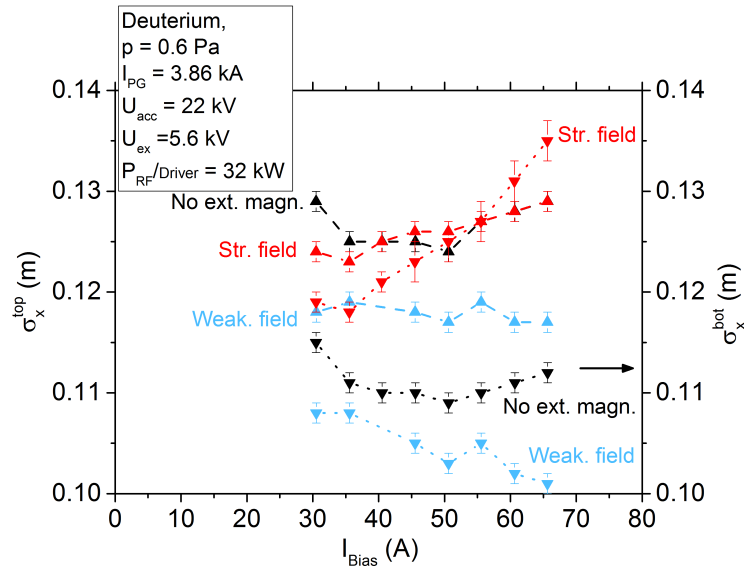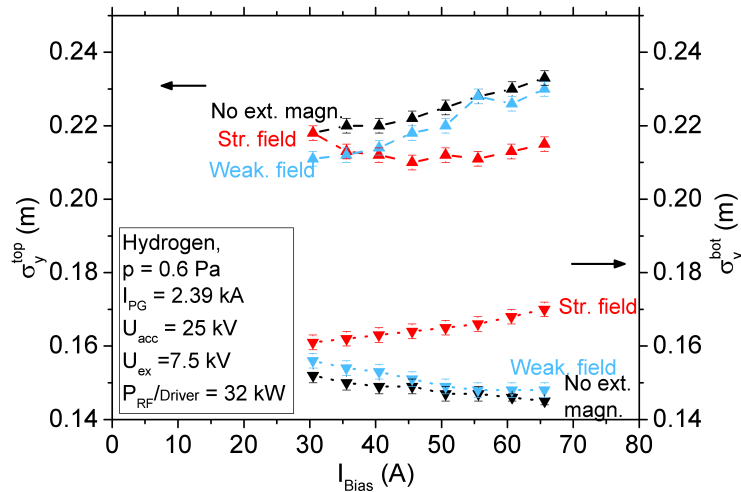

Figure 4.23: Beam segment width in horizontal direction, the three configuration are reported in different colours (red for the strengthening field, blue for the weakening one and black for only I_{PG} filtering field), the top beam segment is referred to the left axis while the bottom one to the right axis.

The comparison between two shots at the same bias current and with the same magnetic configuration is reported in fig.4.24: in hydrogen the beamlet groups merge together and the result is a more spread beam than in deuterium. The final imprint on the calorimeter has a broader shape recognizable by comparing the colour of the blocks located in the edges.

(a) *Hydrogen*
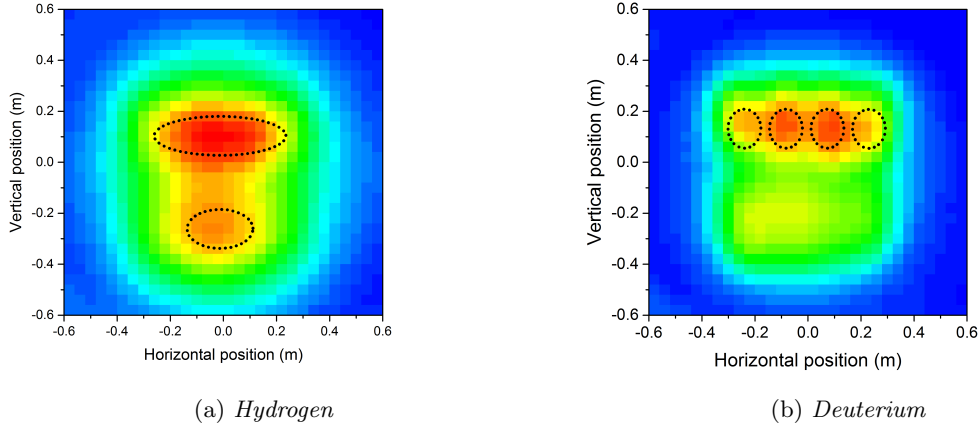
(b) *Deuterium*

Figure 4.24: Shots #13795.01 (left) in Hydrogen and #13316.01 (right) in Deuterium; parameters reported in fig.4.22 and fig.4.23 respectively. In both cases $I_{\text{Bias}} = 65.6$ A with the strengthening field configuration.

Along the vertical direction the two segments are identifiable because σ_y is always lower than half the geometric distance between beamlet groups (39.5 cm along the vertical direction). In deuterium the traces are comparable even if with different trends: the total shift is around 1 - 1.5 cm thus too small to be considered a real dependence. Also in this case it is confirmed that the beam in deuterium has a much more defined profile than in hydrogen: with deuterium the beam has low σ_x and σ_y compared to the cases in hydrogen.

In hydrogen the two beam segments do not show a relation between width and bias current, again the two beam segments react differently: for the weakening configuration and without external magnets the top width increases while the bottom decreases by increasing the bias current; only with the strengthening field the two beam segments seem to react in the same way.

Figure 4.25: Beam segment width in vertical direction, the three configuration are reported in different colours (red for the strengthening field, blue for the weakening one and black for only I_{PG} filtering field), the top segment is referred to the left axis while the bottom one to the right axis.

Due to the beam inhomogeneity between the bottom and top beam segments, the vertical width is different between the two beam segments: in figure 4.25 the absolute value of σ_y is different for the bottom and top beam segment; the value is in any case below the half geometric distance. In deuterium the beam is less affected by inhomogeneities between the beam segments because the width of the two beam segments is comparable in a range of 4 cm.
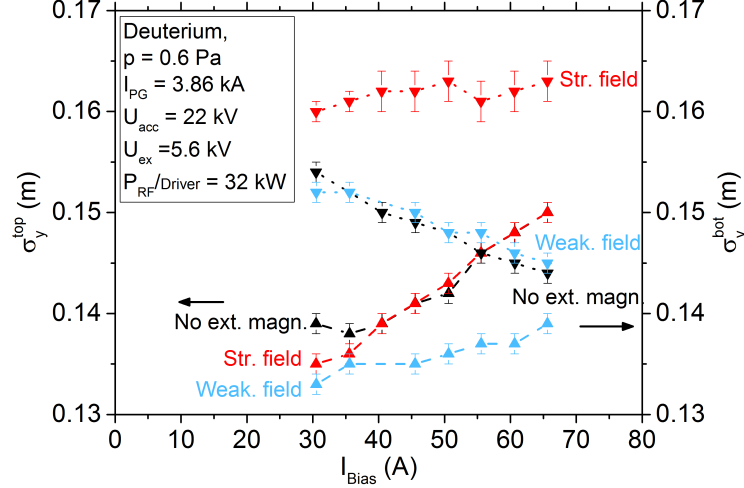

Figure 4.26: Beam segment width in vertical direction, the three configuration are reported in different colours (red for the strengthening field, blue for the weakening one and black for only I_{PG} filtering field), the top segment is referred to the left axis while the bottom one to the right axis.

The variation in σ_y is small compared to the wide range in which the bias current varies and in conclusion it is possible to state that the beam parameters do not exhibit dependences on the bias current.

4.6 I_{PG} scan

In the following scans only the PG current is modified while the bias current is fixed. External magnets in the weakening and strengthening configuration are installed in the plasma volume. The beam segment position from the fit is shown as a function of the I_{PG} current in figure 4.28 for hydrogen and figure 4.27 for deuterium. For deuterium the situation is clearer than in hydrogen and the results are less affected by the drifts: the increase of the I_{PG} current implies an increase of the magnetic field and consequently a decrease of the $E \times B$ drift in the plasma region even if a larger volume of plasma is affected by the drift. Downstream the grid system the beam deflection due to the Lorentz force is diminished or enhanced with strengthening or weakening configuration of the external magnets. It is useful to remember that the adjectives strengthening and weakening are related to the effect on the filter field in the source volume while downstream the PG, where the filter field changes its sign, the effect is the opposite.

The trend, for each configuration, is weak but it is the expected one: for each configuration a beam deflection more downwards is expected by increasing the magnetic field i.e. the I_{PG} current, because the Lorentz force on the beam is stronger.

On the other hand, at least in deuterium in figure 4.27, for the same value of filter field i.e. at same I_{PG} current, the position of the beam segments on the calorimeter in case of

strengthening field is placed more on the top than in the other two magnetic configurations. The same can be said for the configuration without external magnets with respect to the weakening field configuration. This can not be explained with a variation in the source because with the same filter field the $E \times B$ drift with strengthening magnets is less pronounced than without magnets so the position on the calorimeter should be less displaced towards the top for the case of strengthening field than in the case without magnets. On the other hand this can be explained by taking into account the Lorentz force on the beam: the stronger the external field in the source, the weaker the magnetic field and the deflection downstream the GG. With the strengthening field the beam is less deflected towards the bottom of the calorimeter and the beam imprint is placed upper than in the other cases.
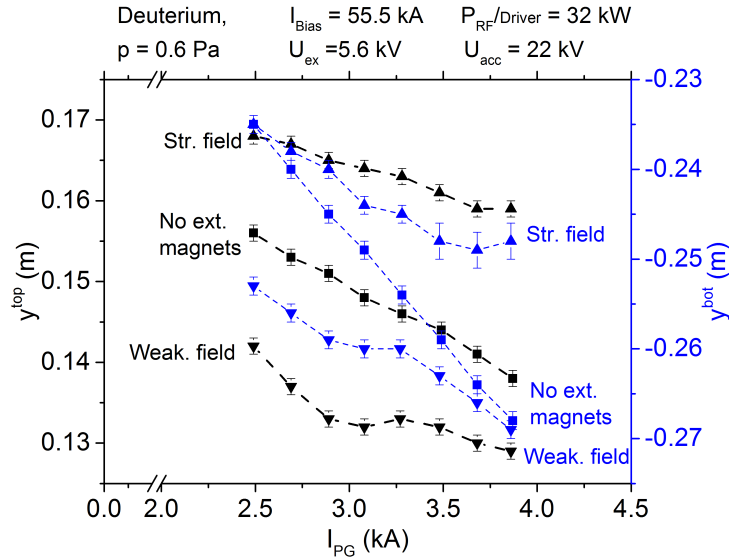
Figure 4.27: Beam segment position on the calorimeter obtained from the fit. In red the strenghtening configuration, in blue the weakening field and in black the case without external magnets. In all the cases the filter field, generated by the I_{PG} current is present.

In hydrogen the drifts play a bigger role than in deuterium and the final imprint on the calorimeter is given by a mixture of plasma drifts, that take place upstream the grid system, and the lorentz force that takes place downstream the grounded grid. Figure 4.28 shows that the range of variation is larger than in deuterium and the trends do not have a clear dependence on the I_{PG} current. The two beam segments react in a different way: without external magnets the top segment center is not affected by the I_{PG} current while the bottom one slightly moves downwards. On the other hand the configurations with the external magnets affect the two segments with the same trend but in opposite directions for the two configurations: the strengthening field causes a beam segment deflection upwards while the weakening field downwards.
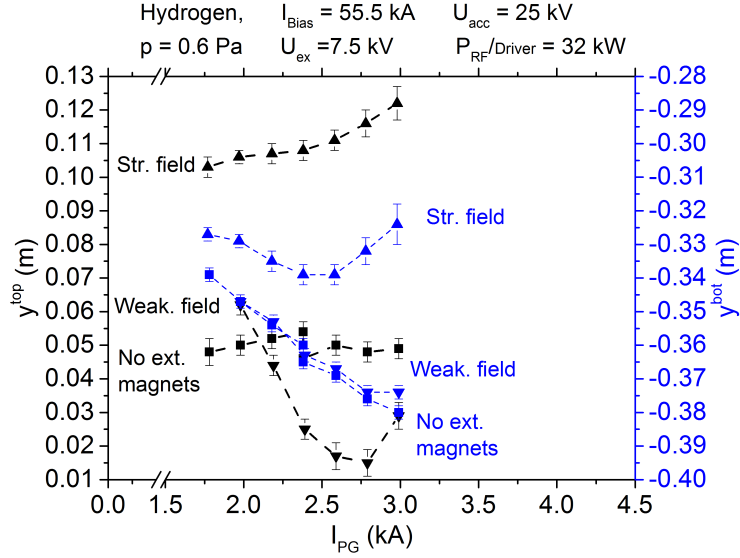
Figure 4.28: Beam segment position on the calorimeter retrieved from the fit. In red the strenghtening configuration, in blue the weakening field and in black the case without external magnets. In all the cases the filter field, generated by the I_{PG} current is present.

Concerning the horizontal width, described by the σ_x parameter, in the case of deuterium shown in figure 4.29 the only configuration that seems to improve the beam optics, i.e. decreasing the width by increasing the I_{PG} current, is the case with the weakening field.
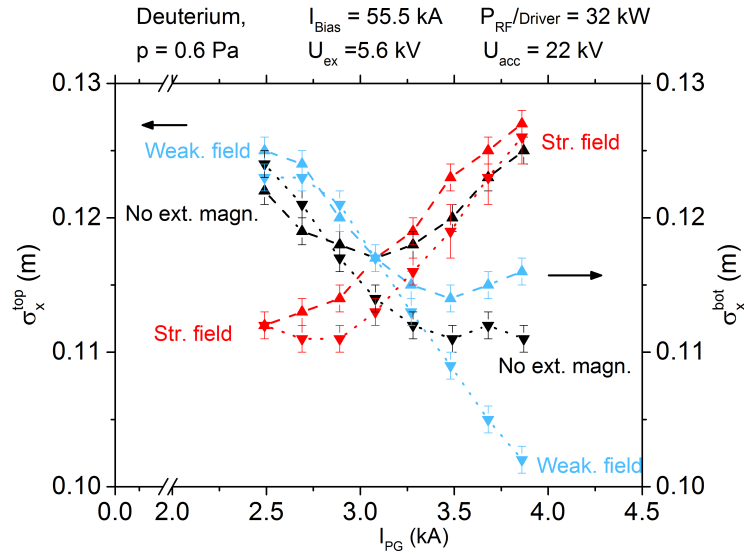
Figure 4.29: Beam segment width in horizontal direction. The three configuration are reported in different colours (red for the strengthening field, blue for the weakening one and black for only I_{PG} filter field), the top segment is referred to the left axis while the bottom one to the right axis.

Anyway, for all the magnetic configurations, the σ_x values vary by about 3 cm in a range of 1.5 kA. The absolute value is between 10 and 13 cm so the fit is capable of distinguishing the beamlet groups inside the beam segment for both the top and bottom segments.

For hydrogen the σ_x upper value is about 26 cm (see figure 4.30): again the fit is not able to distinguish the beamlet groups inside the beam segment. It is difficult to define a trend in

61

hydrogen due to the high uncertainty even if the case in strengthening configuration shows the worst beam optics while the only configuration that decreases, or at least maintains, the width is the weakening configuration. In figures 4.30 and 4.29 the evaluations for hydrogen and deuterium respectively are shown.
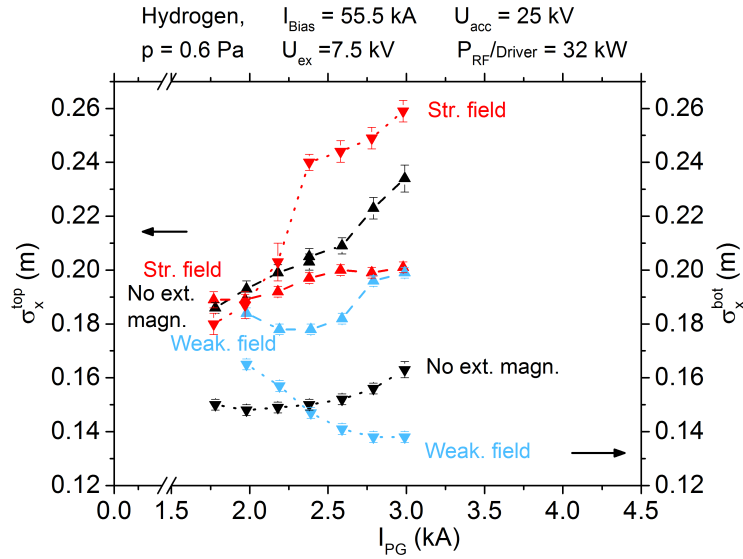

Figure 4.30: Beam segment width in horizontal direction. The three configuration are reported in different colours (red for the strengthening field, blue for the weakening one and black for only I_{PG} filter field), the top segment is referred to the left axis while the bottom one to the right axis.

Along the vertical direction, in deuterium, the σ_y is between 12 cm and 17 cm with an increase in case of strengthening configuration and a decrease in case of weakening configuration.
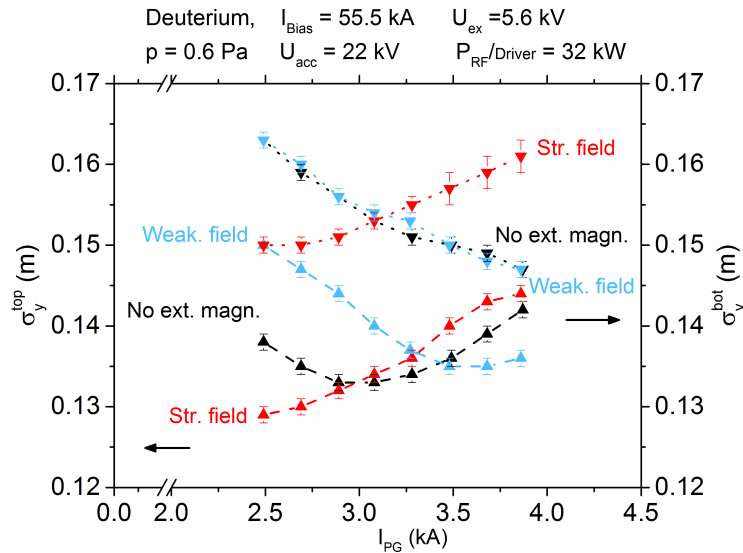

Figure 4.31: Beam segment width in vertical direction. The three configuration are reported in different colours (red for the strengthening field, blue for the weakening one and black for only I_{PG} filter field), the top segment is referred to the left axis while the bottom one to the right axis.

With external magnets the beam segment width varies accordingly for the two beam segments by increasing I_{PG} current. The width of the top beam segment is always larger. The case in which only the filter field is present is particular because the beam segment width does not vary by the same extent by increasing the I_{PG} current. Figure 4.31 shows the σ_y parameter plotted as a function of the I_{PG} value in deuterium. In cases with external magnets the trends are parallel for the beam segments top and bottom but in opposite directions: the beam width increases for the strengthening configuration while it decreases for the weakening one. The case without permanent magnets is different because the two beam segments vary their width in opposite direction by increasing the I_{PG} current.

In hydrogen the two beam segments have different width but the trends are similar: in all cases the width increases or is stable by increasing the I_{PG} current. The only case in which a dependence is clear, in hydrogen, is the bottom segment in the strengthening configuration. In figure 4.32 the vertical width, in terms of σ_y for a I_{PG} scan in hydrogen is shown.
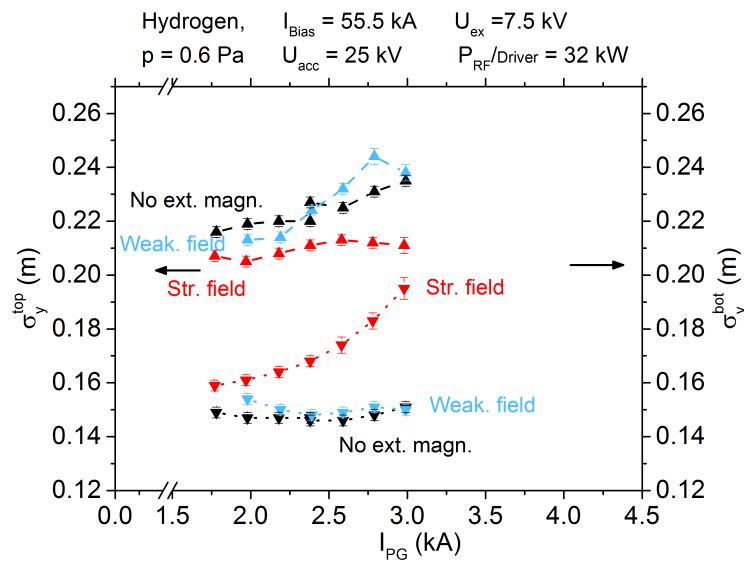

Figure 4.32: Beam segment width in vertical direction. The three configuration are reported in different colours (red for the strengthening field, blue for the weakening one and black for only I_{PG} filter field), the top segment is referred to the left axis while the bottom one to the right axis.

In conclusion the I_{PG} current effect on the beam is weak: the beam deflection is significant i.e. more than $2\,\mathrm{cm}$ only in hydrogen and the direction of the deflection depends on the magnetic configuration in the source. For deuterium this dependence is in agreement with what is expected by changing the magnetic field and consequently the Lorentz force applied to the beam. The optics of the beam, namely the width, seems to show a worse behaviour with the strengthening configuration rather than in the other cases. Anyway the weakening configuration seems to be give the best beam optics even because in almost all cases the absolute value of the width is lower or it decreases more than other configurations.

4.7   Comparison with BES

The analysis of the IR calorimetry can provide information that can be used for cross checking results of other diagnostics e.g. BES. In particular the divergence measured by the BES (see section 2.2.3) is related to the width of the beam measured by the calorimeter.

4.7.1 Beam divergence analysis

While the lines-of-sight of the BES are inclined and they look almost perpendicularly at the beam (see fig.2.9) the measurements of the full width half maximum of the Doppler peak provides an estimate for the beam divergence. In figure 4.33 the comparison between the beam width measured on the calorimeter imprint and the divergence measured by the BES is shown. The vertical and horizontal widths are compared with LOSs that investigate the vertical and horizontal profile respectively. The LOSs chosen for this analysis are #7 that looks at $y = -7.5$ cm for the horizontal profile and the #18 that looks at $x = -8$ cm for the vertical profile (see the coordinate system in figure 2.10).

(a) *Horizontal width vs divergence LOS#7* (b) *Vertical width vs divergence LOS#7*
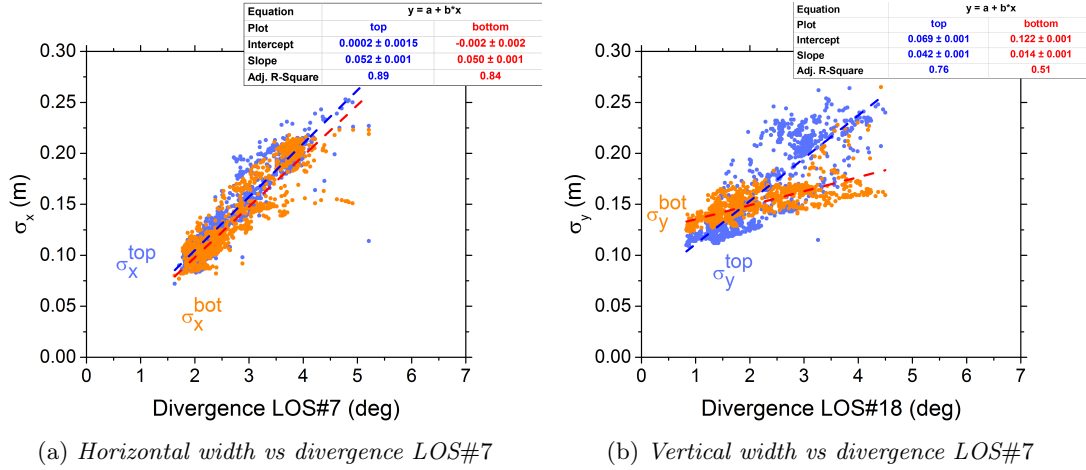
Figure 4.33: Beam segment width compared with the divergence from one line of sight of the BES. In these figures the solid black points are from the top beam segment while the red one are from the bottom beam segment. All these shots are evaluated with the fitting procedure for the beam imprint on the calorimeter. Data from 2015.

For what concerns the horizontal width, namely σ_x, the trends for both top and bottom beam segments show a good agreement with the divergences estimated by the BES. To better visualize this agreement a linear fit is is shown in figure 4.33(a): the two lines have almost the same slope, also the intercepts are close to each other. Figure 4.33(b) shows the vertical width plotted as a function of the divergence. The points show a trend but with a larger dispersion: the R parameter, that indicates the goodness of the fit, is far from the best value i.e. 1 (the range of the R parameter is between 0 and 1). The vertical width for the bottom beam segment has a significantly different trend rather than the top beam segment. A possible explanation for this trend can be a different beam optics due to a less extracted current for the bottom segment.

4.7.2 Broad component

Since the effect of the broad component on the beam profile is weak, in order to prove the presence of the broad component, it is not possible to consider the width provided by the fit but the edges of the calorimeter must be considered instead.

The camera field of view includes parts of the window port so that par can not be included. Thus not all edges of the calorimeter are considered but only a rectangular portion of dimensions 12 blocks × 6 blocks positioned at both edges of the calorimeter (see fig.4.34). The rectangles used are located in the mid left and right edges. The top and bottom edges are not considered since the vertical plasma drift and beam deflection will result in asymmetric beam imprint on the calorimeter. The edges of the calorimeter are supposed to

be reached by parts of the beam with high divergence. The power deposition percentage on the two rectangles can be compared to a simulation of the beam imprint on the calorimeter based on the divergence of the beam determined by BES, taking into account a combination of a narrow and a broad component to define the divergence.
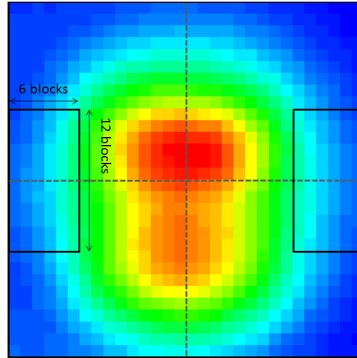

Figure 4.34: In dotted lines the borders of the plates are shown, the value used for the comparison is the percentage of the total power inside deposited inside the solid rectangles

In the simulation formulas all the LOS are taken into account and weighted with the relative power distribution of the two beam segments. The position of the beam segments on the calorimeter is given as an input and corresponds to the value retrieved from the fit, namely y_{top} and y_{bot} [46].

(a) *bias scan.*

(b) I_{PG} *scan.*

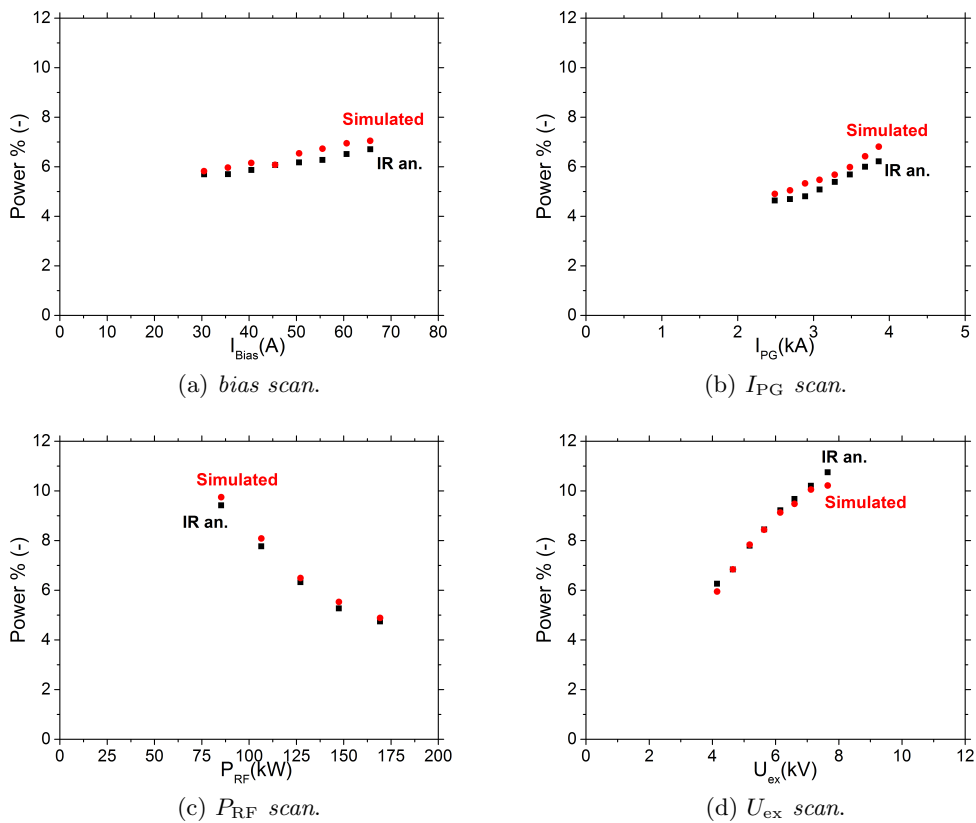(c) P_{RF} *scan.*

(d) U_{ex} *scan.*

Figure 4.35: Broad component, analysis and comparison between the diagnostic calorimeter and BES

From the simulation of the calorimeter imprint the percentage of power deposited on the edges shown in figure 4.34 are calculated. The comparison is shown in figure 4.35 for different scans: in particular for scans in I_{Bias}, I_{PG}, P_{RF} and U_{ex}. The simulation and the results from the IR evaluation are in agreement in trends and in absolute values. The IR calorimetry proves the existence of a broad component that affects the beam divergence.

Chapter 5

Conclusions

5.1   Summary and conclusions

The aim of this thesis was to study the beam at the ELISE experiment via an infra-red analysis of a diagnostic calorimeter placed at 3.5 m from the plasma source.

The beam is composed of beamlets formed by extracting particles from a plasma. This is achieved by means of a set of extraction and acceleration grids. These grids comprise 640 apertures arranged in 8 beamlet groups: the beam is divided in two beam segments (top and bottom) that are formed by 4 beamlet groups each.

The calorimeter surface is segmented in square blocks of dimension 38 mm $\times$ 38 mm separated by a 0.2 mm gap in order to avoid transversal heat diffusion. The blocks are arranged in a 30 $\times$ 30 matrix.

For each beam pulse performed in ELISE a video acquired by an IR camera pointed at the calorimeter is obtained. Due to various phenomena inside the tank it is not possible to measure the calorimeter temperature accurately by the IR analysis during the beam blips: the solution is to define two frames, one before the pulse and one after, and to calculate the temperature increase as a difference between the temperature measurements on the two frames.

The first step of this work is the creation of a BASIC program for the analysis of the calorimeter image. The pixels inside each bock are determined by this program, and by averaging the pixel value, a temperature has been assigned to the block itself. From the averaging process a 30$\times$30 matrix of temperature values is obtained. From the temperature matrix also the power and ion current density profile deposited by the beam are found.

Thermocouples embedded in some blocks on the calorimeter are used to set the correct emissivity in order to calibrate the IR camera for the temperature analysis. One of the results is that, due to a degradation of ε estimation, emissivity periodically needs a recalibration. The causes of this effect in time are not clear up to now. A coverage of the window used for IR calorimetry due to copper sputtering and re-deposition is hypothesized. During a maintenance phase when the source and the extraction system were dismounted the blackening layer that covers the calorimeter surface was re-painted. This re-coating of the calorimeter does not affect the emissivity considerably: the variation before and after the re-coating was less than 0.1. Working on the entire database, the presence of shots during which the IR camera was not focused properly is observed: in order to clarify the effect of the focus on the temperature measurement, a test is performed varying the focus at the same operating parameters for different shot. The conclusion is that the focus adds an uncertainty of about 10% to the measure.

Since the main target was the study of the beam parameters such as beam width, position of the beam on the calorimeters and inhomogeneities between the beam segments, a fit on the 30 $\times$ 30 power matrix is performed: the fit formula consists on 8 bi-dimensional Gaussian

functions, one per beamlet group. The position of the centers for the top and bottom beam segments on the calorimeter is described by y_{top} and y_{bottom} respectively. The vertical and horizontal width is supposed constant for the beamlet groups inside the same beam segment. Finally the database for the IR calorimetry is created for all the videos stored during the past years.

The comparison between the results of the IR analysis and the water calorimetry performed on the calorimeter panels are in good agreement both for the total deposited power and for the distribution of the power on the four plates of the calorimeter. The electrically measured ion current is in agreement with the IR measurements.

In perveance scans the deflection of the beam is highlighted although not yet explained and still under investigation. The width, along the horizontal direction, has a minimum in correspondence to $P/P0 = 0.25 - 0.3$: the observed trend is compatible with the measurements performed by the BES. The vertical width has two different trends for top and bottom beam segments: they seem to obey to different optics.

Acceleration voltage scans show a displacement of the beam upwards by increasing the acceleration voltage for both beam segments: the higher the particle velocity the less the influence of the Lorentz force on the particle the less the beam is deflected downwards. The width, both along the vertical and the horizontal directions, show a minimum in correspondence to the acceleration voltage that optimize the beam optics for the chosen extraction potential: the acceleration stage has an effect on the beam optics comparable, but less significant, to the extraction stage.

The filling pressure inside the source affects linearly the pressure inside the tank, where the space charge compensation on the beam takes place. The higher the pressure the stronger the space charge compensation effect, the less is the beamlet group width: the experimental data support this explanation. For what concerns the beam segment positions on the calorimeter, these move downwards by increasing the filling pressure: the position along the beam line where the neutralisation takes place depends on the background gas density and for higher pressure the beam is neutralized more upstream so it is less affected by the Lorentz force and consequently less displaced downwards.

The magnetic field configuration inside the ELISE source can be modified by equipping it with external permanent magnets. The filter field created by the I_{PG} current is strengthened or weakened by the external magnets depending on how they are installed. Scans in I_{PG} and in bias current were performed with the two different magnetic configurations and without the external magnets. In the source the $E \times B$ drift effect is changed by changing the electric field (driven by the bias current) and the magnetic field by the I_{PG}. The external magnets influence the $E \times B$ drift as well. The same campaign was performed both in hydrogen and in deuterium: the latter heavier isotope forms a beam that is less affected by drifts (e.g. the Lorentz force).

Without external magnets the position of the beam segments on the calorimeter is not influenced by changing the bias current: the trend is so weak that it does not seem to be significant. With external magnets deuterium is hardly affected while in hydrogen the beam seems to move downward with the weakening field and upwards with the strengthening field by increasing the bias current. In hydrogen the beam is more affected by drifts than in deuterium. The width of the beam both in horizontal and vertical direction seems not affected by the bias i.e. the trends are weak. Anyway the situation seems to be worse, i.e. larger beam width, with the strengthening field than in other cases.

The I_{PG} scans analysed with the three magnetic field configurations in deuterium show a displacement of the beam segments towards the bottom of the calorimeter by increasing I_{PG}: the filter field bends the beam due to Lorentz force and the stronger the magnetic field the larger the beam deflection. In hydrogen the trends are not clear due to the drift. The beamlet group width generally increases both in hydrogen and in deuterium for increasing

I_{PG} except for few cases and with some differences between bottom and top beam segments.

The effects of the bias current and of the I_{PG} current involve mainly the source volume by mean of the $E \times B$ drift. Concerning the beam characterisation with the diagnostic calorimeter placed at 3.5 m from the source, the influence of the plasma is visible even if with a small impact.

The lateral portions of the diagnostic calorimeter are analysed in order to investigate the presence of a broad component that affects the beam with a wider width. Several simulations performed taking into account the parameters given from the BES are in agreement with measurements of the percentage of the power deposited on the lateral portions of the calorimeter.

In conclusion the IR thermography provides a robust and reliable analysis on the calorimeter with a sensibility on the beam parameter variation of about 1 cm.

It has a good agreement with other beam diagnostics such as the water calorimetry and the BES. The evaluation of the emissivity is needed in order to properly deduce the temperature. The analysis on the beam imprint confirms the hypotheses for the beam parameter variation by changing the pressure and the acceleration voltage. The beam width as a function of normalized perveance shows a minimum in correspondence to the best perveance value as expected but the beam is deflected downwards in under-perveant conditions without a clear motivation. This phenomenon is still under investigation. Further investigation should be made to confirm the trends in case of external magnets present in the source volume.

5.2   Future improvements and developments

The characterization of the beam can be improved in the experimental data analyses and by means of other experimental campaigns.

The emissivity value can be properly defined for each shot: the value set inside the program can be defined by comparing with the thermocouples before the analysis. This will make the analysis longer but it will make the measurements independent from the ε previously included in the program. In addition, in this work, the emissivity is found by comparing with only 4 thermocouples instead of the 48 actually installed in the calorimeter: in the future the emissivity value can be found using all the available thermocouples.

For what concerns the fit, a first attempt, without changing the fitting formula, can be to enlarge the constraints on the position of the beam segment centers on the calorimeter because the results are clearly cut in correspondence of the lower constraints.

For the shots in which the width is too large compared to the realistic dimensions of the beamlet group, the calorimeter imprint can be fitted with two bell-shaped functions: each describes one of the beam segments.

The analysis of the scans performed in the last years should continue. Some scans were performed with external magnets placed in different positions and with different magnetic configuration inside the source volume and they are not analysed in this work. The calorimeter, placed at 3.5 m can give some hints on the processes inside the plasma volume: the trends that show a dependence of the beam parameters on the plasma parameters should be investigated by performing other scans and studying the reproducibility of the results.

Bibliography

[1]   M. Kikuchi, K. Lackner, and Q. M. Tran, eds. *Fusion Physics*. IAEA International Atomic Energy Agency, 2005.

[2]   G. Miley et al. *Principles of Fusion Energy*. 2000.

[3]   J. D. Lawson. "Some Criteria for a Power Producing Thermonuclear Reactor". In: *Proceedings of the Physical Society. Section B* 70.1 (1957), p. 6. URL: http://stacks.iop.org/0370-1301/70/i=1/a=303.

[4]   J. D. Huba. *NRL: Plasma formulary*. Tech. rep. DTIC Document, 2004.

[5]   R. Pitts, R. Buttery, and S. Pinches. "Fusion: the way ahead". In: *Physics World* 19.3 (2006), p. 20. URL: http://stacks.iop.org/2058-7058/19/i=3/a=35.

[6]   A. R. Choudhuri. *The physics of fluids and plasmas: an introduction for astrophysicists*. Cambridge University Press, 1998.

[7]   URL: http://www.efda.org/jet/.

[8]   2013. URL: https://fusion.gat.com/global/DIII-D.

[9]   URL: http://www.lhd.nifs.ac.jp/en/.

[10] URL: http://www.ipp.mpg.de/ippcms/eng/pr/forschung/w7x/index.html.

[11] D. Wünderlich et al. *IPP activities 2014*. Tech. rep. Max Planck Institüt für Plasmaphysik, 2014.

[12] *Iter, the way to energy*. 2014. URL: http://www.iter.org/.

[13] R. Hemsworth et al. "Status of the ITER heating neutral beam system". In: *Nuclear Fusion* 49.4 (2009), p. 045006.

[14] S. Peruzzo et al. "Thermal analyses for the design of the ITER-NBI arc driven ion source". In: *Fusion Engineering and Design* 82.5–14 (2007). Proceedings of the 24th Symposium on Fusion TechnologySOFT-24, pp. 933 –940. ISSN: 0920-3796. DOI: http://dx.doi.org/10.1016/j.fusengdes.2007.05.071.

[15] R. Hemsworth, A Tanga, and V Antoni. "Status of the ITER neutral beam injection system (invited) a)". In: *Review of Scientific Instruments* 79.2 (2008), p. 02C109.

[16] M. Bacal and M. Wada. "Negative hydrogen ion production mechanisms". In: *Applied physics reviews* 2.2 (2015), p. 021305.

[17] L Schiesko et al. "Magnetic field dependence of the plasma properties in a negative hydrogen ion source for fusion". In: *Plasma Physics and Controlled Fusion* 54.10 (2012), p. 105002. URL: http://stacks.iop.org/0741-3335/54/i=10/a=105002.

[18] E. Speth et al. "Overview of the RF source development programme at IPP Garching". In: *Nuclear Fusion* 46.6 (2006), S220. URL: http://stacks.iop.org/0029-5515/46/i=6/a=S03.

[19] T. Morishita et al. "Mechanism of Negative Ion Production in a Cesium Seeded Ion Source". In: *Japanese Journal of Applied Physics* 40.7R (2001), p. 4709. URL: http://stacks.iop.org/1347-4065/40/i=7R/a=4709.

[20] U. Fantz et al. "Diagnostics of the cesium amount in an RF negative ion source and the correlation with the extracted current density". In: *Fusion Engineering and Design* 74.1–4 (2005). Proceedings of the 23rd Symposium of Fusion TechnologySOFT 23, pp. 299 –303. ISSN: 0920-3796. DOI: `http://dx.doi.org/10.1016/j.fusengdes.2005.06.184`.

[21] G. Boutry and H Dormont. "SOME SURFACE PROPERTIES OF PURE ALKALI METALS". In: *PHILIPS TECH. REV., 30,–8, 9, 10–* (1969), pp. 225–230.

[22] R. G. Wilson. "Electron and Ion Emission from Polycrystalline Surfaces of Nb, Mo, Ta, W, Re, Os, and Ir in Cesium Vapor". In: *Journal of Applied Physics* 37.11 (1966), pp. 4125–4131. DOI: `http://dx.doi.org/10.1063/1.1707987`.

[23] L. W. Swanson and R. W. Strayer. "FieldElectronMicroscopy Studies of Cesium Layers on Various Refractory Metals: Work Function Change". In: *The Journal of Chemical Physics* 48.6 (1968), pp. 2421–2442. DOI: `http://dx.doi.org/10.1063/1.1669464`.

[24] I. Brown. *The physics and technology of ion sources.* 2003.

[25] U. Fantz et al. "Spectroscopy - a powerful diagnostic tool in source development". In: *Nuclear Fusion* 46.6 (2006), S297. URL: `http://stacks.iop.org/0029-5515/46/i=6/a=S10`.

[26] P Agostinetti et al. "Design of a low voltage, high current extraction system for the ITER Ion Source". In: *Negative Ions Beams and Sources, 1st Int. Symposium, AIP CP*. Vol. 1097. 2008, p. 325.

[27] A Krylov and R. Hemsworth. "Gas flow and related beam losses in the ITER neutral beam injector". In: *Fusion engineering and design* 81.19 (2006), pp. 2239–2248.

[28] N Umeda et al. "Long pulse acceleration of MeV class high power density negative H- ion beam for ITER". In: *FOURTH INTERNATIONAL SYMPOSIUM ON NEGATIVE IONS, BEAMS AND SOURCES (NIBS 2014)*. Vol. 1655. 1. AIP Publishing. 2015, p. 050001.

[29] V Toigo et al. "Progress in the realization of the PRIMA neutral beam test facility". In: *Nuclear Fusion* 55.8 (2015), p. 083025.

[30] P. a. Sonato et al. "The ITER full size plasma source device design". In: *Fusion Engineering and Design* 84.2 (2009), pp. 269–274.

[31] B. Heinemann et al. "Design of the half-size ITER neutral beam source for the test facility ELISE". In: *Fusion Engineering and Design* 84.2-6 (2009). Proceeding of the 25th Symposium on Fusion Technology(SOFT-25), pp. 915–922. ISSN: 0920-3796. DOI: `http://dx.doi.org/10.1016/j.fusengdes.2008.11.076`. URL: `http://www.sciencedirect.com/science/article/pii/S0920379608004420`.

[32] B. Heinemann et al. "The negative ion source test facility ELISE". In: *Fusion Engineering and Design* 86.6-8 (2011). Proceedings of the 26th Symposium of Fusion Technology (SOFT-26), pp. 768 –771. ISSN: 0920-3796. DOI: `http://dx.doi.org/10.1016/j.fusengdes.2010.11.031`.

[33] P. Franzen et al. "Progress of the ELISE test facility: results of caesium operation with low RF power". In: *Nuclear Fusion* 55.5 (2015), p. 053005. URL: `http://stacks.iop.org/0029-5515/55/i=5/a=053005`.

[34] P. Franzen et al. "The IPP RF Source: A High Power, Low Pressure Negative Ion Source For The Neutral Beam Injection System Of ITER". In: *AIP Conference Proceedings* 993.1 (2008), pp. 51–54. DOI: `http://dx.doi.org/10.1063/1.2909175`.

[35] P Franzen et al. "On the electron extraction in a large RF-driven negative hydrogen ion source for the ITER NBI system". In: *Plasma Physics and Controlled Fusion* 56.2 (2014), p. 025007. URL: `http://stacks.iop.org/0741-3335/56/i=2/a=025007`.

[36] P. Franzen et al. "Status of the ELISE test facility". In: *AIP Conference Proceedings* 1655.1, 060001 (2015). DOI: http://dx.doi.org/10.1063/1.4916470.

[37] D. Wünderlich et al. "Influence of the magnetic field topology on the performance of the large area negative hydrogen ion source test facility ELISE". In: *submitted to Plasma Physics and Controlled Fusion* (2016).

[38] R. Nocentini et al. "Beam diagnostic tools for the negative hydrogen ion source test facility ELISE". In: *Fusion Engineering and Design* 88.6-8 (2013). Proceedings of the 27th Symposium On Fusion Technology (SOFT-27); Liège, Belgium, September 24-28, 2012, pp. 913–917. ISSN: 0920-3796. DOI: http://dx.doi.org/10.1016/j.fusengdes.2013.01.031.

[39] F. Bonomo et al. "Infra-Red (IR) measurements of the beam calorimeter surface in the ELISE test facility". In: *Report RFX_SPIDER_TN_306* 2008-45-R01.00 (2013). Deliverable T3.3/P1, F4E–RFX–PMS_A–WP–2013.

[40] URL: http://www.flir.com/science/display/?id=46802.

[41] M. Barbisan, U. Fantz, and D. Wünderlich. "Influence of the magnetic filter field topology on the beam divergence at the ELISE test facility". In: *Submitted to 5th International Symposium on Negative Ions, Beams and Sources* (2016).

[42] *ThermoVisionTM SDK*. Version Program version 2.6 SP2. URL: http://www.flir.com/science/display/?id=46802.

[43] D. Wünderlich et al. "Optical emission spectroscopy at the large RF driven negative ion test facility ELISE: Instrumental setup and first results". In: *Review of Scientific Instruments* 84.9, 093102 (2013). DOI: http://dx.doi.org/10.1063/1.4820806.

[44] A. Pimazzoni. "Investigation of ELISE beam properties by means of the diagnostic calorimeter". Università degli studi di Padova, 2014.

[45] P. Veltri et al. "Ion beam transport: modeling and experimental measurements on a large negative ion source in view of the ITER heating neutral beam". In: *Nuclear Fusion under revision* ().

[46] M. Barbisan. June 17, 2016.

Acknowledgements

Ringraziamenti